Check for updates

# Revisiting anodic alumina templates: from fabrication to applications

Alejandra Ruiz-Clavijo, [ID] Olga Caballero-Calero [ID] * and
Marisol Martín-González [ID]

Anodic porous alumina, −AAO− (also known as nanoporous alumina, nanohole alumina arrays, −NAA− or nanoporous anodized alumina platforms, −NAAP−) has opened new opportunities in a wide range of fields, and is used as an advanced photonic structure for applications in structural coloration and advanced optical biosensing based on the ordered nanoporous structure obtained and as a template to grow nanowires or nanotubes of different materials giving rise to metamaterials with tailored properties. Therefore, understanding the structure of nanoporous anodic alumina templates and knowing how they are fabricated provide a tool for the further design of structures based on them, such as 3D nanoporous structures developed recently. In this work, we review the latest developments related to nanoporous alumina, which is currently a very active field, to provide a solid and thorough reference for all interested experts, both in academia and industry, on these nanostructured and highly useful structures. We present an overview of theories on the formation of pores and self-ordering in alumina, paying special attention to those presented in recent years, and different nanostructures that have been developed recently. Therefore, a wide variety of architectures, ranging from ordered nanoporous structures to diameter changing pores, branched pores, and 3D nanostructures will be discussed. Next, some of the most relevant results using different nanostructured morphologies as templates for the growth of different materials with novel properties and reduced dimensionality in magnetism, thermoelectricity, *etc.* will be summarised, showing how these structures have influenced the state of the art in a wide variety of fields. Finally, a review on how these anodic aluminium membranes are used as platforms for different applications combined with optical techniques, together with principles behind these applications will be presented, in addition to a hint on the future applications of these versatile nanomaterials. In summary, this review is focused on the most recent developments, without neglecting the basis and older studies that have led the way to these findings. Thus, it gives an updated state-of-the-art review that should be useful not only for experts in the field, but also for non-specialists, helping them to gain a broad understanding of the importance of anodic porous alumina, and most probably, endow them with new ideas for its use in fields of interest or even developing the anodization technique.

## 1 Introduction

Porous anodic aluminium oxide (AAO) membranes are a hot research topic due to their great versatility with applications in a wide range of scientific fields. AAO membranes provide a cost-effective platform to obtain structures with a high density of ordered pores with diameters in the order of nanometers and with lengths that can reach the micrometer range. Since the published work by Masuda *et al.* in 1990,[1] where the fabrication process of highly ordered porous structured alumina membranes in oxalic acid was first reported, research has

come a long way. New conditions under different anodization regimens have been discovered in many different types of acidic electrolytes and experimental conditions (temperature, applied anodization potential, *etc.*),[2–13] which allow alumina membranes with pre-designed porous structures (pore diameter, inter-pore distance, porosity, length, *etc.*) to be obtained for certain applications. This high degree of tunability of the porous structure at the nanoscale level allows a fine control of the optical properties displayed by alumina films, which can be exploited for sensing applications.[14–20] Furthermore, their high surface to volume ratio (associated with their pore density) makes them appropriate vehicles for drug delivery applications.[21–25] These membranes can be further used as templates for micro- and nano-structuration of different materials, which is highly demanded in the nanotechnology

*Instituto de Micro y Nanotecnología, IMN-CNM, CSIC (CEI UAM+CSIC) Isaac Newton, 8, E-28760, Tres Cantos Madrid, Spain. E-mail: olga.caballero@csic.es*

field. Several distinct morphologies ranging from solid nanowires,[26–35] segmented nanowires of varying compositions[36–38] or diameters,[37,39] hollow tubular wires, also referred to as nanotubes,[40–48] nanocones,[49] and Y-branched wires[50–56] to 3D networks of interconnected nanowires[26,57–62] can be obtained by filling the previously generated porous structure. This can be achieved through different growth techniques such as electrochemical deposition (ED), Chemical Vapour Deposition (CVD), Atomic Layer Deposition (ALD), and sputtering, among others. Holey films,[63–68] also known as antidot arrays, can be fabricated if the deposition of a certain material takes place only over the surface of a hollowed membrane, replicating this structure. Depending on the chosen material, different phenomena and interesting optical, electric, and magnetic properties have been observed in the above mentioned shapes. Hence, alumina membranes provide powerful platforms for studying the property changes occurring at the nanoscale.

Nowadays, there is a wide variety of materials and fabrication techniques that can produce nanostructures or highly nanoporous media for their use in different applications. For instance, for the fabrication of hard templates with features at the nanoscale, there are several possibilities.[69,70] One type of widely used nanostructured 3D templates is opals or inverse opals, where the final structure depends on the dimensions of the starting spheres (ranging from 140 to 350 nm, approx.) and their nature (polystyrene, silica, etc.). Also, one can consider lithography-based techniques, such as two-photon lithography, which can produce 3D templates. In this case, very exotic structures can be designed, but this is a costly and time-consuming technique, and the typical dimensions of the obtained features are hundreds of nanometers in diameter.[71] Another way to obtain nanopore templates is the fabrication of ion-track-etched polymeric membranes, where a high density of parallel pores with diameters in the range of tens to hundreds of nanometers and microns in length can be obtained. Even 3D structures based on irradiating polymeric membranes with different incident angles to their surface can be achieved. Nevertheless, in this case, the drawbacks are that there is no ordering of the nanopores or control over their actual position, and an ion accelerator is needed to produce the tracks.[72] Other types of widely used nanoporous structures in current research, besides AAOs, are porous polymers, such as block copolymers[73] and metal-organic frameworks (MOFs),[74] which provide a high surface to volume ratio, but they also have limited thermal stability, where none of them able to function over 600 °C,[75] and limited thickness of the achieved nanostructures. Also, the research on mesoporous silica[76] is relevant, but in this case, mostly silica nanoparticles (100 to 500 nm in diameter) with a porous surface (ranging from 2 to 50 nm in diameter) are employed, which give rise to different architectures than that obtained with AAOs. Then, as we will see through this review, AAOs appear as the most suitable platforms for a great number of applications, either as porous materials themselves or templates for the fabrication of a variety of nanostructured architectures. They provide thermal stability to the structures, even over 1000 °C,[77] large areas of high density pores, good control over the pore diameter (which can range from tens to hundreds of nm), great control over the structural parameters of 3D structures, and a large aspect ratio with a cost-effective, easily scalable method, and therefore, are widely used and provide an active field of research.

In this work, an updated review of the state of the art of this rapidly evolving field is presented, starting with a description of the AAO porous structure and the most used parameters for its fabrication (section 2). Then, the different theories for the mechanisms of pore formation are discussed (section 3), followed by an insight into the two most used anodization regimes, namely mild and hard anodization (section 4). Once the theory and most used regimes are introduced, the influence of the anodization conditions to obtain different morphologies of porous structures, such as branched structures, pores with modulated diameters, and even 3D porous structures, is reviewed (section 5). The last part of this manuscript is devoted to a review of the latest publications on the applications of the different AAO porous structures, both as templates to grow replicas of their nanoporous structures in different materials (section 6) and due to their nanoporous structure themselves (section 7), which make them ideal candidates for applications such as structural coloration, photonic structures, and sensors. Accordingly, this work aims to provide a deep understanding of AAO nanoporous structures, from their formation mechanisms to their technological applications.

## 2 AAO porous structure

The electrochemical oxidation of a metal, also known as anodization, is a simple and low-cost electrochemical process that produces an oxide layer on the target metallic surface over large areas. This process has been used to obtain nanoporous, nanotubular, and other types of nanostructured functional oxide layers on a wide variety of metals and semimetals, such as gold,[78] cobalt,[79] copper,[80] gallium,[81] hafnium,[82] iron,[83] molybdenum,[84] niobium,[85] tin,[86] titanium,[87,88] tungsten,[89] vanadium,[90] zinc,[91] and zirconia.[92] These oxide films have many applications in catalysis,[78,79,84] photocatalysis,[83,87,89,91] supercapacitors,[90] photoelectrodes,[88] thermal protection,[92] etc. In most cases, the applications take advantage of the large surface to volume ratio of the formed structures. In the case of aluminium anodization, it was intensively studied firstly for the protection of surfaces, and recently, most of the research has been devoted to the fabrication of nano-devices and ordered tunable nanostructures. Anodic aluminium oxide (AAO) is also produced via the electrochemical oxidation of an aluminium substrate, which is usually performed in a two-electrode electrochemical cell, where the working electrode is aluminium. Depending on the electrolyte composition, two different types of anodic oxides can be grown, compact nonporous anodic aluminium oxide and porous alumina films.

To better understand the formation process of this nanoporous structure, one first has to understand how a simpler structure, namely non-porous anodic aluminium oxide films, is produced. In this case, solutions with pH 5–7, in which the anodic aluminium oxide is insoluble, are used. Then, under a certain applied voltage, an insulator oxide barrier layer is formed. In brief, the process involves the migration of oxygen-containing ions ($O^{2-}$ and $OH^{-}$) into the metal from the metal-oxide interface, while the metal ions can either form an oxide layer or be released to the electrolyte. The current density flowing through this barrier layer eventually decays due to its insulating behavior, limiting the maximum thickness of the resulting barrier oxide layer. Therefore, the final thickness of this non-porous alumina is proportional to the anodization potential ($U$). These films are usually used for corrosion protection.

Nanoporous AAO membranes are obtained in a more acidic medium to slightly increase the solubility of the anodic oxide barrier layer. In this case, the abovementioned nonporous barrier layer is also formed when a certain potential is applied, but then, due to the increased solubility of this layer in an acidic environment, a porous anodic oxide layer starts to grow. In this system, the thickness of the barrier layer remains constant throughout the process due to the balanced competition between the new anodic oxide formed and the oxide dissolution at the oxide/electrolyte interface.[93] This process will be described in detail in section 3, where the formation and growth mechanisms will be discussed. Here, simply, the final thickness of the porous AAO membrane is directly proportional to the anodization time.

Then, by controlling the anodization conditions (temperature, anodization voltage, anodization time, electrolyte composition, *etc.*), self-ordering of the vertical pores in a closed-packed hexagonal pattern can be achieved (Fig. 1). Under the conditions that give rise to self-ordering of the pores, each pore forms a hexagonal unit cell. The most characteristic parameters of the porous structure are the pore diameter ($D_p$), interpore distance, ($D_{int}$), which also refers to the cell size, and barrier layer thickness ($t_b$).

Depending on the temperature, electrolyte composition, and applied potential, the structural parameters of the porous structure of alumina membranes can be varied, mainly the pore diameter, interpore distance, and barrier layer thickness. Similar to non-porous anodic oxide films, the thickness of the barrier layer is proportional to the anodization potential ($U$). S. Z. Chu *et al.* studied the linear relationship between $U$ and $t_b$ in different acidic media,[94] (see Fig. 2). However, there is no unified explanation for how each of the abovementioned electrochemical factors influences the diameter pore and interpore distance. In general, it is accepted that the anodizing potential (or current density) increases the pore diameter[95] and interpore distance[95–97] according to the following expressions under mild anodization conditions (see section 4.1).

$$D_p = \xi_p \times U = 1.29 \times U \tag{1}$$

$$D_{int} = \xi_{MA} \times U = 2.5 \times U \tag{2}$$

where $D_p$ and $D_{int}$ are the pore diameter and interpore distance, and $\xi_p$ and $\xi_{MA}$ are proportionality constants of the pore diameter and cell size under mild anodization conditions, respectively, with the applied potential ($U$). The linear correlation of the cell size (or interpore distance, $D_{int}$) and the anodizing potential is shown in Fig. 2b and c in various electrolytes. Nevertheless, there is a discrepancy in the effects that temperature[95,98–100] and electrolyte pH[95,97,101–103] (electrolyte concentration) have on both structural parameters. The major differences arise from comparing different electrolytic solutions. A more detailed explanation between the experimental conditions and the structural parameters from all the data that can be found in the literature is already discussed in several books[104,105] and reviews.[106]

The three most used acidic electrolytes are sulfuric, oxalic, and phosphoric acid. Studies of these three electrolytes have allowed ordered porous systems to be obtained in a wide range of conditions (temperature, concentration, and mixture of chemical species) and under two different potentiostatic (or galvanostatic) regimens, ranging from mild anodization (MA, low-field anodization regimen) to hard anodization (HA, high-field anodization regimen), and more details can be found in section 4. Besides these three acids, other acids have been used, such as selenic ($H_2SeO_4$),[107–109] arsenic ($H_3AsO_4$),[11] phosphonic ($H_3PO_3$),[7] phosphonoacetic,[8] chromic ($H_2CrO_4$),[110] sulfamic ($NH_2SO_3H$),[111] pyrophosphoric ($H_4P_2O_7$),[112] malonic,[113] tartaric,[9] citric[96,114] and etidronic[10] acids. Under these less known electrolytic solutions, self-ordering of the pores can also be achieved, but only under specific anodization conditions. These acidic systems do not show the same capability as the conventionally used acids, or they have not been thoroughly studied to date, and thus, the anodization con-
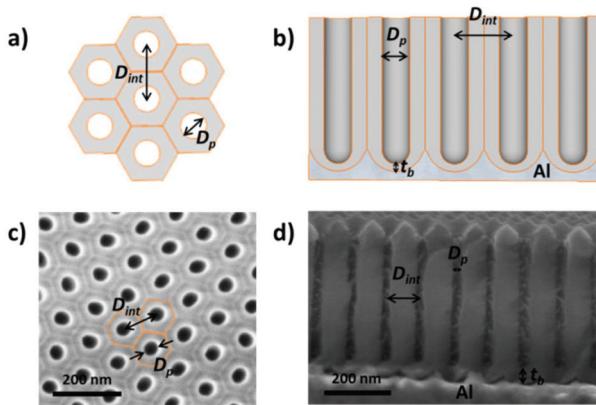


**Fig. 1** (a) Schematic top view of the arrangement of 6 hexagonal pore unit cells. (b) Lateral sketch view of an anodic oxide aluminium porous membrane. (c) Top and (d) cross-sectional view SEM images of a lab-made alumina membrane (0.3 M oxalic acid). Structural parameters of the alumina porous structure including pore diameter ($D_p$), interpore distance, ($D_{int}$), and barrier layer thickness ($t_b$) are identified in all the images.
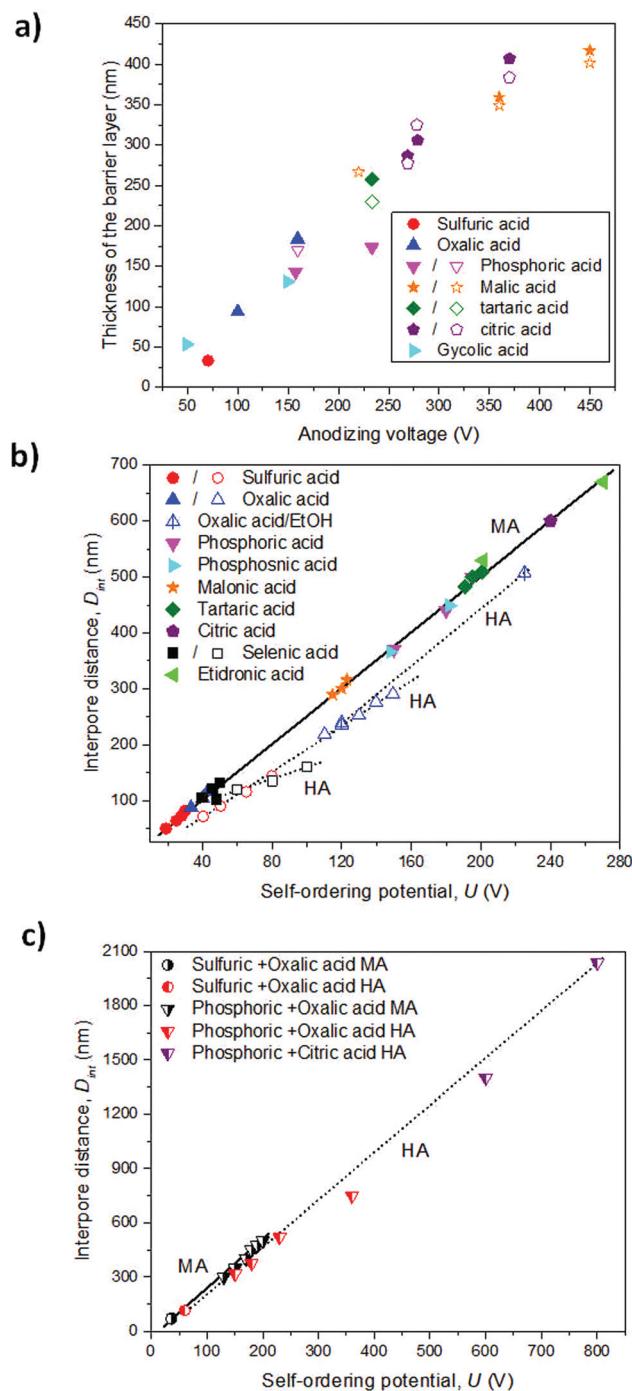
**Fig. 2** (a) Evolution of the thickness of the barrier layer as a function of the anodizing potential in different acidic electrolytes.[94] Solid symbols represent the measured values. Open symbols, calculated values from the half-thickness of the pore wall. (b) Self-ordering regimes under MA (solid symbols) and HA (open symbols) in different electrolytes. (c) Self-ordering conditions of mixed electrolytes, under MA (black symbols) and HA (red and purple symbols) regimes. The black solid line and black dotted lines were added to guide the eye, showing the linear correlation of the cell size (or interpore distance, $D_{int}$) and the anodizing potential ($U$) under MA and HA conditions, respectively. Data was taken from Table 1.

ditions to obtain nanoporous ordered structures are limited considering that for each used acid, there is only a certain range of applied voltages at which ordered pore structures can be formed. Usually, two-step anodization under MA conditions is used to obtain highly ordered nanoporous structures,[1,115] even though this type of order can also be achieved under certain conditions in HA, as it will be demonstrated later.[4] However, the resulting alumina membranes display new cell parameters in terms of pore diameter and inter-pore distance that were not covered by the more traditional acids, as presented in Table 1. Synthesized alumina membranes have been reported with pores as small as 8–10 nm in diameter[107] to several hundred nanometers.[10,116] The interpore distance between neighboring pores ranges from 63–65 nm (smallest interpore distance obtained to date in sulfuric acid[117]) to around 1.4–2.0 μm (in a citric acid/ethylene glycol/phosphoric acid mixture solution[118]). Thus, the features of the porous structure of alumina membranes can be selected to fulfill the requirements of many different applications.

## 3 Pore formation and pore growth mechanism

During anodization, the formation process of the porous structure of alumina can be divided into four stages. Each stage is associated with a particular step in the growth process of the membranes. Fig. 3 shows a typical current density-time curve recorded during potentiostatic anodization conditions. The different stages are delimited by the changes in the current density. The illustrations above portray the evolution of the growing porous oxide film in each stage. Under galvanostatic conditions, in the profile of the recorded potential-time transient curve (not shown here), these same stages can be identified.[127]

The chemical reactions involved in all the different stages of the anodization process in acidic media between the metal/oxide interface and oxide/electrolyte interface are as follows:

$$2Al^{3+}_{(ox)} + 3O^{2-}_{(ox)} \rightarrow Al_2O_3 \tag{3}$$

$$Al_2O_3 + 6H^{+}_{(aq)} \rightarrow 2Al^{3+}_{(aq)} + 3H_2O_{(l)} \tag{4}$$

$$Al^{3+}_{(ox)} \rightarrow Al^{3+}_{(aq)} \tag{5}$$

$$2O^{2-}_{(ox)} \rightarrow O_{2(g)} + 4e^{-} \tag{6}$$

$$2H_2O_{(l)} \rightarrow O^{2-}_{(ox)} + OH^{-}_{(ox)} + 3H^{+}_{(aq)} \tag{7}$$
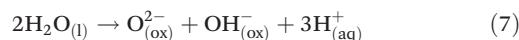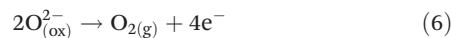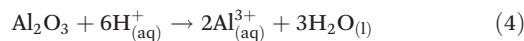
The formation of anodic oxide occurs at the metal/oxide interface, as described by reaction (3), while the dissolution of anodic alumina occurs at the oxide/electrolyte interface, as shown by reaction (4). Reaction (5) corresponds to the direct ejection of $Al^{3+}$ ions from the metal surface towards the electrolyte, due to an applied electrical field. Reactions (5) and (6) reduce the efficiency of the anodization process, while reaction (7) is the dissociation of water molecules occurring at the

**Table 1** Structural parameters of ordered anodic oxide membranes obtained using different electrolytic solutions (single acids and mixed acidic solutions) and varying anodizing conditions (temperature and applied potential)

**Single acids**

| Acid | Electrol. concentration | An. Reg. | Voltage/current density | $T$ (°C) | $D_p$ (nm) | $D_{int}$ (nm) | Ref. |
|---|---|---|---|---|---|---|---|
| Sulfuric | 0.05–0.2 M | MA | 30–28 V | 0 | 21–22 | 82–73 | 102 |
| | 0.3 M | MA | 25 V | 0 | 20–25 | 63–65 | 117 |
| | 0.3 M | MA HA | 25 V (0.3 M, 10 min) 40–80 V | −1.5 to 1 | 15–30 | 78–114 | 2 |
| | 10% V/V | HA | 40–70 V/160–200 mA cm$^{-2}$ | 0 | 30–50 | 90–130 | 119 |
| | 15 wt% H$_2$SO$_4$/50 wt% eth. glycol | MA | 19 V | −15 | 12–15 | 50 | 3 |
| Oxalic | 0.3 M | MA | 40 V | 1 | 30 | 100 | 120 |
| | 0.3 M | MA HA | 40 V 110–150 V | 1–2 | 49–59 | 220–300 | 4 |
| | 0.3–0.75 M (5–10% ethanol) | HA | 120–225 V | −1 to 0 | 50–60 | 240–507 | 5 |
| Phosphoric | 0.1–0.3 M | MA | 195 V | 0 | 150–200 | 500 | 116–97 |
| | 0.25–0.5 M/H$_2$O/EtOH | HA | 195 V, 150–400 mA cm$^{-2}$ | −10 to −5 | 140–80 | 380–320 | 6 |
| Phos-phonic | 0.5 M | MA | 150–180 V | 0–10 | 140 | 370–440 | 7 |
| Phos-phono-acetic | 0.9 M | MA | 205–210 V | 10–15 | | 500–550 | 8 |
| | 0.3 M | | 225 V | 10 | | | |
| Selenic | 0.3 M | MA | 46–48 V | 0 | 10 | 102 | 107–109 |
| | 0.3 M | HA | 60–100 V | 0 | | 120–160 | 121 |
| Malonic | 4 M | MA | 120 V | 5 | | 300 | 9 |
| | 0.3 M oxalic | HA | 110–140 V | 5 | | | 113 |
| | 1.67 M malonic | MA | 125–140 V | 0 | | | |
| Citric | 2 M | MA | 240 V | 20 | | 600 | 96 |
| Tartaric | 3 M | MA | 195 V | 5 | | 500 | 9 |
| Etidronic | 0.3 M | MA | 210–270 V | 20 | 250 | 530–670 | 10 |
| Arsenic | 0.3 M | MA | 320 V | 0 | 220 | 920 | 11 |
| **Mixture of acids** | | | | | | | |
| Sulfuric + oxalic acid | 0.3 M + 0.3 M | MA | 36 V | 3 | | 73 | 122 |
| | 0.07–0.2 M sulfuric + 0.4 M oxalic | MA/ HA | 36–60 V | 0 | | 69–115 | 123 |
| Phosphoric + oxalic acid | 1 wt% phosphoric + 0.03–0.3 M Oxalic | MA | 200–130 V | 1 | 130–53 | 500–300 | 124 |
| | 0.05–0.3 M phosphoric + 0.3–0.4 M Oxalic | MA HA | 35 V 150–180 V | 0 | | 317–375 | 125 |
| | 0.3 M phosphoric + 0.1–0.3 M Oxalic | MA HA | 70 V 230 (0.1 M Ox.)–360 V (0.3 M Ox.) | <5 | 110–119 | 520–700 | 126 |
| Phosphoric + citric acid | Citric acid/ethylene glycol/Phosp. acid with different concentrations | HA | 600–800 V | −2 | | 1400–2036 | 118 |

oxide/electrolyte interface. O$^{2-}$/OH$^-$ ions migrate towards the metal/oxide interface under an electric field, providing new ions to form the anodic oxide.

### 3.1 Stage I

The exponential decay of the current density in this stage is associated with the fast formation process of the oxide barrier layer, since the electrical resistance increases due to the insulator nature of the forming compact oxide layer, which gets thicker with time. Several models describe this ionic migration through the oxide layer, describing the observed current under potentiostatic conditions, and setting different effects that determine the final rate obtained, including the classic models of Verwey, where the transport of ions within the oxide film is considered determinant,[128] Cabrera and Mott, where the rate is determined by the transport across the metal-oxide interface,[129] and Dewald, where the transport of ions across the oxide-electrolyte interface is also accounted for.[130] In the 90s, novel approaches such as the point defect model, includ-

ing the dissolution of the oxide film and the presence of point defects in it,[131] and the Lohrengel model, where a hopping mechanism of the ions is considered,[132] were developed. The most recent studies on the conduction through thick porous oxide films consider not only the diffusion and migration of the ions, but also stress-induced material flow and other contributions to the mass transport,[133] which have shown importance in the process at this stage.

### 3.2 Stage II and III

The increase in the current density at this stage corresponds to initial pore nucleation, which continues until a local maximum is reached. This maximum is associated with the breakdown of the oxide barrier layer and the actual development of an incipient disordered porous structure. Different theories have been proposed to shed some light on the question: what is it that sets into motion pore nucleation after the fast formation of the oxide barrier layer? Two main theories try to explain the pore nucleation mechanism occurring at this
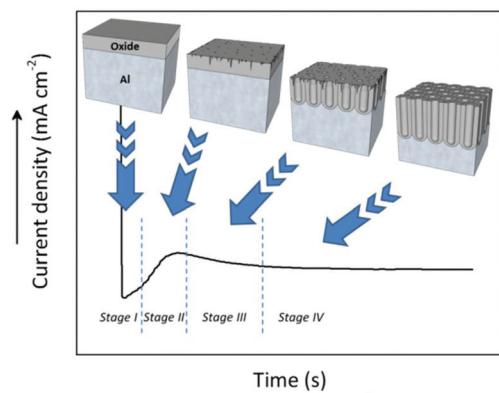
**Fig. 3** Profile of the current density-time curve recorded during potentiostatic anodization of a lab-made AAO alumina membrane prepared in 0.3 M $H_2SO_4$ at 25 V. The above-inserted illustrations show the changes occurring at the different stages, from the formation of the non-porous oxide barrier layer (stage I) to the development of pores in an ordered hexagonal arrangement (stage IV). Going through several intermediate states, the generation of defects and cracks in the surface of the oxide barrier layer (stage II) where the current will accumulate creates space for the nucleation pore sites, acting as precursors for the initiation growth of bigger pores (stage III).

stage, namely the field-assisted model and the stress-driven mechanism. The *field-assisted* model, which was developed by O'Sullivan and Wood,[95] suggests field-assisted pore formation. The current concentration of local imperfections on the initial barrier layer will lead to the non-homogenous growth of this layer. Pore nucleation points emerge at the thinner regions of the oxide layer. The s*tress-driven mechanism* was developed by Shimizu and Thompson.[134] They proposed a model where the stress is the key factor for the evolution of pores. Stress originates at the metal/oxide interface as a result of volume expansion at this interface as the metal substrate is being oxidized. This tensile stress contributes to local cracking of the anodic oxide film (over protuberances or ridges found in the metal surface due to imperfections or impurities). A high local current density occurs at the cracked sites and ions are consumed from the aluminium base to heal these regions, resulting in non-uniform film growth.

Between these two theories, *i.e.*, the field-assisted model and the stress-driven mechanism, the former is the most accepted and cited to explain pore initiation.

### 3.3 Stage III and IV

A steady state is reached as the density of pores is reduced. The disordered pores start to merge and pores parallel to each other and perpendicular to the surface start to grow. The current density decreases and when the final steady state is achieved, the current density stabilizes. A schematic representation of steady-state oxide growth and the chemical reactions involved in the process are shown in Fig. 4.

During this steady stage, the thickness of the barrier layer ($t_b$) is kept constant and the porous structure grows in thickness through the balance of two competitive mechanisms: alu-
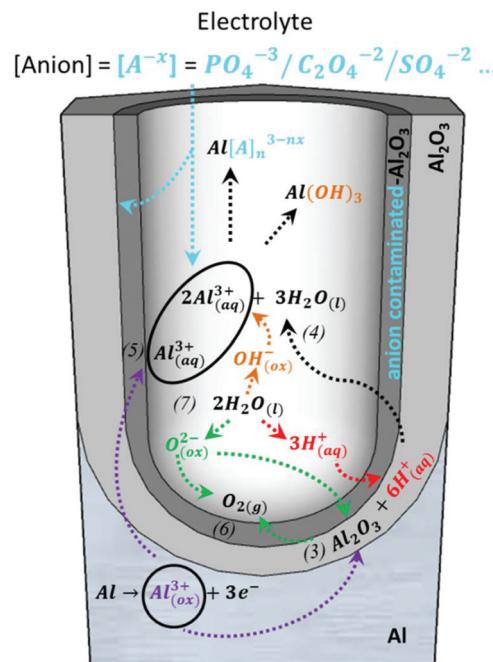


**Fig. 4** Chemical reactions of the species present in the acidic electrolyte during the anodization process: purple arrows point the route of the metallic aluminium of the substrate as it is oxidized towards the formation of $Al_2O_3$ or the direct ejection of the oxidized $Al^{3+}$ ions into the electrolyte, corresponding to reactions (3) and (5), respectively. The green arrows point to the inward migration of $O^{2-}$ species to form new $Al_2O_3$ (reaction (3)) from the dissociation of water molecules, according to reaction (7), and indicates the generation of oxygen bubbles as $O_{2(g)}$ is released, as described by reaction (6). The red arrows mark the dissociation of water into $H^+$ ions (reaction (7)) and the role played by these $H^+$ ions in the re-dissolution of the already formed $Al_2O_3$, as shown in reaction (3). The orange arrows show the dissociation of water into $OH^-$ ions (reaction (7)), which later react with the $Al^{3+}$ species present in the solution. The black arrows show the re-dissolution of $Al_2O_3$, as in reaction (4), and the formation of Al-based soluble complexes. The blue arrows mark the inward migration of the counteranions from the bulk electrolyte that binds $Al^{3+}$ ions in the solution to form water-soluble complexes and their incorporation in the $Al_2O_3$ of the outer walls of the pores.

minium oxide formation and dissolution of the oxide, as described by reactions (3) and (4), respectively. The formation of new anodic oxide is possible due to the diffusion of oxygen-containing ions and molecules ($O^{2-}$, $OH^-$, *etc.*) from the electrolyte towards the metal/oxide interface (reaction (7)). The $Al^{3+}$ ions travel through the barrier layer and are ejected to the electrolyte, as shown by reaction (5). Both the dissolved $Al^{3+}$ ions, according to reaction (4), and the ejected $Al^{3+}$ ions, as shown in reaction (5), now present in the electrolytic solution will form water-soluble complexes with the counteranions, $[A^{-x}]$, of the different electrolytes. Another important event is the incorporation of the counteranions on the surface of the pore walls in close contact with the electrolyte solutions, forming an anion-contaminated outer layer of alumina along the pores. Even though it is not yet completely understood, these anionic species play a crucial role in the development and self-arrange-

ment of the pores. All reactions are schematically represented in Fig. 4, and after a certain time, all the different reactions that are involved reach their steady-state value. This dynamic equilibrium between oxide formation and oxide removal taking place at the different interfaces has been studied under different perspectives to understand the mechanism that leads to pore formation and the steady-state growth stage, including Joule heat-induced dissolution at the pore base,[98,135–137] field-assisted oxide dissolution,[95,136,138] and more recently, the stress-induced plastic flow model[139–142] and the effect of the bubble mold model, which has been developed to understand the evolution of different pore morphologies during their growth.[143]

The first approximation, that is, Joule heat-induced dissolution at the pore base, was abandoned by Nagayama and Tamura back in 1968 upon calculating that the heating at the bottom of the pore was ~0.06 °C, and thus they considered it negligible.[144] Although other authors such as Mason[145] and Li and Zhang[98] found that the temperature increase of the bottom of the pores was about 25 °C, that is, several orders of magnitude higher, even this temperature is not enough to explain why the growth rate at the pore base is higher. Actually, Oh,[146] in 2010, based on the previous work from Hunter and Fowle,[147] showed that to explain the faster growth rate at the pore base based on the Joule heat, the electrolyte should be boiling. Thus, because of all these arguments, the idea of the Joule heating was ruled out.

O'Sullivan and Wood[95] developed an '*average field model*' in which growing pores of different sizes will experience different electric fields, and thus different dissolution rates. Through merging and self-arrangement of the pores, the electrical field experienced by each pore will balance to the same average electric field. Under this average field, the equilibrium of the growth rate is achieved for all pores. Several mathematical models were developed to describe this field-assisted oxide dissolution process. Most of them used the Laplace equation,[101,148,149] which assumes no space charge, to govern the potential distribution in the oxide film. At high electric fields (such as that maintained at the pore base), diffusive transport can be neglected since ionic conduction is the dominant mechanism controlling interface motion. These models were able to predict the linear dependence of the interpore distance (or cell size), $D_{int}$, with the applied potential.

This field-assisted model was modified to consider several experimental findings. For instance, in 2006, Houser et al.[150] demonstrated that the Laplace approximation to describe the interface motion violates two physical conditions that were experimentally observed, namely the requirement that the interface speed must be constant, and thus the morphology of both interfaces remains time-invariant during steady-state growth. Also, the requirement of current continuity along the oxide film, which controls the actual growth, being responsible for both the recession of the barrier layer at the bottom of the pores and the accumulation of oxides on the pore walls. The authors showed that when only the Laplace equation is used, and therefore no space charge is present in the model, two

effects occur, *i.e.*, an unrealistic increase in the electrical field from the pore bottom to the ridges and a difference in current density by 7 orders of magnitude between the metal-oxide interface and oxide-solution interface (violating the current continuity observed experimentally). This implies that a certain space charge in the oxide is necessary to maintain current neutrality in non-planar oxide films. Therefore, to avoid these inconsistencies, Houser et al., also in ref. 150, proposed a current continuity equation based on the interface kinetics, accounting for $Al^{3+}$ dissolution in the electrolytic bath and $O^{-2}$ migration into the film. After these findings, Su et al. presented a new mathematical model supporting the equifield strength empirical model, which was firstly described by O'Sullivan, but also including both the oxide dissolution and oxygen migration rates and in which the latter, determined by the water dissociation rate, plays a key role in the final porosity (the pore to cell size ratio).[151]

Subsequently, previous experimental studies employing [18]O isotopes tracers were carried out first by Siejka and co-workers[152] and later corroborated by Skeldon et al.,[153] which showed no appreciable oxygen dissolution from the film. Then, if there is no significant oxide dissolution occurring during steady-state pore formation, the recession of the oxide-solution interface had to be attributed to other phenomena. In this line of thought, other authors supported the relevance of the direct cation ejection mechanism, where the free volume left by the ejection of $Al^{3+}$ ions (according to reaction (5)) must be compensated by an inward movement of the oxide at the oxide-solution interface. This direct ejection of $Al^{3+}$ ions from the substrate towards the electrolyte reduces the efficiency of the formation process of porous alumina, as was proved by Takahashi and Nagayama.[154] They reported that about 40% of $Al^{3+}$ ions are lost to the electrolytic solution and do not contribute to the formation of porous alumina. It is worth mentioning that several other works support the direct cation ejection mechanism.[152,153,155]

Then, even though the field-assisted model describes the pore-growth process and oxide formation, several experimentally observed phenomena are not compatible with it. Thus, in 2008 a new model was proposed by Skeldon et al.,[139,156] who suggested a flow mechanism to explain the steady-state pore formation. In this model, the thickness of the barrier layer, $t_b$, is kept constant by the flow of oxide materials from the base of the pore towards the cell boundaries, as was experimentally observed from the flow pattern of tungsten (W) found along the pore walls in W tracer studies. This is the opposite of the field-assisted migration of $W^{6+}$ ions through the oxide towards the oxide-solution interface and their dissolution in the electrolytic bath. Moreover, this flow model is also supported by the stress-driven transport theoretical model proposed by Hebert and Houser,[140,141] in which ion migration is described by combining a mechanical stress gradient and an electrical potential. The model also incorporates the viscoelastic creep of the oxide. The calculated values using this model matched the experimental results (from stress measurements to tracer studies). The authors concluded

that the stress field driving the flow originates from volume expansion at the metal/oxide interface, different migration rates of $O^{2-}/OH^-$ species and $Al^{3+}$ ions, and incorporation of acidic anionic species from the electrolyte solution into the oxide.[141,142] It is also consistent with Sato's breakdown model,[157] in which the formation of porous alumina films was associated with continuous plastic deformation of the oxide.

Besides these theories on the pore evolution and pore growth mechanisms along the steady stage, after the nucleation initiates, there is another phenomenon that occurs in AAO nanopore membranes, which is self-ordering, that should also be understood to be able to control it. This ordering of the pores in a close-packed hexagonal arrangement also takes place at this stage. Jessensky[120] and Li[158] stated that stress is the driving force responsible for this alignment due to the repulsive forces between neighboring pores. Nevertheless, there is still research being done to fully understand how the different phenomena affect the actual formation mechanism and self-ordering of the pores, such as volume expansion and anion incorporation from the electrolyte solution. Both seem to linearly depend on the applied anodizing voltage,[159–163] whereas the latter, at least in the particular case of sulfur incorporation, seems to increase the plasticity of the oxide since the breakdown limit of the oxide before cracking under mechanical stress is increased.[163] This can open new regimens under high stress (due to higher volume expansion of the oxide) for the self-ordering formation of nanoporous alumina.

Recently, an extended version of Hebert and Houser's stress-driven plastic flow transport model was proposed,[164–167] which also explains this self-ordering. In this case, the internal stresses developed in the oxide film and metal-oxide interface discussed above will also be responsible for the ordering of the pores. It accounts for volume expansion at the metal-oxide and oxide-solution interfaces due to the formation of $Al_2O_3$ and the incorporation of oxyanions, respectively, in the generation of stress driving the oxide flow. The dynamics of the interfaces is described here by dynamic boundary conditions. A non-planar topography oxide surface, inducing non-uniform current distributions at the interfaces, was also accounted for in the model. Generally, the model was able to predict the generation of tensile and compressive stress gradients from the oxide bulk towards the metal-oxide and oxide-solution interfaces, respectively, under high electrical fields, to balance the presence of $O^{-2}$ or $OH^-$ ions (increasing the oxygen flux) needed at the interfaces to maintain the volume balance boundary conditions established at each of them. They observed the formation of nanometer-thick layers of interfacial stress depending on the local current density, followed by induced stress relaxation due to the oxide flow. At high electrical field conditions (under which self-ordering is achieved), the developed stress at the metal-oxide interface is tensile. $Al^{3+}$ ions are consumed at a faster rate (aluminium oxidation is enhanced) than that of oxygen migration towards this interface. Tensile stress is generated at this interface to increase the volume flux of oxygen ions. However, in a later study, they suggested that the volume change at this interface is relatively small and the gen-

erated flow at the metal-oxide interface can be considered negligible. Thus, the motion of this metal-oxide interface is mainly controlled by electrical migration.[167]

In the same work, the motion of the oxide-solution interface is described as driven by oxide flow generated from interfacial stress. At the solution interface, strong adsorption of anionic species occurs, which coordinates with $Al^{3+}$ surface ions, thus blocking oxide formation at this interface. Instead, $O^{2-}$ ions incorporated from the solution are forced to migrate within the oxide and interfacial compressive stress is needed to enhance the migration rate of oxygen ions. Their studies revealed that pattern formation is associated with a critical efficiency value for oxide formation, $\varepsilon_O$, just slightly higher than that of the transport number of oxygen ions, $t_O$, by migration. Hence, compressive flow in close competition with oxide formation at the pore base is responsible for the formation of patterns of stable pores. The dimensionless parameter, $\omega_s$, which controls oxide formation is then:

$$\omega_s = \varepsilon_O - t_O \qquad (8)$$

In this competitive situation, a pattern emerges at the surface of the solution interface with a characteristic wavelength, $\lambda_c = 2\pi h/k_c$ (where $h$ is the oxide length, and $k_c$ is a spatial dimensionless perturbation parameter), the value of which determines the interpore distance, $D_{int}$, between self-ordered pores.

The inset in Fig. 5a shows that for negative values of $\omega_s$ ($\varepsilon_O < t_O$), there is no perturbation peak, $k_c$, indicating that the formation of pores is not favorable, resulting in non-porous
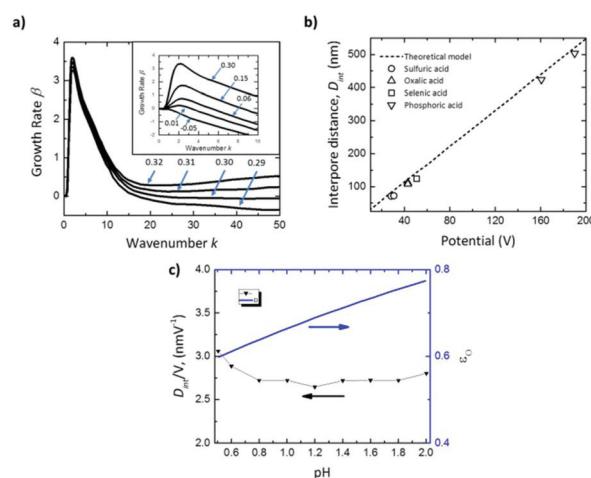


Fig. 5 Results of linear stability analysis of the anodization model. (a) Effect on growth rate dispersion curves for Al of the parameter $\omega_s$, controlling the oxide formation rate at the oxide-solution interface near the critical value of 0.30, above which the film is unstable at all wavenumbers. Inset shows the dispersion curves below the critical value $\omega_s < 0.30$. (b) Comparison of predicted (solid line) and measured interpore distance, $D_{int}$, for anodic alumina grown in various solutions (black open symbols). (c) pH dependence of predicted $D_{int}$ and anodization efficiency, $\varepsilon_O$, for Al anodization at 10 mA cm$^{-2}$, for comparison to pH-independent $D_{int}$ reported in the literature.[102,103] Reprinted with permission from ref. 167. Copyright © 2020 Elsevier.

planar films. Intermediate values of $\omega_s$ ranging from 0 to 0.3 correspond to efficiencies, $\varepsilon_O$, between 0.60–0.90, which are in good agreement with the experimental efficiencies for different acids.[168–170] In this range, pattern formation is promoted. The transport number of oxygen ions was set as 0.60, as reported in the literature.[154] For $\omega_s$ values higher than 0.3 ($\varepsilon_O \gg t_O$), the oxide is unstable (Fig. 5a), the growth rate increases at large wavenumbers, and hence no ordered pores with wide pore distributions will be formed in this regime.

This model also agrees well with the observed experimental dependence of the interpore distance, $D_{int}$, with the applied voltage, as can be seen in Fig. 5b. In this figure, experimental measurements of the pore spacing are plotted together with the calculated values from $k_c$ (solid line) according to the expression $D_{int}/V = 2\pi h_V/k_c$, where $h_V$ is the anodizing ratio (ratio of the barrier layer thickness to cell voltage), which has been reported to be 0.1 nm V$^{-1}$, independently of the electrolyte composition. Moreover, they were able to predict using the flow model the weak dependence of the inter-pore distance on the pH of the solution, which has been also experimentally reported[102,103] (Fig. 5c).

Finally, the oxygen bubble mold model accounts for the effect that the oxygen bubbles that are produced as a side reaction during anodization have on the morphology of the anodic oxide layer.[143,171] As will be seen in section 5, besides pores with parallel walls, different pore-wall morphologies can be obtained, such as serrated walls[172,173] and diameter modulated pores (also called bamboo-like structures),[174] and these morphologies can be understood based on the oxygen bubble mold model. As hinted by its name, this model considers the oxygen generated while oxidation is occurring during anodization. Then, the generated oxygen bubbles are presented as molds for the formation of a semi-spherical barrier layer at the bottom of the pores. This model is also related to the previous one because the plastic flow of the produced oxide is enhanced by the high-pressure areas under the oxygen bubbles, where there is also a higher electric field. Then, there is a plastic flow from the bottom of the pores towards the pore walls, which is favored by the bubbles. In 2008, Zhu K *et al.* presented work on how the oxygen bubble mold effect can be responsible for morphologies such as serrated walls,[143] where the formation of further oxygen gas bubbles at the pore wall during the pore growth results in the formation of new pores with a certain depth within the oxide layer, which gives the resulting serrated structure.

It is worth mentioning that the formation of some special morphologies that have been observed under certain anodization conditions, such as ordered nanofibers or nano-petals,[175] can only be explained with both the oxygen bubble mold and plastic flow models. Nevertheless, research on the full understanding of how the hexagonal ordering of the pores is achieved is still underway. Studies such as that presented in 2020 by Heinschke *et al.*[176] and the recent work of Pashchanka[177] also presented in 2020 are examples of the current research in this direction. In the former, a mathematical model that explains how the microscopic processes involved in the formation of the pores are related to the entropy of the system that generates because of ion migration is developed. A clear relation between the entropy production and the porosity number, $p$, and hence the cell size, was established. Moreover, this model considers the accumulation of charge due to the incorporation of anions present in the electrolyte at the oxide/electrolyte interface and responsible for the generation of ionic flow in the interface proximity as attractive Coulomb forces compete with repulsive ones between charged ions of the same sign. This ionic flow is produced as a result of the applied anodizing potential in the electrochemical cell and is responsible for the formation of convection cells, which ensure the hexagonal arrangement of the pores. This study is based on the empirical model proposed by Pashchanka *et al.*,[178] which predicts the optimum anodization conditions required to achieve the maximum degree of order of the porous structure and where the porosity number is the determinant factor. In the latter, Pashchanka, after studying the different theoretical models proposed in the literature for pore-formation, presented a step further in the study of the self-organization of the pores in AAOs and, modifying the conventional experimental conditions, achieved a long-range ordering in hierarchically organized cells directly on the surface of aluminium.

Thus, work still needs to be done to deeply understand the actual nature of pore formation, self-ordering, and anodization evolution. Any step in this direction, as shown in this section, opens the door to further developments and new morphologies in AAO nanoporous structures.

# 4 Anodization regimes

Regardless of the existing discrepancy between the different theories that have been developed to try to explain the mechanism behind the formation of the porous anodic oxide structure as opposed to barrier-type oxide growth and the phenomena that govern the self-ordering of the pores, the generated electrical field across the barrier layer (and thus applied anodizing potential) is a determining factor for oxide dissolution, Al$^{3+}$ ejection and stress generation due to volume expansion at the metal/oxide interface. Therefore, an important effort has been done in this direction through the optimization of the anodizing potential. Regarding this parameter, two different regimes can be distinguished, *i.e.*, mild anodization (MA) and hard anodization (HA), which will be described next.

## 4.1 Mild anodization

Mild anodization conditions refer to anodization in a potential range below the breakdown potential of the forming oxide layer. Above this breakdown potential, typically the burning and cracking of the oxide or oxide formation with an increasing number of growing defects occurs.

Self-ordering of the nanoporous structure of anodic alumina under this regime was first reported by Masuda *et al.*[179] in a two-step anodization process using 0.3 M oxalic
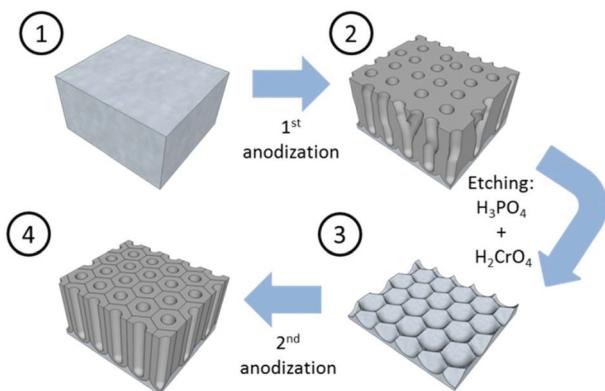
**Fig. 6** Schematic sketch of the steps involved in the two-anodization process developed by Masuda *et al.*[179] to obtain highly ordered nanoporous alumina.

acid, as described in Fig. 6. During this process, the first anodization step was carried out at 40 V and 0 °C for 24 h. After this long anodization period, the self-arrangement of the pores at the metal/oxide interface was achieved. The end of this step is the removal of the oxide porous layer formed by chemical etching in 6 wt% $H_3PO_4$ and 1.8 wt% $H_2CrO_4$ mixed solution. Then, the surface of the remaining aluminium substrate presents a hexagonal pattern structure, which will facilitate the growth of highly ordered pores in the direction normal to the substrate. The second anodization step was performed under the same conditions as the first anodization. Later, the optimized conditions for the growth of highly self-ordered systems in 0.3 M $H_2SO_4$ and 0.3 M $H_3PO_4$ were reported to be 25 V (ref. 117) and 195 V,[116] respectively, at 0 °C, and correspondingly the cell sizes of 65 nm in sulfuric acid and 500 nm in phosphoric acid (as recorded in Table 1) were achieved. More recently, other acidic systems have been studied and new conditions have been discovered, which allow self-ordering of pores with a wide range of cell sizes (see Table 1).

### 4.2 Hard anodization

Hard anodization is performed under limited conditions above the breakdown potential, which is normally used to obtain thick AAO films in short anodization times. As previously mentioned, burning, cracking, or defects over the oxide appear under this regime and normally no control of the structural parameters of the pores, such as pore diameter and interpore distance, was possible to be achieved until quite recently. To improve the control and avoid the breakdown of the oxide under a high anodizing potential, one approach is to use additives, which will improve heat dissipation (*e.g.* by adding ethanol)[5,6] or increase the electrical resistivity of the electrolyte solution, thus increasing the limiting breakdown potential (*e.g.* by the addition of ethylene glycol).[118] Also, mixed solutions of acids have been successfully used in HA anodization conditions.[113,123,125,126] However, the most popular procedure involves a first anodization step under MA conditions followed by a gradual increase in the anodizing potential until reaching

the HA regime.[2,4,113,121,123,125,126] Details of the structural parameters of the AAOs fabricated under HA conditions are recorded in Table 1.

When very high voltages are applied, besides porous growth, the different cells can be cleaved due to the high rate of $O^{2-}$ and $OH^-$ ions travelling through the barrier layers, creating tensile stress near the cell ridges, which has been observed experimentally by the formation of nanotubes, for instance in ref. 140. Also, a variation in the cell wall thickness when HA in oxalic acid is performed at ultra-high voltages has been reported, which is related to the oxygen gas bubbles created at the metal-oxide interface.[171] Also, in this regime, the formation of a certain amount of $Al(OH)_3$ has been observed, which is another important difference with MA, and thus, the mechanisms governing this regime are different.

In 2015 Vega *et al.*[5] proposed a specific mechanism for the formation of pores under HA conditions, which supposes a breakthrough in this particular regime, where the starting point for research was oxide burning and cracking. This mechanism was based on diffusion-limited oxide growth due to fast oxide formation under HA conditions, which hinder the diffusion of ions from the bulk electrolyte solution, oxalates species in their experiments, along the length of the pores and towards their base. They suggested that under this regime, oxide growth at the oxide/electrolyte interface becomes relevant (as in the case of non-porous-type anodic oxide) due to the limited diffusion of oxalate species (phosphate or sulfate ions, depending on the electrolyte), thus resulting in a lower concentration of these species available at the pore bottom to react with the $Al^{3+}$ ejected ions and form water-soluble molecules. Instead, the ejected $Al^{3+}$ ions will react in a higher proportion with water molecules, forming non-soluble complexes that finally contribute to the formation of new $Al_2O_3$ at the oxide/electrolyte interface. This phenomenon is not considered during the formation process of porous alumina films under MA conditions. An increase in the thickness of the barrier layer, $t_b$, because of the re-deposition of $Al_2O_3$ at the pore base was expected.

By neglecting the terms associated with migration and convention contributions to the ionic transport of the Nernst–Planck equation, and assuming a linear concentration gradient along the pores, as shown in Fig. 7a, (with the form $C(x) = C(0) + [C(L) - C(0)]x/L$, where $C(0)$ is the concentration of ions from the bulk electrolyte present at the pore base, which is approximated to 0 and $C(L) = C_0$ takes the value of the initial concentration of the bulk electrolyte), they obtained an inverse relationship between the current density and the thickness of the oxide membrane according to the following equation:

$$j_{DL} = |zFJ| = \frac{zPFDC_0}{L} \tag{9}$$

where $j_{DL}$ is the diffusion-limited current density, $J$ is the ionic flux of a certain ionic species, $D$ is the diffusion coefficient of the specific ion of interest, $C_0$ corresponds to its concentration at the pore bottom and $z$ its charge number. $P$ and $L$ refer to
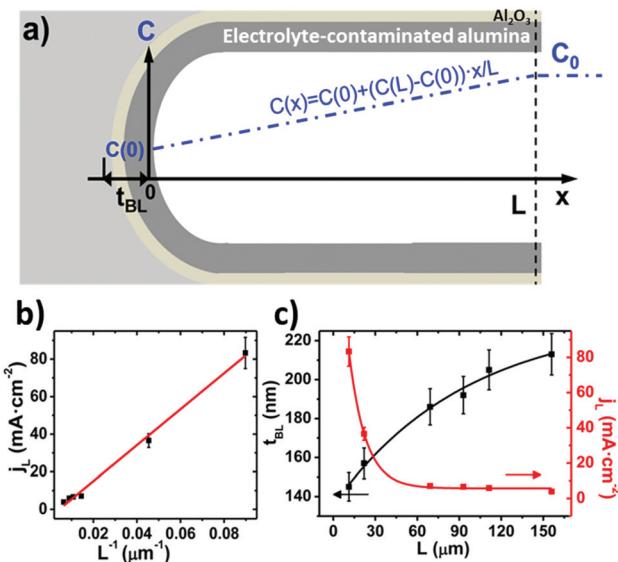
**Fig. 7** (a) Linear profile of the concentration gradient along the pore length. (b) Fitting of the final anodization current density, $j_L$, as a function of the inverse of the total membrane thickness, $L^{-1}$, obtained for H-AAO samples anodized at 120 V in 0.3 M oxalic acid electrolyte. (c) Dependence of the barrier layer thickness, $t_b$, and limit current density, $j_L$, on the total thickness of the alumina membrane. Reprinted with permission from V. Vega, J. García, J. M. Montero-Moreno, B. Hernando, J. Bachmann, V. M. Prida and K. Nielsch, Unveiling the Hard Anodization Regime of Aluminum: Insight into Nanopores Self-Organization and Growth Mechanism, *ACS Appl. Mater. Interfaces*, 2015, 7(51), 28682–28692. Copyright © 2015 the American Chemical Society.

the porosity and thickness of the nanoporous membrane, respectively, and *F* is the Faraday constant.

Experiments confirmed the behavior of the current density described by eqn (9), as well as the predicted thickening of the barrier layer with the total thickness of the oxide membrane. As the thickness of the barrier layer increases, the generated electric field across the layer decreases (Fig. 7c). The migration of $O^{2-}$ and $OH^-$ species across this oxide barrier is reduced, and thus it is the current density. They observed experimentally the linear dependence of the last current density recorded value, $j_L$, and the inverse of the final thickness of the AAO film, $L^{-1}$ (Fig. 7b), in agreement with eqn (9).

# 5 Different morphologies of the porous structure. Influence of the anodization conditions

The understanding and control of the anodizing conditions make it possible to obtain nanoporous alumina membranes with certain pore diameters (with low dispersion in size), ordering, and pore-lengths. The next natural step in the anodization of aluminium is the development of new fabrication techniques, modifying the fabrication conditions, which provide novel pore architectures. Among them, we will briefly describe the most relevant ones, including branched pores,

where one pore is divided into others or the other way round, modulated diameter nanopores, where anodizing pulses are applied alternating between the MA and HA anodization regimens while forming a porous structure, and finally, 3D porous structures, where the conditions are highly controlled over time and can give rise to nanopore structures with interconnected pores.

Furthermore, pre-patterning treatments of the aluminium surface by direct indentation methods such as focus ion beam (FIB) lithography,[180–184] using the scanning probe of an Atomic Force Microscope (AFM)[185,186] to generate an indention on the Al surface, interference lithography,[187] reactive ion etching (RIE),[188,189] and through the combination of lithographic processes and the use of resins[190,191] or employing AAO and PMMA as masks[192,193] followed by wet chemical etching; or by indirect impression techniques based on imprinting molds[194–198] employing, for example, nanoimprint lithography technology; are used to produce long-range highly ordered nanopores with a fixed unit cell size, reducing the number of anodizing steps to achieve perfect order. However, for this goal, the first approach is time-consuming and expensive, while the second route has a limitation of the area of the fabricated mold of 1 mm$^2$ for imprinting. Besides the high order of the pores obtained by these means, the typically hexagonal geometry of the unit cell can be altered, producing new morphologies with pores in a square and triangular arrangement.

## 5.1 Branched nanoporous structures

Mainly, two different approaches have been developed to achieve branching of stem pores, namely through non-steady-state and steady-state anodization. During steady-state anodization, the anodizing voltage decreases accordingly to the equal-area model, which states that the total pore area of the template is invariant, hence branching of the stem pore into *n* smaller in diameter pores that will follow the relation $d_2/d_1 = 1/\sqrt{n}$, which considers the conservation of the pore area. $d_1$ and $d_2$ are the diameter of the stem pore and the diameter of the *n* smaller branched pores, respectively. According to the previously established linear relationship between pore diameter with the anodizing potential (see section 2, eqn (1)), the equal-area model can be extrapolated to the anodizing voltage giving a reduction of the original voltage, $V_1$, by a factor of $1/\sqrt{n}$. In this regime, to obtain *n* Y-junctions, the voltage is systematically reduced in $1/\sqrt{n}$ steps. Each step will be extended over time until a steady state of the current density is reached under the new anodizing conditions. To reduce the duration of these steps, researchers followed different anodization routes, including chemical etching of the barrier layer down to the correspondingly new thickness of this layer under the decrease of the anodizing voltage between each branching step[199–202] and a change in the electrolyte solution to better suit the new anodizing conditions to be applied.[200,203] Sousa *et al.*[200,204] studied three cases as follows: (1) successive branching without intermediate steps (which requires long stabilization periods); (2) incorporation of an
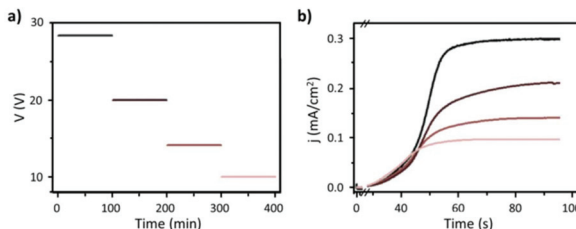
**Fig. 8** Steady-state anodization: (a) recorded $V(t)$ reduction from 28.4 V to 10 V by a factor of $1/\sqrt{2}$ to obtain two-, three- and four-generations of Y-branched pores. (b) Density current, $j(t)$, transients with a decrease in the $j(t)$ values due to the reduction of the applied potential, and the anodization time is extended during each voltage reduction stage until the anodization density current reaches a new stable value. Reprinted with permission from ref. 204. Copyright © The Royal Society of Chemistry 2012.



**Fig. 9** (a) Schematic illustration and (b) actual SEM images of multi-branched pores fabricated in succeeding tiers. Top view (top image) and cross-view (bottom image). Reprinted with permission from ref. 201. Copyright © 2008 WILEY-VCH Verlag GmbH & Co. KGaA, Weinheim.

intermediate etching step between each branching process; and (3) switching of the electrolyte solution depending on the anodizing voltage to be applied. Accordingly, anodization was initially carried out in 0.3 M oxalic acid solution, and then the applied potential was sequentially reduced by a factor of $1/\sqrt{2}$, as shown in Fig. 8a and b. In another set of experiments, the same anodization process was reproduced; however, a chemical etching step in 0.1 M phosphoric acid was implemented between successive branching to shorten the time consumed in each anodizing step. After thinning of the barrier layer to a value corresponding to that of the applied potential (according to the expression $t_b = \gamma V$), the generation of branched pores occurred immediately and the duration time of the anodizing steps was reduced. However, the resulting branched structure was over etched, since chemical etching collaterally causes the widening of the pores, and extreme enlargement of the pore results in the collapse of the porous AAO films. To overcome both issues, namely over-etching and long duration times of the anodization steps, in a third experiment, the electrolyte solution was changed to 0.3 M sulfuric acid.

Nevertheless, regardless of the shortcomings encountered, hierarchical multi-branched pores in succeeding tiers have been successfully fabricated if etching of the barrier layer is performed between each branching step.[201] Fig. 9b shows the top and cross-sectional views of a three-tiered branched pore structure. The fabrication process is as follows: the 1$^{st}$ anodization in 0.3 M phosphoric acid at 130 V for 30 min and a subsequent 50 min chemical etching step, followed by a 2$^{nd}$ anodization in 0.15 M oxalic acid at 80 V for 3.5 min and a 90 min chemical etching step, and a subsequent 3$^{rd}$ anodization in 0.3 M oxalic acid at 50 V for 15 min and a 40 min chemical etching step. Other authors also defend the need to add a chemical etching step of the barrier layer before variation of the anodizing voltage to eliminate the competitive growth of branched pores. Competition between stem pores or branched pores occurs due to the non-uniform dissolution of the barrier layer during the different anodizing steps and non-uniform field strength distribution at the pore base. Then, the pore growth rate of certain pores (or branched pores) occurs over
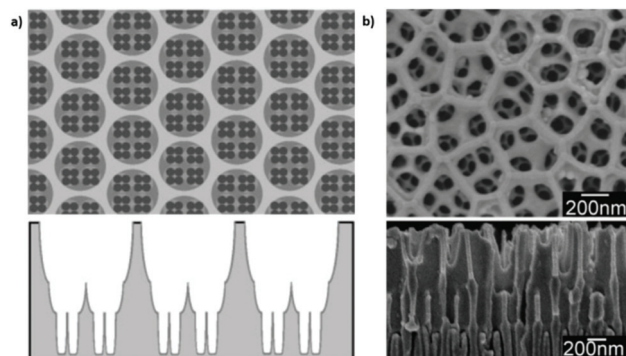
the others. The etching of the barrier layer enables steady-state growth to be reached more rapidly under the new anodizing conditions, thus avoiding the non-uniform dissolution of this barrier layer occurring during the long periods taken to reach the new steady-state when no previous etching is performed.[202]

In contrast to the voltage-control method described above, Guo et al.[205] reported a current-control method for the fabrication of highly homogeneous triple-branching pores, where the homogeneity of the branching pores is improved by controlling the applied current against the reduction of the applied potential. More complex branched structures have been grown by alternating between the voltage and current control anodizing steps.[206]

Similarly, Zakeri and co-workers[207] proposed a model where branching of pores occurs over non-flat aluminium surfaces and without the need to reduce the anodizing voltage through the curving and subsequent merging of the growing pores over edges, notches, and curved sites.

Recently, in 2016 Jin et al.[208] developed three different types of complex branched structures by combining the steady-state growth of branched pores on pre-patterned curved aluminium substrates, where tree-like porous structures are formed, as previously described by Zakeri et al.,[207] at the boundaries of the pattern cells. Specifically, type 1, 3D interconnected branched structure; type 2, self-supported AAO nanowires structure, and type 3, which is what the authors called a supporting AAO skeleton structure. To obtain 3D interconnected branched pores (type 1 structure), a periodic anodizing potential was applied alternating between 50–30 V in 0.3 M oxalic acid, followed by a 35 min etching treatment. Types 2 and 3 were grown under a constant voltage (30 and 40 V) and different etching times 31–33 min (AAO nanowires were formed) and 43 min for the complete dissolution of these nanowires, respectively.

Serrated branched porous structures associated with oxygen evolution when applying different voltage steps have also been reported by several authors.[143,172,173] The growth of serrated

pores in the oblique direction along the vertical walls of the pore channels cannot be assessed by the field-assisted dissolution theory at the pore bottom of perpendicular pores (concerning the aluminium substrate) due to geometric considerations. Therefore, the formation mechanism of serrated pores combines the previously proposed field-assisted flow model by Skeldon *et al.*[139,156] with the oxygen bubble mold effect. During anodization, oxygen bubbles trapped within the oxide barrier layer are generated, and current density accumulates around them. Consequently, $Al_2O_3$ formation is promoted at these local points, where the field strength is increased, a protuberance is formed and the oxygen is released from the oxide. Then, at the steady-state growth stage, protuberances are pushed towards the vertical walls by oxide flow deformation. However, this mechanism is only enhanced under certain conditions, such as at elevated anodizing temperatures at which the increase of the current density induces higher oxygen evolution and when the Al substrate is placed vertically inside the electrochemical cell, which seems to promote the formation of serrated branched pores aligned on one side of the walls of the vertical channels.

In the case of non-steady state, the anodizing potential exponentially decreases (Fig. 10a), and potential reduction steps are applied before the steady stage can be reached at each anodizing step. The transient current *versus* time curves show a tooth-like profile, as can be seen in the inset of Fig. 10b. The current drops as the applied potential is reduced and then starts to increase with time. However, the next potential reduction step will be applied before current stabilization is achieved (Fig. 10b).

Cheng *et al.*[209] proposed a specific mechanism for the formation of branched pores under the conditions described above. They stated that when the anodization process is kept in a non-steady state, the oxide formation and dissolution rates never reach an equilibrium balance and negative charges (coming from oxygen-containing species) will tend to accumulate in the oxide layer up to a threshold accumulative charge. Then, discharging of the negatively charged oxide layer will

occur, leading to the generation of non-uniform current pathways running through the oxide. Field-assisted dissolution is induced this way, resulting in the formation of branched pores. Consequently, the pore diameter of the branched pores is not proportional to the anodizing potential with a root or tree-like form (inset Fig. 10a).

In addition to the electrical field effect, the authors also paid attention to the role played by mechanical stress. One specific morphological characteristic of this type of branched pores is their uneven morphology, where some nodes can be found along with individual pores. Furthermore, when branching of a pore takes place, the stem pore will always grow into two pores smaller in diameter. This was explained as a consequence of the strong repulsive forces between neighboring pores. Repulsive forces due to space limitation reduce the ramification of a pore into only two branches if they manage to overcome these forces. If not, a node appears. In this competitive branching pore formation mechanism, pores suddenly change direction, looking for space to grow and deviate from the perpendicular direction concerning the substrate.

A slightly different concept of the branched structure was that presented in 2018 by Hashimoto *et al.*, where the authors fabricated a membrane they described as a hierarchical structure of macropores with a pore wall full of mesopores[210] by anodization of aluminium in phosphoric acid, and then, a heating process at 1400 °C produced aluminium phosphate nanoparticles, which were segregated from the alpha-alumina matrix formed after the annealing. Then, these nanoparticles were dissolved in concentrated hydrochloric acid, giving rise to the combination of straight macropores (with diameters of around 220 nm) with mesopores with a diameter in the range of 20–80 nm present inside the macropore walls.

All the branched structures described in this section can be later used for the fabrication of branched nanowires (NWs) and nanotubes (NTs) for several practical applications in different fields, namely electronics, optics, energy harvesting, and biotechnology. More details of the actual applications of Y-branched NWs and NTs will be described in section 6.

## 5.2 Nanopores with modulated diameters

To produce changes in the diameter while the nanopores are being formed, there are many different possibilities, such as using a modified electrolyte with additives such as ethylene glycol to modify its viscosity,[212] combining constant voltage anodization and chemical etching,[213] and using the HA method with very high applied voltages,[214,215] where fluctuating diameters along the pore length are obtained. In the last few years, the two most commonly used methods are the change in electrolyte while performing the anodization[203] (Fig. 11a and b) and maintaining the same electrolyte, while varying the applied voltage. This change in voltage can be done in such a way that periods of mild anodization and hard anodization are applied during the anodization (this technique is known as pulsed anodization).[211] The latter permits the fabrication of subsequent HA and MA layers of alumina (Fig. 11c and d), and thus, the combination of their properties, includ-
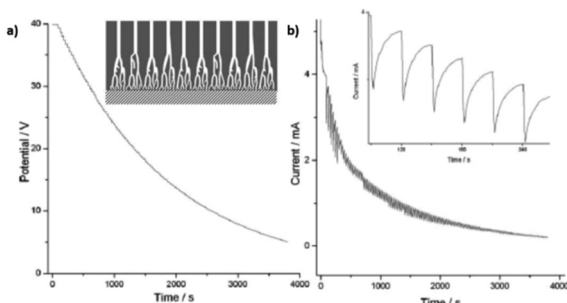


**Fig. 10** (a) Potential-time and (b) current-time transients profiles recorded in non-steady-state anodization. Inset in (a) is a schematic illustration of the tree-like branched pores. Inset in b is the magnification of the current curve for a clear view of its tooth-like profile. Reprinted with permission from ref. 209. Copyright © 2007, The Royal Society of Chemistry.
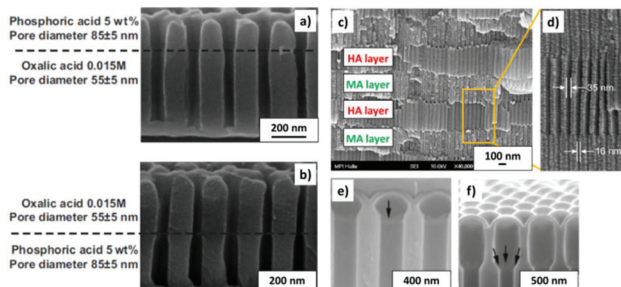
**Fig. 11** (a) and (b) Nano-funnels and inverted nano-funnels (as named by the authors). They are formed by anodizing firstly in 5 wt% phosphoric acid followed by anodization in 0.015 M oxalic acid and *vice versa*. The pore spacing is 200 nm and the dotted line shows the change in pore diameter. Reprinted with permission from ref. 203. Copyright © 2007 WILEY-VCH Verlag GmbH & Co. KGaA, Weinheim. (c) and (d) SEM cross-sectional view of AAO with modulated pore diameters by pulsed anodization in 0.3 M sulfuric acid at 1 °C. Each cycle consisted of an MA pulse (25 V for 180 s) and an HA pulse (35 V and 0.5 s). Reprinted with permission from ref. 211. Copyright © 2011 Elsevier Ltd. All rights reserved. (e) and (f) Cross-sectional SEM micrographs of bottle-shaped pore channels with two sections of significantly differential pore diameters after an annealing treatment at 500 °C, followed by re-anodization in phosphoric acid up to a specific current density (of 0.5 mA cm$^{-2}$ and 6 mA cm$^{-2}$, respectively) and then etching for 32 min.

ing alternating layers of different porosity and refractive index.[211,216] With this method, high control over the shape of the modulations and their position can be achieved. Currently, these structures are being widely used as photonic structures, as will be further discussed in section 7.

Furthermore, controlling the profile of the periodic pulsed signals, meaning the amplitude and period of the applied pulse, the shape of the pores can also be modulated, and pores with a desired geometry can be fabricated. Hence, voltages or current pulses with tooth, sinusoidal, triangle, or square profiles result in different pore geometries. This process is known as cyclic anodization and differs from the pulsed anodization technique in a slower transition from MA anodization conditions to HA anodization, which allows better control over the shape of the modulated pores.[216,217] It has also been reported that cyclic anodization technique, during which the anodizing voltage (or current) is gradually increased up to HA conditions, is better suited to produce modulations along the pores when using oxalic and phosphoric electrolytes due to the longer recovery times required for both electrolytic solutions until the current density stabilizes across the barrier layer as the applied potential is increased.[199,218] The forming oxide barrier layer is thicker in phosphoric acid and oxalic acid solutions than sulfuric electrolytes, and hence if pulsed anodization is used, where the transition between MA and HA regimens happens at a faster rate, a current steady state is not reached during the applied HA pulses and the changes of the anodizing voltage (or current) do not result in the actual modulation of the pore structure for the former cases. The barrier oxide layer of sulfuric AAO membranes is thin enough,
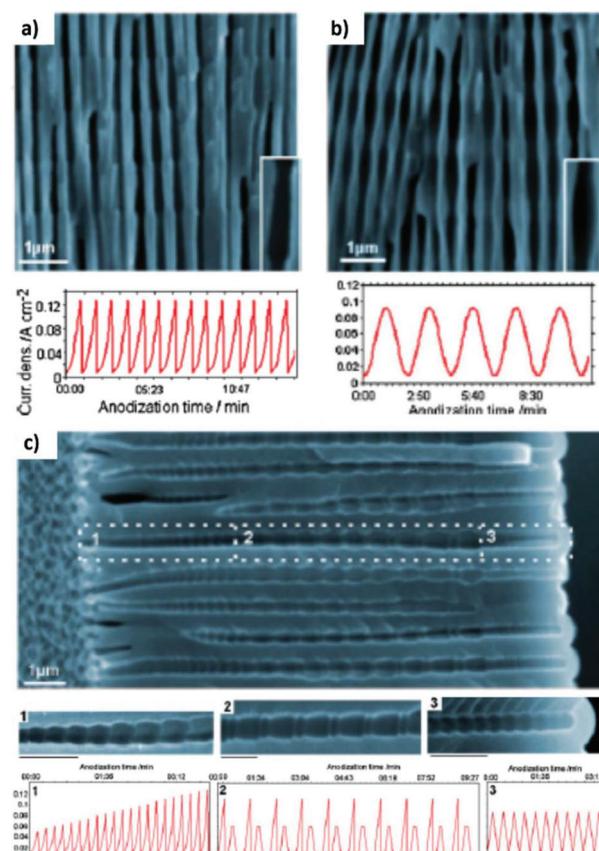


**Fig. 12** Controlling the shape of the AAO-modulated pore by cyclic anodization. Current–time curves and corresponding SEM images of AAO pore structures fabricated by galvanostatic anodization in 0.1 M phosphoric acid at −1 °C using different current signals. (a) Asymmetrical current signal with an exponential saw-tooth-like profile with asymmetrical bottle-neck shaped pores. (b) Symmetric sinusoidal current signals showing pore segments with spherical shapes. (c) Combination of (1) asymmetrical current signal with an exponential saw-tooth-like the profile of increasing amplitude, (2) alternating asymmetrical (saw-tooth-like profile) and symmetric (triangular) current signals, and (3) final series of symmetrical triangle pulses for the fabrication of AAO with more complex pore architectures. Reprinted with permission from ref. 217. Copyright © 2009 Wiley-VCH Verlag GmbH & Co. KGaA, Weinheim.

and thus control over the pore geometry can be attained through pulse anodization.

Fig. 12 shows the modulated pores with different shapes fabricated by cyclic anodization processes. When asymmetric current pulses with an exponential tooth-like profile are applied, asymmetric pores are also obtained with an asymmetrical bottle-neck type geometry, as can be seen in Fig. 12a. As expected, with symmetrical sinusoidal pulses, the resulting pores present an asymmetric spherical shape (Fig. 12b). Finally, a more complex multilayer pore structure with different geometries can be obtained by combining tooth-like and triangular pulses, as shown in Fig. 12c. Insets 1, 2, and 3 show in more detail the different features of the modulated

pores obtained by the different profile periodic pulses that appear underneath each of them.

In both cases, pulsed anodization and cyclic anodization, the thickness of each segment can be controlled by the duration of each pulse. However, the mechanism behind the change in the geometry of the modulated pores is not yet well understood. It seems that the key factor is the difference between oxide formation and oxide dissolution rates as the anodizing conditions are varied (HA/MA anodization regimens) and that the electric field continuously changes throughout the process. Comparing the curvature of the barrier layer formed during the different stages of the cyclic anodization process (HA, MA and the transient time in between) from the SEM images taken at each of them, it was observed that during the HA condition, the barrier layer possesses a more ellipsoidal shape, while in the other two stages, the barrier layer has a more circular geometry. These experimental findings indicate that the different formation and dissolution rates at each of the different stages of the periodical pulses indeed affect the shape and morphology of the resulting pores.[217]

Other combinations of anodization conditions, etching, annealing, *etc.* have also been explored to give rise to pore morphologies such as bottle-shaped pores in the base of the pores, like in ref. 219, (see Fig. 11e and f). During this process, the prior annealing treatment reduces the etching rate of the pore walls, while that of the barrier layer is enhanced by the subsequent re-anodization processes, and the preferred chemical etching around this oxide layer (probably due to structural changes induced by the annealing treatment) results in the generation of scalloped pored tips at the bottom of narrower channels (bottle-shaped).

Another approach involves temperature-modulated hard anodization, which was developed by Bayat and co-workers.[220] In this process, the current density, and hence pore diameters, were varied by temperature modulation under hard anodization conditions. Anodization was carried out in 0.075 M oxalic acid solution containing 10 v/v% ethanol at −4 °C, and 130 V starting potential. After 10 min the anodizing voltage was gradually increased to 230 V, and at this potential, the anodization was extended for 1 h. During this time, the temperature was periodically increased, which in turn caused an increment in the current density, and then decreased again back to the steady state. Using this method, cylindrical pores with modulated diameters were successfully fabricated, with narrow segmented pores of 47 nm in diameter and the widest segments of 130 nm.

A recent development, which is linked with this pulsed anodization technique, is the fabrication of ultra-short anodic alumina nanotubes (AANTs), where galvanostatic pulsed anodization is performed using ultrashort pulses of HA (of one second) in an electrolyte with a certain amount of ethanol. Control over this process is achieved by the optimization of three factors, which are deeply intertwined, *i.e.*, current density, HA duration, and heat generation. Short HA pulses of 1 s are required to produce ultra-short AANTs; however, when these HA pulses are shortened incompletely, voltage recovery occurs (in other words, the maximum HA voltage is not

reached) and modulation of the pores is not observed. HA anodization is associated with the large evolution of heat compared to MA and accelerating oxide dissolution rates. To favor the generation of modulation due to the thinning of the pore wall structure under fast applied HA pulses, heat generation must be enhanced under a certain fixed current density. Accordingly, the authors found that the addition of ethanol, while the electrolyte was kept above 0 °C, did not contribute to heat dissipation, but on the contrary, contributed to increasing it. Besides, heat generation produces weakened conjunctions along cell boundaries as well as weak MA/HA interfaces, which can be then cleaved and individually separated after acid etching and subsequent sonication of the structure. Consequently, well-defined AAO nanotubes were produced.[221]

### 5.3 3D porous structures

These structures provide a further step to the modulated nanoporous structures considering that the fabrication principle is similar, that is, a periodic change in the anodization conditions switching between MA to HA by either pulsed or cyclic anodization. Nevertheless, in this case, precise control over the anodization parameters is required to obtain a 3D interconnected porous structure, in which the longitudinal pores are connected to other 6-neighboring pores through transversal nanochannels. In particular, the etching times must be precisely adjusted so that selective chemical dissolution at certain positions along the pore channels, corresponding to the HA pulses, is achieved. Simultaneously, excessive etching must be avoided, which will revert to the collapse of the whole porous structure. The higher content of impurities and less density of the HA layers make them less chemically stable against chemical etching compared to MA layers, and hence selective etching of HA layers is accomplished.

In 2009, 3D nanoporous structures (grown in 0.1 M phosphoric acid using cyclic anodization under galvanostatic mode) were fabricated by Losic and co-workers,[223] as shown in Fig. 13a, combining longitudinal nanopores of around 250 nm
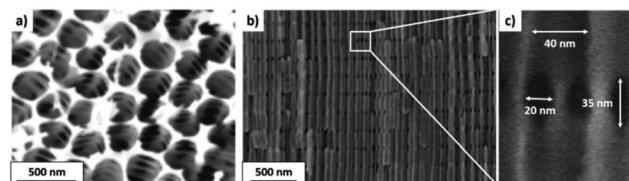


**Fig. 13** 3D network porous structures consisting of a hexagonal array of vertical pores, which are periodically interconnected through transversal nanochannels to adjacent longitudinal pores at certain points. (a) Fabricated by current-controlled cyclic anodization in 0.1 M phosphoric acid. Reprinted with permission from D. Losic and D. Losic Jr, Preparation of porous anodic alumina with periodically perforated pores, *Langmuir*, 2009, 25(10), 5426–5431. Copyright © 2009, the American Chemical Society. (b) and (c) Fabricated by voltage-controlled pulsed anodization. (c) Enlarged view of the area marked in b with a square in which longitudinal pores (diameter = 40 nm) and the transversal pores (diameter = 20−35 nm) can be distinguished. Reprinted with permission from ref. 222. Copyright © 2014, Springer Nature.

in diameter and transversal nanochannels with dimensions of 60–100 nm in diameter, located periodically along the length of the former. Accordingly, the porosity of the alumina membranes was significantly increased. Later in 2014, Martín et al.[222] developed a pulsed anodization controlling-voltage procedure, in which 3D nanoporous networks with longitudinal pore diameters of 45–50 nm and transversal pores of 25–30 nm in diameter were synthesized in 0.3 M sulfuric acid electrolyte (Fig. 13b and c). Following this approach, these structures have been even fabricated in cylindrical aluminium wires,[224] which demonstrates the good reproducibility and consistency of the method.

These 3D porous alumina membranes by themselves have been proven to be useful in many different applications, as will be thoroughly shown in section 7. Also, they have been used as templates for the fabrication of interconnected arrays of nanowires of a wide variety of materials, as will be discussed in detail in the next section.

### 5.4 Pre-patterned structures on the alumina surface

As previously mentioned, pre-patterning of the aluminium surface before the anodization process of the substrate can be carried out by two different methods through a direct approach or an indirect one, resulting in the perfect arrangement of pores. A monodomain porous structure can be relevant for certain applications in photonics[225–229] and magnetic recording media.[230] Moreover, different structures can be produced this way over the surface of alumina, resulting in different and new morphologies in which the geometry of the pore cell is changed, as shown in Fig. 14. The key factor to generate new pore arrangements in a square, triangular, hexagonal or even diamond shape is the initial arrangement of the pre-patterned concave pits over the Al substrate guiding the initiation of pores, but not the shape of the indented pits. In particular, when an FIB pattern with a graphite lattice and a 300 nm interpore distance was used, the oxide walls developed in a triangular shape (see Fig. 14a and b), and if the pattern used had a hexagonal arrangement with some missing sites but the same interpore distance (Fig. 14c) then the shape of the visible oxide walls was diamond (Fig. 14d). A final example of a rectangular arranged pattern of holes with 300 nm for the long and $300\sqrt{3}$ nm for the short interpore distance is shown in Fig. 14e, which also produces a rectangular arrangement of pores after anodization (Fig. 14f). The SEM images corroborate that the final arrangement of the pores is only dependant on the arrangement of the pattern. It is also worth mentioning that more complex arrays based on Moiré patterns, which consist of the superposition of hexagonal patterns with a rotation angle, with several different interpore distances have been reproduced in the surface of alumina *via* nanoimprinting lithographic techniques,[182] as shown in Fig. 14g and h.

The non-hexagonal arrangement can only be maintained for a certain anodization duration before rearrangement of the pores occurs in a hexagonal pattern. The optimization of the anodizing potential accordingly to the self-ordering regimen
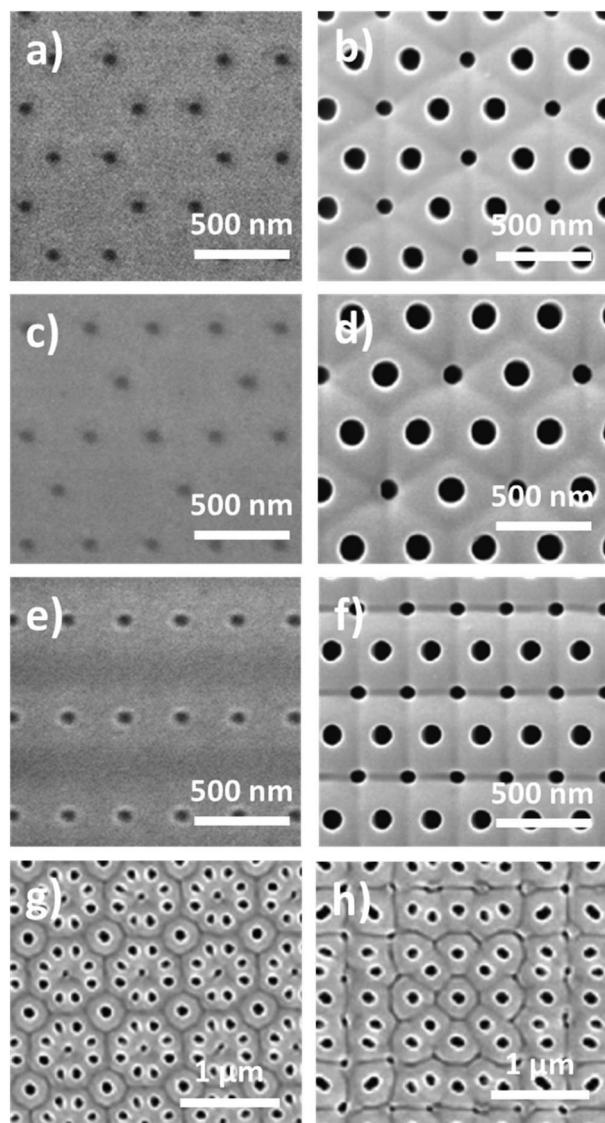


**Fig. 14** FIB patterned concaves with (a) graphite, (c) hexagonal and (e) rectangular lattice structure, where the interpore distance between concaves is 300 nm in all cases. (b) and (d) and (f) corresponding SEM images to the FIB patterns in (a), (c) and (e) after anodization in 0.3 M phosphoric acid at 20 mA with a steady-state potential of 140 V, respectively. Reprinted with permission from ref. 180. Copyright © 2011, the American Chemical Society. (g) and (h) SEM images of the porous surface of alumina with a Morié pattern created from two overlapping square patterns with the same interpore distance (350 nm) and two square patterns with different interpore distances (400 nm and 500 nm), respectively. Nanoindentations were performed with a rotational angle of (g) 36.9° and (h) 0°, and the subsequent anodization was carried out under a constant current of 20 mA at 0° for 2 min, in 0.3 M phosphoric acid. Reprinted with permission from ref. 182. Copyright © 2011, the American Chemical Society.

conditions is also important in the case of a hexagonal unit cell, where the linear relation between the cell size and the optimal value of the anodizing voltage is 2.5 nm V$^{-1}$, in agreement with eqn (2). However, a reduction in the interpore distance in a squared cell has been reported to result in a less

densely packed arrangement compared to a hexagonally packed distribution, according to the following equation:[231]

$$D_{int} = 1.04 \times U + 33, \qquad (10)$$

where $D_{int}$ is the interpore distance and $U$ the applied potential.

In general, the introduction of indentations on the surface of aluminium, which act as nucleation sites, guides the growth and development of the pores, as well as the geometry of the unit cell. However, the nucleation of pores at the edges of the cell boundaries can be propitiated under certain conditions, and thus if the interpore distance between neighboring pores is sufficiently large, the cell boundaries become visible and new pores can be formed at the cell junctions of the imprinted pattern. This phenomenon occurred in the three different examples presented in Fig. 14, where the smaller pores in the SEM images corresponding to Fig. 14b and d, and f do not appear in the FIB pattern that was used in each case, as shown in Fig. 14a, c, and d, respectively. The common factor in these three cases is the interpore distance between the indented pits of 300 nm (long interpore distance in the rectangular pattern, along which the smaller pores arise), which seems to be sufficient distance for the development of these new pores. In this case, the electric field at the bottom of the imprinted concaves defines the size of the pore cell, while the mechanical stress guides the growth direction of the new pores forming at the cell junctions. Accordingly, not only non-hexagonal cells can be generated, but also non-spherical pore shapes are produced depending on the stress field experienced at the cell boundaries. Hence, elongated, elliptical, and triangular smaller pores are generated depending on their surroundings, where the bigger pores grow faster and will confine and restrict the growth of the former pores. More complex patterns can be created with both triangle and diamond shape pores, as shown in Fig. 15c, when an array of non-regular hexagonal polygons (inset in Fig. 15c) is employed. In these nonequilibrium arrangements, the hexagonal cell is partially compressed, leading to the formation of diamond, circular, and triangular pores. This also applies to the smaller pores in alternating size patterns, as shown in Fig. 15a, where two different sized pits of 65 and 45 nm were imprinted at a 200 nm interpore distance over an Al substrate by FIB. After the anodization, the larger pores presented a spherical shape with a diameter of 105 nm, while smaller pores grew with an elongated shape along the direction that was not restricted by the presence of the bigger pores (Fig. 15b). The long axis of the pores was 95 nm and the short axis was 50 nm, where the later the growth in the direction between two bigger pores was cut short due to the much faster growth of the oxide layer of the larger pores, thus resulting in the elongated pore shape. On the other hand, circular pores are favored when the neighboring concave patterns surrounding a particular pit have a symmetrical distribution (distance and size). Also, if the interpore distance of the patterned concave reaches the optimal value to allow the complete development of the pore, the generated
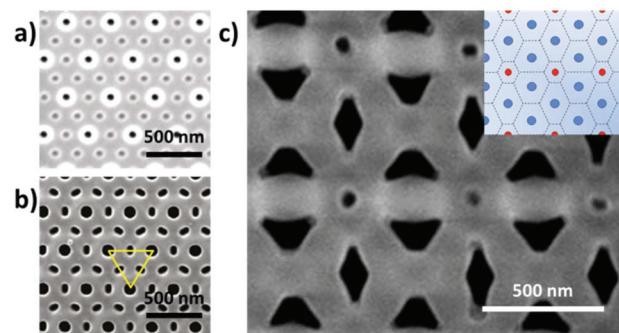


Fig. 15 (a) Alternating FIB pattern with 200 nm interpore distance, where the larger concave size is 65 nm and the smaller concave size is 45 nm. (b) Alternating FIB pattern after anodization in 0.3 M phosphoric acid at 20 mA with a steady-state potential of 140 V. The connecting lines between the bigger circular pores show that the direction together with the growth of the smaller pores in the middle of the two is restricted. Reprinted with permission from ref. 180. Copyright © 2011, the American Chemical Society. (c) SEM image of hybrid triangle-diamond patterned porous template (with a 300 nm periodicity), upon 30 min anodization at 120 V in 0.3 M $H_3PO_4$ electrolyte. The top-right inset image shows a schematic representation of the corresponding triangle-diamond pattern tiling scheme, where a large, blue dot represents the sites included in the prepattern process and the smaller red dots indicate the locations at which compensated pores will appear. Dashed lines define the location of the cell wall formation. Reprinted with permission from ref. 192. Copyright © 2009, AIP Publishing.

pores develop a round shape.[232] Moreover, as the interpore distance is further increased, the area between the cell boundaries of neighboring pores becomes too broad and new non-pre-patterned pores can form,[232,233] as mentioned before. The self-formation mechanism of these pores was first studied by Masuda[195] using a hexagonal pattern with a missing hole; however, after the anodization process, complete repair of the hexagonal arrangement with no missing pores was accomplished, which was described as a self-compensating healing process. The growth and complete development of these pores was also explained according to the equi-field strength model[151] by several authors.[180,232] A direct consequence of this self-compensating mechanism and development of new pores between far apart pores is the reduction of the interpore distance, and thus the size of the unit cell in the hexagonal arrangement, which can be used to overcome the resolution limit of technology commonly employing lithographic techniques and etching treatments to produce stamps and molds in the case of using indirect indentation methods, as proposed in ref. 232, 234 and 235. Another advantage is the possibility to reduce the optimum interpore distance value associated with the self-ordering conditions defined by eqn (2) for each of the different electrolytes, as reported by Choi et al. in 2003. In a 0.3 M phosphoric electrolytic solution at an applied potential of 195 V, the ordering of the pores occurred at an interpore distance of 500 nm; however, the authors were able to reduce this distance to $0.6D_{int} = 300$ nm, while the ordering of the pores was not affected. Recently, nanosphere lithography has emerged as a promising technique to solve the resolution
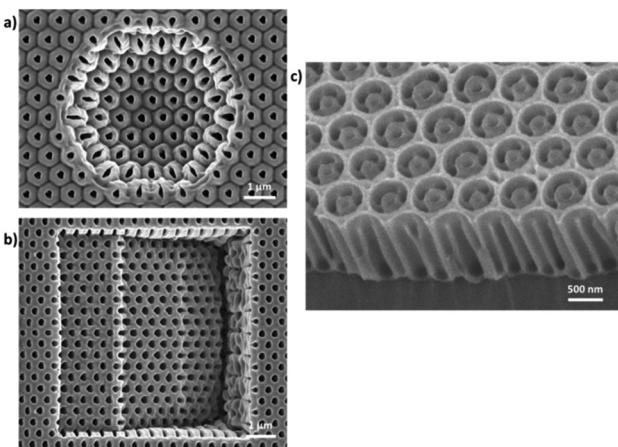
**Fig. 16** (a) and (b) SEM images of anodized nanopore arrays across (a) hemispheric-shaped aluminium surface and (b) stair-case shaped surface. The interpore distance between the nanopores is 350 nm and 200 nm, respectively. Reprinted with permission from ref. 181. Copyright © 2011 Elsevier Ltd. (c) SEM image of a hierarchical AAO structure by NSL technique. The period of the pre-patterned aluminium substrate is 680 nm. Reprinted with permission from ref. 198. Copyright © 2012 WILEY-VCH Verlag GmbH & Co. KGaA, Weinheim.

problem of conventional lithography by selecting the appropriate size of the spheres. Molding patterns using spheres in the range of 13–500 nm in diameter and different interpore distances have been successfully achieved through this method.[198,236,237] In a particular case, hierarchical nanoporous structures, such as that shown in Fig. 16c with a multi-periodic porous structure, were prepared by the NSL (nanosphere lithography) method.

Another recent development addresses FIB patterning over uneven surfaces,[181] as shown in Fig. 16a and b The order of the nanopore array is well maintained all along the uneven surfaces; however, there is some pore shape deformation at the edges due to the absence of a flat surface.

# 6 Nanoporous alumina structures as templates: examples and applications

The internal porous structure of alumina can be filled using different deposition techniques such as ED, CVD, and ALD with different types of materials, resulting in an anti-replica of the pores. As described in section 5, alumina membranes can be fabricated with different porous structures, varying from straight or modulated longitudinal pores to more complex branched pore structures or a 3D interconnected porous structure, and thus different morphologies can be obtained through nanostructuring of materials using alumina membranes as templates. Mainly, straight nanowires, longitudinal nanowires of varying pore diameters, branched nanowires and 3D nano-networks of interconnected nanowires can be fabricated. Some works reviewing this topic can be found in ref. 238–240.

The use of nanoporous alumina structures as templates to grow different materials inside them presents several advantages over other types of templates, such as the diameter sizes that can be achieved in the range of nanometers, combined with straight pore lengths in the range of microns, the low cost and large area of ordered nano-cylinder arrays that can be provided, and thermal stability in a wide temperature range, without loss of the porous structure even after treatments over 1000 °C.[241,242] Depending on the template-assisted growth mechanism used for the material, the original porous alumina can be used with the barrier layer and backing aluminium (for instance, for polymer infiltration and atomic layer deposition) or both backing materials can be removed and the self-sustained nano-hole structure can be used as a template (for electrochemical deposition). Finally, the alumina templates can be dissolved in alkaline or acidic solutions after their filling, leaving the nanostructures free for certain applications.

## 6.1 Template-assisted fabrication of inorganic structures

Through the template-assisted deposition of inorganic materials using porous alumina membranes, three main structures can be obtained, namely nanowires (NWs), hollow nanotubes (NTs), and holey films (or nanomeshes). The most commonly used growth techniques range from chemical approaches such as electrodeposition (ED) to physical deposition processes such as CVD, ADL, and sputtering. Fig. 17
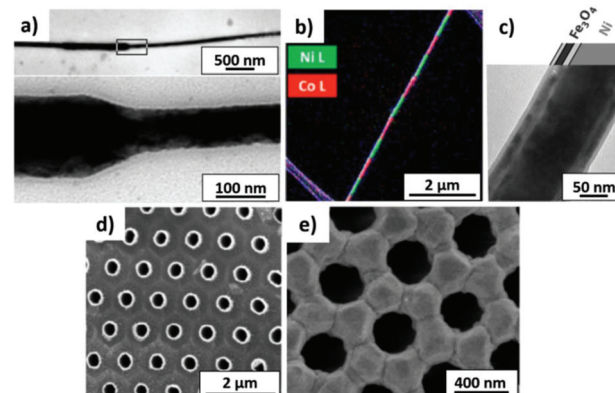


**Fig. 17** (a) Transmission electron (TEM) micrographs of a single modulated Ni wire isolated from the alumina template. Top, low magnification image showing two diameter changes. The area defined by the rectangle is further magnified in the lower panel. Reprinted with permission from ref. 258. Copyright © 2011, AIP Publishing. (b) EFTEM (energy-filtered transmission electron microscopy) image of a multisegmented Co/Ni nanowire. Reprinted with permission from ref. 38. Copyright © 2016, the American Chemical Society. (c) TEM image of an $Fe_3O_4$ (outer)/Ni (inner) core-shell nanowire. Reprinted with permission from ref. 259. Copyright © 2010 WILEY–VCH Verlag GmbH & Co. KGaA, Weinheim. (d) SEM top view image of an array of hollowed carbon nanotubes (CNTs) grown inside the porous structure of an alumina template through a CVD deposition process. Reprinted with permission from ref. 46. Copyright © 2017, the American Chemical Society. (e) SEM image of sputtered $Si_{0.8}Ge_{0.2}$ nano-mesh film grown over an alumina template, where the porous structure was successfully replicated. Reprinted with permission from ref. 66. Copyright © 2016, Springer Nature.

shows a compilation of some of the morphologies that will be reviewed in this section, which are obtained through nanostructuration of a chosen material using alumina membranes as templates by different deposition techniques (ED, CVD, ADL, sputtering, *etc.*) for their application in different fields (a. modulation of pore diameter, b. multilayered nanowire, c. core-shell-type nanowire, d. hollowed nanotube and e. nanomeshes).

**6.1.1   Nanowires.** There are many fields in which obtaining low-dimensional structures, such as nanowires, presents certain advantages. At the nanoscale, different phenomena related to the low dimensionality of these structures can be observed. The most relevant are the changes in the configuration of electronic states due to quantum confinement, which can result in more exotic electronic effects such as localization and splitting of the electronic bands. Consequently, this can result in semimetal-semiconductor transitions[243] or ballistic transport in 1D metallic nanowires,[244,245] among other phenomena. Also, due to the low dimensionality, there is a higher surface to volume ratio, which results in a significant presence of surface conduction or surface effects, characteristic of nanowires. For instance, in these types of structures, when studying the conduction of the surface in bismuth telluride nanowires, topological insulator behavior was observed.[246] Therefore, the use of nanoporous alumina as a template provides a quite powerful platform to study changes on the magnetic and electric properties, as well as in a wide variety of other fields, occurring when reducing the dimensions down to the nanometer scale. The main advantages are the high density of nanowires that can be fabricated at the same time, the high control over the morphology of the resulting nanowires (diameter, length, and density of the nanowires), and the mechanical resistance and stability of the alumina templates.

This method has been extensively used for the fabrication of magnetic nanowires as a way to increase the density storage and performance of already existing magnetic recording devices such as RAMs and hard drive disks due to their high-aspect-ratio or for the development of some new racetrack memories[247] and design of future magnetic logic devices[248–251] through tunning of the magnetic anisotropy governing the magnetic behavior behind the nanowires. As their dimension is reduced along at least one space direction (diameter or length of the nanowires), shape anisotropy becomes dominant over the other the magnetic forces contributing to the total magnetic anisotropy energy. Moreover, due to space confinement, control over the magnetization and demagnetization process, as a consequence of controlling the domain wall motion along the nanowires, can be achieved.[252,253] Different types of domain walls have been reported, separating different magnetic domains (in which spins are aligned in the same direction), depending on the diameter of the nanowires. In general, for diameters below 40 nm, the formation of a transverse domain wall (TDW) is favored, which is a high energetic configuration in which spins rotate transversely to the nanowire length and is favored due to strict space limitations. In contrast, a vortex domain wall (VDW) configuration is found in nanowires with diameters bigger than 40 nm, where changes in the magnetization undergo a less energetic curling process of the spins from one direction to the opposite one, moving along the nanowire length.[252,254–256] These numbers can change depending on the magnetic material.[252] The racetrack memories first proposed by IBM were designed to exploit the control over domain wall motion in nanowires by the injection of an electric current.[257] More sophisticated and recent studies specifically combine both types of domain wall configurations to gain more precise control over the magnetic response by the generation of well-defined pinning sites in the development of more complex logic devices, where the control over the position and motion of domain walls is the key factor. This can be achieved through modulation of the pore diameter along the length of the fabricated nanowires[37,39,249,251,258] (see Fig. 17a).

Also, tuning of the magnetocrystalline energy adds an even higher degree of control over the magnetic properties and domain wall motion by tailoring the chemical composition of magnetic nanowires[36,260,261] and multilayered[36–38,262,263] or even core-shell nanowires[259,264] through alloying (as shown in Fig. 17b and c, respectively).

A rather interesting phenomenon, giant magnetoresistance (GMR), has also been experimentally observed in multilayered nanowires due to the spin transfer process between adjoining layers of hard and soft magnetization, which occurs through an exchange coupling mechanism.[265,266] GMR is displayed in multilayered systems where two possible spin-channels exist, which is associated with a maximum resistance state (antiferromagnetic coupling between subsequent layers) or a minimum resistance (ferromagnetic coupling). Switching between the antiparallel (high resistance) and parallel (low resistance) states is propelled by an external magnetic field. This effect can be directly employed in the fabrication of spin-valve sensors and magnetoresistive random-access memories (MRAM).

It is also worth mentioning the use of these magnetic nanowires, in particular core-shell structured nanowires, in biomedical applications[267] for cell separation[268,269] and tracking,[270] as drug delivery vehicles driven by a magnetic field and hyperthermia treatment.[271]

Another important application of nanoporous alumina membranes as templates for the fabrication of nanowires is in the field of thermoelectric materials (such as bismuth telluride[272,273]), which convert waste heat in the form of a temperature gradient into usable electricity. In 1993, Dresselhaus[274] first predicted the enhancement of the thermoelectric performance of these materials when reducing their dimensions, for instance, in the form of 1D nanowires. The efficiency of a thermoelectric material is defined by the dimensionless figure of merit, $zT = S^2\sigma/\kappa$, where $S$ is the Seebeck coefficient, which measures the generated voltage due to an induced temperature gradient across the material ($\Delta V/\Delta T$), while $\sigma$ and $\kappa$ are the electrical and thermal conductivity, respectively. These three parameters are deeply intertwined, and thus if $S$ increases, $\sigma$ decreases, and increasing $\sigma$ increases $\kappa$ (as a result of the increase in the electron contribution to the

total thermal conductivity), and thus effective enhancement of $zT$ cannot be achieved this way. Nanowire engineering aims to decouple these parameters to obtain phonon-glass electron-crystal behavior, as theoretically proposed by Dresselhaus in 1D quantum wire structures.[274,275] In this case, the electron conductivity is enhanced along the length of the wire through free electron motion in this direction (transition from semimetal to semi-conductor behavior[243]) and phonon scattering is increased in the direction perpendicular to that due to the presence of the surface of the nanowires, which reduces the thermal conductivity.[276] This can be achieved since normally both electrons and phonons suffer collision events or scattering processes at significantly different characteristic distances. Specifically, in most materials, the mean free path of phonons (in the range of hundred nanometers) is higher than that of electrons (usually in the order of tens of nanometers), and therefore the scattering of phonons with the surface of the nanowires increases their scattering without affecting the electrons. Furthermore, the Seebeck coefficient can be further improved due to the increase in the density of states at the Fermi level as a result of the reduction of the dimensionality. Nevertheless, the diameters required to experimentally observe an enhancement in $S$ are too small for most of the interesting materials and is below the lower limit that can be achieved through AAO-based technology (*i.e.*, to fulfil this requirement, bismuth telluride nanowires with diameters of 1 nm are needed). Still, it is possible to use nanowire structures of thermoelectric materials employing alumina membranes as templates to improve their thermoelectric figure of merit, $zT$, through an increase in $\sigma$ or a reduction inf $\kappa$. In particular, the latter approach has yielded more successful results to date. Other effects, besides the increase of phonon boundary scattering commented before, such as topological insulator effects associated with the appearance of surface electron states, among others, have been experimentally found in low-dimensional structures such as nanowires fabricated inside alumina templates.[27,28,246,277] These effects have provided some of the latest breakthroughs in the field of thermoelectricity, both from experimental and theoretical points of view.

A different synthetic route has also been reported for the fabrication of nanowires using AAO membranes as templates. In the case of SiC core-shell nanowires, it has been discovered that if plasma deposition is performed, the deposited material, does not grow along with the pores, and hence, filling of the pores does not occur. Instead, a different growth mechanism is involved. Since the porous surface of the alumina membrane has some texture with crests and valleys, corresponding to the triple union point of the walls of adjacent pores and the actual nano-pores, respectively, nucleation of the SiC nanowires is promoted at the crest points. At these sites, plasma-induced reduction of the aluminium oxide to metallic Al occurs and Al droplets are formed, where later Si and C atoms will be incorporated by the plasma process through Si/C co-precipitation. Subsequently, nanowire growth occurs, thus resulting in the formation of core-shell nanowires made of an SiC core and an AlSiC outer shell.[29]

Another approach is the use of alumina membranes as templates to produce long-range nanostructured surfaces with antireflective qualities, which are especially important for solar cell applications, to reduce the reflected light at the film-air interface as light travels from one medium (air) to another (material film) with significantly different refractive indexes. They are normally used as a mask during the plasma etching process or in nanoimprint lithography to produced periodic Si nanopillar arrays.[30,278–280]

**6.1.2 Nanotubes.** Besides fully compact nanowires, the fabrication of hollowed nanotubes of different types of materials has also been reported. These nanotubes have been applied in drug delivery,[42,281,282] sensing,[43,283] optoelectronics,[44] and energy storage applications (where metal-insulator-metal systems were synthesized *via* successive CVD or ADL layer deposition, such as the fabrication of CNT-SiNT-CNT arrays with high charge capacity acting as the anode for lithium-ion batteries,[40] or titanium nitride[284] and Al-zinc oxide[285] nanotube array nanocapacitors). Additionally, a complete review of the properties and applications of magnetic nanotubes can be found in ref. 41.

**6.1.3 Nanocones.** Conical nanopores can be produced in aluminium substrates by alternating the aluminium anodization and pore widening treatments, as described in ref. 286. These substrates present a hexagonal order of the cones and can be used for the fabrication of nanocones of different materials by sputtering on the surface, electroless deposition, *etc*. For instance, sputtered copper in this type of template was presented as a way to obtain nano-conical electrodes, which increased the working surface area of copper electrodes for electrocatalytic applications.[287] These nano-conical templates have also been used to develop nanoconical perovskite solar cells[288] or plasmonic metasurfaces, which are formed by gold nanocones fabricated by electrodeposition.[49]

**6.1.4 Nanomeshes.** Another strategy, besides the deposition or infiltration of materials inside the pores of the alumina template, involves in the replication of the top surface of the membrane to produce antidots arrays, that is, a thin film layer with a characteristic void structure of hexagonally ordered holes, also known as nanomeshes. Magnetic anti-dot arrays have been developed, typically taking advantage of the occurrence of pinning of the domain walls at the edges of the holes, which hinders domain wall motion. Accordingly, complete magnetization in the direction of the applied field (magnetic saturation) occurs at higher magnetic fields compared to the case of continuous films.[63,64,289–291] Further control over the magnetic behavior was achieved by the engineering of the diameter of the holes and the edge-to-edge distance between holes by tailoring the alumina template ($w$).[292–294] Moreover, the inversion of the magnetization easy axis from the in-plane direction (along the film) to the out of plane direction above a certain hole diameter has been reported (with an improvement in the magnetic performance in the perpendicular direction). This is due to the perpendicular magnetization contribution coming from the edges of the holes since some deposition occurs in the first tens of nanometers along the pore walls.

This approach may be applied to high-density storage data systems and spintronic logic devices. Also, they can act similarly as photonic crystals do for photons, exhibiting a periodic potential for magnons and where the spin-wave dispersion can be tuned for the fabrication of spin filters and spin waveguides.[295] Some magnetic behavior arises from common non-magnetic bulk materials when reducing the dimensionality of the system, such in the case of 2D antidot films. The observation of pore edge ferromagnetism has been reported in oxidized black phosphorous nanomeshes.[65] This effect also appears in graphene nanomeshes and will be expanded in section 6.3.2. Here, it is sufficient to say that it can be used for the development of spin current-controlled devices.

Al nanomeshes have been proposed as transparent conductive Al electrodes for third-generation optoelectronic devices of LEDs, photovoltaics, touchscreens, etc., where besides fulfilling the actual requirements of low resistance and high light transmission, low-cost production, and increase in their flexibility are desirable. Through an easy and cheap anodization process of a sputtered aluminium layer over a glass slide used as a substrate, followed by a controlled chemical etching step, the alumina membranes are removed, leaving only the non-oxidized sputtered aluminium with a patterned structure. Consequently, Al nanomeshes were obtained with increased optical transparency above 70% due to the presence of nanoholes.[296]

In the field of thermoelectricity mentioned above, several studies have been carried out on the thermal transport mechanisms behind this type of perforated film.[66,67] A significant thermal reduction was observed as the distance between holes (w) was reduced due to enhanced phonon-surface scattering events, and in-plane confinement was promoted by the presence of holes.[297,298] In these systems, the electrical conductivity was slightly degraded; however, the overall thermoelectric performance of the nanomeshes was improved in comparison with that of continuous films. If further optimization of the electrical conductivity is achieved, these holey films can easily compete with nanowire technology due to the higher mechanical strength of the former, which makes its integration into TE modules much easier.

**6.1.5 Interconnected networks of inorganic materials.** In the case of 3D-AAOs, since the first development of these structures in 2009 by Losic et al.[223] in phosphoric acid and later in 2014 by Martin et al.,[222] who used sulfuric acid instead, and thus reducing the dimensions of the resulting longitudinal and transversal pores (45–50 and 25–30 nm, respectively), in comparison with the former work of Losic of higher pore diameter (longitudinal pores of 250 nm and transversal pores of 60–100 nm), as discussed in section 5.3, they have been used for the fabrication of interconnected nano-networks of different materials. 3D nanowire nano-networks cause the surface to volume ratio of the nanostructured material to dramatically increase, exceeding the increase in the surface to volume ratio that 1D nanowires (of the same diameter) can provide. The main advantage of these structures is that they allow high tunability of certain materials in the nanometric

scale, while they still can be obtained and handled similar to bulk materials in the macroscopic scale, considering that the resulting 3D nanowire network is self-sustainable after the removal of the alumina template. The 3D structure provides mechanical support, avoiding collapse, as in the case of regular 1D nanowires without the template, as it can be seen from Fig. 18a. Although to date they are still less exploited than their nanowire counterparts, they can cover a vast area of applications in a wide variety of fields, mostly due to their much easier handling, higher mechanical stability, and more straightforward implementation in future devices compared to non-interconnected 1D nanowires.

Some recent examples have been developed in the case of metal nanostructuring since they can be applied in the electrolytic production of hydrogen, where their high surface area and high porosity are optimal for this application,[57] as shown in Fig. 18a. This advantage should be also relevant for applications in battery electrodes, and therefore $V_2O_5$ has been grown through a template-assisted deposition process in these types of 3D AAOs. Nevertheless, in this case, the obtained results showed that the performance was not improved, but diminished due to the negative effect of the interconnections on the final capacity and the poor electronic conductivity of the material.[58] Another interesting possibility when using these 3D AAOs as templates is filling them with magnetic materials, such as Ni[26,59] and Co.[59] By tailoring the nanostructure, the magnetic anisotropy of the whole system can be modified, obtaining properties that are different from both magnetic nanowires and magnetic thin films.[59]

Also, in the case of thermoelectric applications, 3D nanowire networks fabricated via template-assisted deposition provide a great advantage over thermoelectric nanowires,
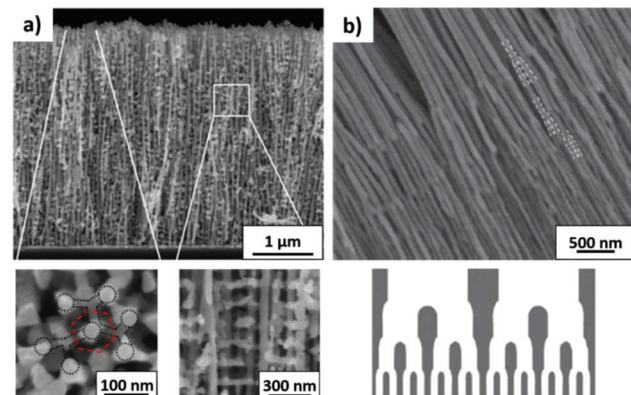


Fig. 18 (a) SEM cross-sectional image of a 3D Ni nanowire network after removal of the alumina template, underneath the top view (left) and cross-section (right) of the nano-network structure at high magnification. The dashed red lines represent the unit cell of the alumina template of hexagonal pores arrangement. Reprinted with permission from ref. 57. Copyright © 2018, the American Chemical Society. (b) SEM image of Ni nanowires with three-generation Y-branched morphology. Bottom: schematic drawing of such multi-branched nanowires. Reprinted with permission from ref. 53. Copyright © 2010 WILEY-VCH Verlag GmbH & Co. KGaA, Weinheim.

which is the possibility of having the improved properties that the nanostructuring provides together with a mechanically stable structure at the macroscale, which can be easily handled. For instance, thermoelectric materials such as bismuth telluride have been already synthesized in this form[60] and the main advantage of nanostructuration, that is, the reduction in i thermal conductivity, is maintained.[299]

Branched nanowires (Nws), branched nanotubes (NTs) and a segmented hybrid combination of Nws-NTs with a branched structure can also be considered as another type of 3D nano-architectures,[50,300] where, again, the enhancement of the available surface area is of great relevance for applications such as energy storage and solar cells due to the improved light absorption in these structures, as shown in ref. 301. Moreover, the electronic transport properties of Y-branched nanowires have also been an object of study of different materials, ranging from CNT[51,302] (see section 6.3.1) to solid Bi[52] branched nanowires. The magnetic behavior of a single Y-junction of Ni nanowires was investigated by Guo *et al.*[303] Also, more complex multi-branched structures made of different materials (Si-NT/Nw, Au, Ni, Ge-NT/Nw, and Pt), as shown in Fig. 18b, have been synthesized with potential applications in nanoelectronics,[53] in particular, for the development of improved transistors, as in the case of Y-branched nanotubes/nanowires based on Ge,[54] nanomagnetism[53] and for catalytic applications.[55]

## 6.2 Template-assisted fabrication of organic nanostructures

**6.2.1 Organic nanotube arrays.** An example of these types of structures is carbon nanotubes, where interesting electric conduction effects have been theoretically predicted and experimentally observed to some extent, ranging from ballistic transport (corresponding to a metallic behavior)[304–306] to Coulomb blockade due to the localization of the energy states into discrete energy levels (associated to semiconductor behavior), inhibiting the flow of electrons and promoting individual electron transport by the tunnel transfer of electrons when one of the discrete energy levels falls into the Fermi energy level of the system.[307–309] CNTs can have either semiconducting or metallic electronic properties depending on their diameter since their bandgap energies vary inversely as a function of this parameter.[310–313] Thus, they have been studied as good candidates for the fabrication of field-effect transistors[314–316] and single-electron transistors.[309,317,318] Several works have used alumina temples for the growth of CNTs inside the porous structure *via* chemical vapor deposition technique (CVD),[45,319–322] as shown in Fig. 18d, to reduce the cost of the synthesis of CNTs and overcome the difficulty of handling individual nanowires when grown by other methods such as molecular beam epitaxy (MBE). Following this approach, nano-capacitors based on CNT arrays through template-assisted deposition have been developed, showing relatively good capacitance values with room for improvement.[323] However, other studies suggest that the electrical conductance of carbon nanotubes grown on AAO templates, and thus the performance of FETs based on them, diminishes due to the implied

accumulation of defects during their growth.[324,325] Y-branched carbon nanotubes have also been studied as possible candidates for the development of FETs.[51,302]

Recently, these structures have demonstrated their applicability for transport[46] and sensing[326] of certain molecules, and CNTs with modulated diameters along their length can be implemented for the filtration and separation of molecules, cells, or proteins.[327]

**6.2.2 Organic nanomeshes.** Graphene nanomeshes (GNM) have been implemented in the fabrication of field-effect transistors (FETs) with improved performances than their graphene nanoribbon or nanotube counterparts,[68,328,329] where reducing the distance between the nano-holes ($w$) translates into an increase the ON/OFF current ratio of the resulting device. Optimization of the AAO template-assisted fabrication process of GNMs has allowed low-containing defect graphene nanomeshes with hexagonal shaped nanoholes (instead of rounded holes) to be obtained, where ferromagnetic behavior coming from the polarization of spins at the edges of the hexagonal pores was observed. Moreover, at a critical $w$ value and under a critical external magnetic field, the accumulation of polarized spins is favored at the pore edges, followed by the spin pumping effect since the excess spins are abruptly emitted. This effect can be used in the fabrication of future spintronic working devices, where the manipulation of spin currents is a key factor for the complete development of this technology[330]

**6.2.3 Polymer nanostructuring.** The fabrication of polymers using nanoporous alumina as templates opens the possibility of obtaining one-dimensional polymeric nanostructures with novel properties, which can be used in nanoscale devices, such as biosensors and optics. A wide variety of polymer structures, such as nanotubes, nanocapsules, nanofibers, and nanospheres can be fabricated *via* the infiltration of polymer melts or solutions into the AAO templates or by polymerization of monomers inside the nanopores. Besides obtaining functional nanostructures, these fabrication techniques allow the possibility of studying different physical properties of polymers when they are confined to low dimensions, such as their crystallization, dynamics, mechanical and thermal properties. A complete review of these types of structures can be found in ref. 331. Even electrochemical polymerization can be used to grow certain conductive polymers inside alumina templates, which was performed with PEDOT inside 3D AAOs to obtain a 3D interconnected free-standing network of 20 nm diameter vertical nanowires connected by 10 nm diameter wires, maintaining the semiconducting properties of the polymer.[62] These 3D structures have also been filled with polyethylene by melting infiltration, obtaining hydrophilic, flexible nanostructured macroscopic polymeric structures with tunable iridescent coloring (considering that they act as Bragg refractors, being the replica of the 3D alumina templates, the color of which can be tuned by changing their fabrication parameters, as was discussed in section 7.1).[61] Finally, both modulated and 3D AAOs have shown potential for obtaining different polymers, replicating their nanostructure.[220]

Some of the most notable applications of nanostructured polymers are in the development of future biosensing, electronic, and optoelectronic devices. For example, improved luminescence and lasing properties were reported due to the preferred orientation of the β-phase polymer chains along the nanowire axis in PFO nanowires and nanotubes.[32,332] Later, the same researchers demonstrated the possibility of controlling the polarization direction of PFO light emission in the form of Y-branched nanowires by adjusting the angle between branches.[333] Several studies on the electrical transport properties of polymeric PEDOT nanowires,[31,47] and PH3T nanotubes[48,334] showed improved carrier mobility and electrical conductivity, respectively, which are qualities required for the fabrication of organic field-effect transistors and solar cells. 3D polymeric membranes, as mentioned above, with a Bragg reflector photonic response, are good candidates for chemical and biosensing applications. Further functionalization of the surface of polymeric nanowires can enhance their selectivity and sensibility for the detection of specific molecules, or make them responsive to certain stimuli (such as pH, humidity, and light).[56]

# 7 Properties of nanoporous anodic alumina structures and their applications

Nanoporous alumina is widely used in different fields. Obtaining a self-ordered highly porous structure is important, for instance for increasing the adsorption and the fabrication of membranes. Moreover, the great control over the diameter of the pores, together with the long-range self-ordering can be used to generate structural coloring by different means, and the high surface to volume ratio of these porous structures can be also used for biosensors once the pore walls have been activated with certain substances. Next, we will review some of these applications.

## 7.1 Structural coloration

The sole presence of a patterned nanostructure with a certain order produces a bright structural coloration on metallic surfaces, which is angle sensitive. This coloration is produced by the interference of light with the ordered patterned structure, as shown in ref. 8. Ordered dimple arrays with a diameter of 500–550 nm were produced on an aluminium substrate during anodization in phosphoacetic acid. After the chemical dissolution of the oxide layer, structural coloration was observed in the visible range of 500–700 nm, coming from the reflected light on the periodically ordered dimple array over the aluminium surface.

The structural coloration of nanoporous alumina membranes is mostly based on the Fabry–Perot interference occurring at the Al metal/AAO film and air/AAO film interfaces (see section 7.2 for a more detailed description of this effect); however, there is a threshold thickness of around 2 μm, above

which, this interference is not observed[342] since all the incident light will be absorbed by the porous membrane. Regardless of the film thickness limitation, the way light interferes at the different interfaces can still be modulated to produce coloration with a high degree of tunability by two means, namely controlling the depth of the pore channels (or a total thickness of the oxide layer within the limiting range)[343,344] and by tuning the porosity (changing the pore diameter or interpore distance while one of the two is fixed)[341,345] since both structural features produce changes in the effective refractive index of the anodic aluminium layer. Using all these different parameters, virtually any structural color can be produced with these structures according to Bragg's law.

$$\sum_i 2n_i \times d_i \times \cos\theta_i = m \times \lambda \tag{11}$$

This establishes a clear relationship between the effective refractive index and the reflection of light, and hence the colours that are perceived, where $n_i$ is the effective refractive index, $d_i$ is the thickness, $\theta_i$ is the reflection angle, $m$ is the order number and $\lambda$ is the reflective peak wavelength that gives the observed colour. The suffix $i$ stands for the different dielectric layers with different refractive indexes of which the alumina membrane can be composed (see section 5). It is also worth mentioning that the latter two parameters, and thus the structural coloration, are angle-dependent on the incident light.

Moreover, the deposition of a metallic layer over the nanoporous AAO can further improve the colorimetric response of these membranes, adding a higher variety of colors, as well as enhancing the reflectance of the light on the metalized surface. In 2018, Manzano *et al.*[341] studied the dependence of the different structural parameters of AAO films (interpore distance, pore diameter, porosity, the thickness of the oxide layer, and chemical composition as a function of the anodizing electrolyte) against coloration and the effective reflective index of the films. According to their experimental observations, the authors concluded that the thickness and porosity of the AAO films are the only two morphological parameters that influence the effective refractive index of the films, thus affecting their color. Fig. 19a clearly shows the inverse relationship between the values of the effective refractive index and the thickness of the alumina membrane. The porosity of the films also affects both the refractive index and coloration, as is seen when comparing samples grown in oxalic acid and that anodized in sulfuric acid and ethylene glycol mixed electrolyte solution, which showed a similar porosity of 13.2% and 13.6%, respectively. Thus, alumina films with the same porosity, also having the same thickness, show nearly the same coloration. However, when the porosity was significantly reduced to 11.5% (samples anodized in sulfuric acid, red line), a different coloration was obtained when fixing the thickness. For example, an AAO film with a thickness of around 800 nm showed a vibrant green coloration in sulfuric acid-containing ethylene glycol solution (green line) compared to the light
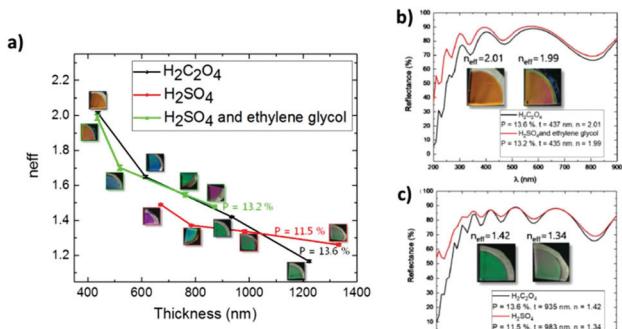
**Fig. 19** (a) Effective refractive index as a function of the thickness for different percentages of porosity (achieved by varying the anodization conditions and electrolyte solution) and the corresponding optical images of the fabricated Cr−AAO−Al films. (b) and (c) UV-Vis reflectance spectra of AAO−Al films anodized in different electrolytes while the thickness and porosity were kept constant. Inset shows optical images of the films. Reprinted with permission from ref. 341. Copyright © 2018, the American Chemical Society.

blue color of the alumina film of the same thickness when it was anodized in sulfuric acid. To further prove this dependence, other morphological parameters were varied such as pore diameter and interpore distance, while the thickness and porosity of the alumina films were fixed. Accordingly, two different sets of samples were grown (Fig. 19b and c) with the same coloration. A golden hue was achieved when the thickness and porosity of the films were fixed at 437–435 nm and 13.6–13.2%, respectively. The corresponding refractive index was around 2, regardless of the other structural parameters such as pore diameter and interpore distance, which were both varied by changing the electrolytic medium, using in each case oxalic acid and sulfuric acid-containing ethylene glycol. Another pair of green-colored AAO films were grown in oxalic (pore diameter 30 nm and interpore distance 100 nm) and sulfuric acid (pore diameter 20–25 nm and interpore distance 62–65 nm) with fixed thicknesses of 935 and 938 nm and porosities of 13.6% and 11.5%, respectively. The effective refractive index of the samples was in the range of 1.4–1.3, giving a final green coloration. In this study, all the samples were metalized with a thin layer of Cr to enhance the colorimetric response of the anodic oxide films. An optimized layer thickness of 8 nm was used considering that the thickness of the evaporated metallic layer must be thin enough to avoid the propagation of light in the metal but not too thin that the absorption of light is not enhanced.

Previous works have investigated this mechanism, where the interaction between light and the porous structure of AAO films was improved by the addition of a metallic layer. In the simplest case of an AAO film, phase modulation of the light in the porous structure generated a wavy profile, where reflective peaks appeared at wavelengths corresponding to the in-phase interference of light (constructive interference), while valleys were formed when the phase difference between the reflected light at the two different interfaces was out of phase (destruc-

tive interference). By adding a thin metal layer, the maximum absorption of light should occur at the wavelengths associated with the destructive interference (valleys) of light in the anodic oxide film, and thus the reflective profile of the valleys is sharpened. In this conjugated twin-phase mechanism, which was proposed by Xue *et al.*,[345] constructive and destructive interference in the metal layer conversely correspond to that of destructive and constructive interference in the AAO film. The thickness of the top metal layer was designed so that asymmetric phase modulation between the two layers is achieved, hence improving color saturation. Further enhancement of the reflective peaks was accomplished by increasing the roughness of the metal layer, which led to an increase in the broad band absorption efficiency of the film.

The authors developed a color printing technique combining the color saturation approach described above together with full-color generation through tuning the thickness and porosity of the AAO layer with lithography in such a way that a pattern could be written over the metal-AAO-Al films and then revealed by simple chemical etching (Fig. 20a). The colors of the pattern could be selected by adjusting the thickness and etching time of the anodic oxide layer (through a change of the porosity and effective thickness between the patterned and unpatterned AAO regions). Furthermore, by carefully choosing colors that appear in a narrow wavelength range, the pattern could be encrypted. In Fig. 20b, encryption of the pattern was
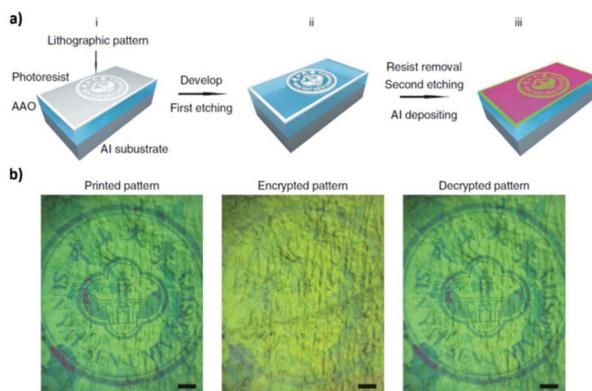


**Fig. 20** (a) Method of colour pattern printing. (i) After spin-coating on an AAO template, the photoresist is patterned using photolithography. (ii) The photoresist is developed to leave the designed patterns, after which the first acid etching is implemented to form the difference of effective thickness of the AAO template (and thus a difference in the effective refractive index) between patterned and unpatterned AAO domains. (iii) An Al layer is sputtered on the sample to form the designed colourful pattern after the removal of the photoresist and the implementation of the second etching. (b) Encryption of the printing pattern by choosing colors with a small wavelength difference. The image on the left, printing pattern in blue color, and green-black ground (printed pattern). Both colors are within close wavelengths numbers. The image in the center, spin coating of PMMA produces a redshift in color and the pattern becomes invisible (encrypted pattern). Blue color shifts towards green. Right image, after removal of the PMMA layer, the pattern becomes clear again (decrypted pattern). Reprinted with permission from ref. 345. Copyright © 2015, Springer Nature.

achieved by first selecting blue and green as contrasting patterned colors with corresponding reflective peaks lying in close wavelength numbers. Then, when coated with poly (methyl methacrylate) the refractive index of the AAO changed, producing a red shift in the whole reflectance spectrum of the sample. After the red shift, both colors were located in the green region, and thus the encrypted pattern became invisible. When the polymeric layer was removed, the patterned code could be read once again. These experiments demonstrated the viability of using structural coloration of AAO for writing and labeling applications, as well as anti-counterfeiting and data encryption storage applications with a small micrometric resolution on large sample areas up to the centimeter scale.

In the case of nanoporous structures with non-homogeneous diameters along the depth of the pores (modulated nanopores,[346,347] or even 3D nano-structures[348]), the oscillatory optical response of these structures is based on the interference of light reflected through a multilayer nanoporous structure of alternating layers of low porosity (MA layers) and high porosity (HA layers) with higher and lower refractive indexes, respectively (see Fig. 21b). High porosity layers correspond to wider pore segments (see Fig. 11d or Fig. 12 in section 5.2) in the case of modulated nanopores. Regarding 3D porous structures, high porosity layers are associated with the transversal nanochannels interconnecting the longitudinal pores (see Fig. 13, section 5.3 and Fig. 21a, section 7.1) with a porosity that can reach up to 80% compared to the longitudinal pores of around 20% porosity (low porosity layer). Thus, the refractive index of each layer is defined by the fraction of alumina filled by air and changes as a function of the corresponding porosity. Fig. 21b illustrates the periodic modulation of the refractive index through the 3D alumina membrane and reflection of the light between adjacent layers.

Considering that the fabrication method allows great control over the thickness of each of these layers, as well as its periodicity, one can fabricate a periodic structure combining different layers, and thus a distributed Bragg reflector is obtained, where propagation of specific wavelengths can be designed to produce the desired coloration of the fabricated membrane. Fig. 21c shows different Brag reflectors specifically designed to have a certain colorimetric response as a function of the thickness of the low porosity layer (MA layer), which can be controlled by the duration of the MA pulses.

This type of physical coloration through nano-engineering of the structural parameters is also presented in nature, ranging from opals to butterfly wings (see, for instance, ref. 61 and 348).

In all the different approaches used to modulate the color of AAO membranes from metal-AAO-Al films to MA/HA multilayered AAO, due to the porous nature of these anodic oxide membranes, the refractive index of the initial metamaterial composed of a porous alumina structure filled by air will be drastically changed by wetting in water (or any other liquid or gas) since the propagation of light changes as a function of the surrounding medium. This change in the effective refractive index results in a shift in the reflection peaks, and hence different colorimetric responses due to environmental changes. This process is reversible, and therefore it can be easily implemented for the fabrication of colorimetric sensors to detect certain substances.[61,349]

Another property of these structures is that their color changes depending on the substrate on which they are placed. A specific example of this property of color sensitivity is provided in Fig. 22. This 3D AAO structure, after removal of the remaining Al substrate, was completely transparent, but when placed on different substrates the same sample exhibited a significant color variation. Light will be first reflected from the substrate located underneath the 3D-AAO membrane and then propagates back through the metamaterial, and thus a change of color is observed depending on the nature of the substrate. Fig. 22 shows a clear change in the perceived color from green to pink when the 3D-AAO membrane was placed on top of a lighter or a darker substrate. In the former, most of the light is reflected and will propagate back, while in the latter case, light is only partly reflected since most of it will be absorbed on the dark background, resulting in the observed change of coloration. These features, both the dependence of the substance filling the pores and the substrate used, can be specifically used for security, anti-counterfeiting, camouflage detection, and food safety applications, as cited by the authors.

### 7.2 Optical and photonic crystals

The fabrication of photonic crystals based on anodic alumina templates is a step forward in the control and modulation of light. Lately, there has been a great development of these structures based on nanoporous anodic alumina, mainly because this method presents several advantages compared others to produce photonic crystals, being cost-competitive, fully scalable, and relatively simple to implement. An extensive review
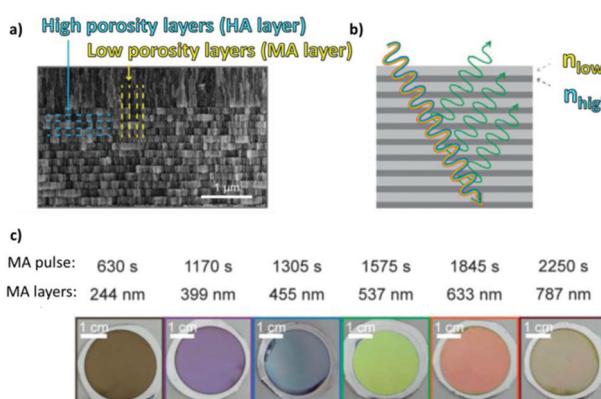


**Fig. 21** (a) Cross-sectional SEM image of AAO membrane, where HA layers are identified in blue and MA layers are marked in yellow. (b) Schematic of the interaction of light at the different layers of higher ($n_{high}$) and lower ($n_{low}$) refractive indices associated with high porosity and low porosity layers, respectively, behaving as a Bragg stack. (c) 3D-AAO Brag reflectors with a pre-designed reflectance by the thickness of MA stack layers. Reprinted with permission from ref. 61. Copyright © 2018 WILEY-VCH Verlag GmbH & Co. KGaA, Weinheim.
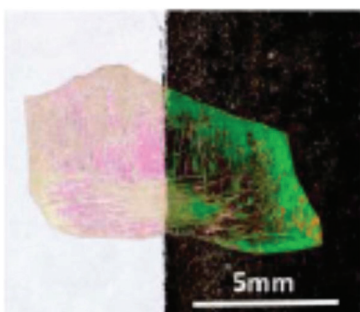
**Fig. 22** Observed color change of the 3D-AAO sample from pink to green when placed on top of different substrates. Reprinted with permission from ref. 348. Copyright © 2018, the American Chemical Society.



**Fig. 23** Structural details of the photonic crystal structures made from nanoporous AAO membranes by structural engineering of the effective medium.

of a wide variety of structures fabricated up to 2017–2018 can be found in ref. 350 and 351

The pioneering work of Masuda and coworkers demonstrated the feasibility of the structural engineering of nanoporous alumina for the fabrication of 2D photonic crystals. By exploding the tunability of the effective medium of these membranes, which can be treated as a composite material consisting of an alumina matrix filled by air, one can control the way light is propagated across the porous AAO structure, as established by the Bragg eqn (11). Masuda *et al.*[352] reported the modulation of the position at which a photonic bandgap appears, where by controlling the interpore distance in the alumina membrane, a red shift was observed as the cell size (interpore distance) increased. Further control over the position of this photonic bandgap could be achieved by the widening of the pores through chemical etching, while the interpore distance was kept constant. In this case, a blue shift of the photonic emission was recorded.

Accordingly, the development of more complex anodization processes to gain control over the in-depth modulation of the porous structure of alumina such as pulsed and cyclic anodization techniques has monopolized most of the attention of researchers. Hence, most of the examples of photonic crystal structures found in the literature are based on branched, modulated, or 3D-nanoporous anodic alumina.

According to what has been stated up to this point, 4 different morphologies with which alumina membranes have been fabricated through nano-engineering of their structural parameters (and thus engineering of the effective medium and generating photonic crystal structures) can be highlighted (see Fig. 23).

**7.2.1 Fabry–Perot interferometers.** The simplest of all these optical structures are Fabry–Perot interferometers with a uniform effective refractive index along their structure, which were briefly described in section 7.1. In these thin AAO films, which can have thicknesses of up to 2 μm to show this effect, fine control over their thickness and porosity are key factors to modulate the effective refractive index.[342] These structures can act as sensing platforms due to the changes in the refractive
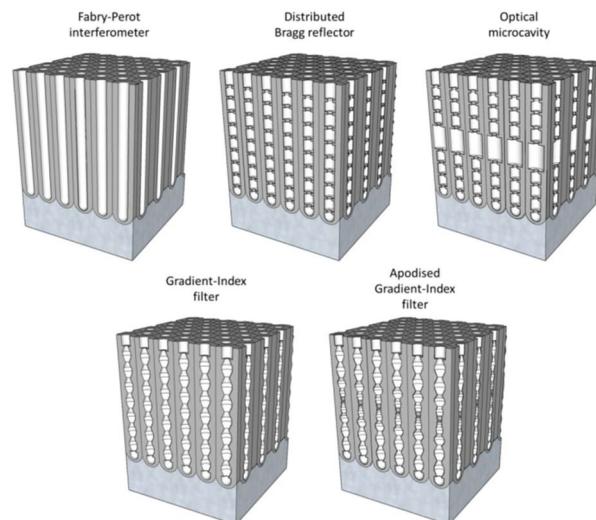
index of the material filling the straight pores (from solids to liquids and gases). Furthermore, if a metal layer is evaporated over the porous membrane, the structural coloration is enhanced, as described in section 7.1, and hence changes of the filling medium can be perceived with the eye by the improved colorimetric sensitivity of metal-AAO/Al films.[341,345]

Recently, their performance as chemical sensing platforms was tested by Ferro *et al.*[14] in a study evaluating the Fabry–Perot interference spectra of AAO films as a function of glucose concentration through photoluminescence measurements, combined with other multivariate analytical data processing techniques. The determination of glucose concentration with good analytical performance was reported employing this approach.

However, these proposals based on straight pore channels were shown to have geometric limiting factors (limiting the range of the structural parameters with which alumina membranes can be fabricated, including interpore distance, pore diameter, porosity, and thickness) and therefore, their versatility is too low for most practical applications.

**7.2.2 Distributed Bragg reflectors.** Distributed Bragg reflectors are fabricated through periodic pulses, resulting in a stack layered structure of high and low porosity (low and high refractive indexes, respectively). Applying the Bragg reflection law (7), by tunning the different refractive index layers, the location of the optical bandgap can be tailored to fulfil certain requirements for specific applications. Pulsed anodization alternating between MA and HA regimens has been intensely used in the fabrication of Bragg stacked reflectors based on MA/HA layered AAO by several authors,[211,216,218,222] where the phonic response was modulated by the length of the MA segment (or duration of the MA pulse), followed by subsequent chemical etching of the HA layer. Fig. 24a shows the typical voltage-controlled pulse anodization profile alternating between MA/HA regi-
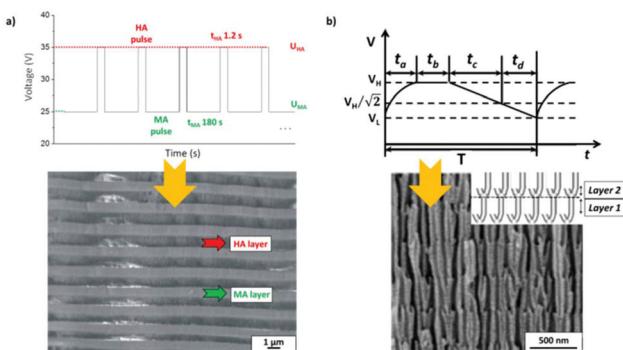
**Fig. 24** (a) Typical voltage signal applied during the pulse anodization of aluminium, where $U_{MA}$ and $U_{HA}$ are the anodizing potentials used to achieve mild anodizing (MA) and hard anodizing (HA) conditions, respectively. Bottom, cross-sectional view of the resulting stacked Bragg-based alumina structure with alternating MA and HA layers formed by pulse anodization in 0.3 M sulfuric acid at 1 °C, after selective etching (in 0.52 M phosphoric acid at 45 °C for 20 min) of the HA layers. Reprinted with permission from ref. 211. Copyright © 2011 Elsevier Ltd. All rights reserved. (b) Applied voltage signal profile during pulse anodization under MA conditions in 0.3 M oxalic acid. Bottom, scheme of the resulting photonic crystal heterostructures composed of two different photonic crystals with different lattice constants (PC1 and PC2). Reprinted with permission from ref. 353. Copyright © 2008 Elsevier B.V.

mens, and the bottom shows the cross-view SEM image of the corresponding MA/HA layered AAO structure fabricated in 0.3 M sulfuric acid, where the HA layer was chemically etched.[211] However, due to the limited control achieved over the structural parameters and morphology of the pores under HA conditions, cyclic and pulse anodization under MA conditions have become the most popular approaches. Under these conditions, more precise tuning of the shape of the pore channels can be attained. It is important to note that as the voltage decreases from a higher starting applied potential, $V_H$, to a lower one, $V_L$, by a factor of $1/\sqrt{n}$ (within MA regimen), an n-branched porous alumina structure is formed, as described in section 5.1. However, as the voltage is periodically restored to $V_H$, only one of the branched channels will continue to grow to undergo a new branching process, while the others will be terminated at this stage (as shown in the SEM image and schematic drawing in Fig. 24b).

The typical voltage signal profile of pulsed anodization in the MA regimen is illustrated in Fig. 24b, where two well-defined segments of different trends can be identified, namely sinusoidal increase in the applied potential to $V_H$ and a linear decreasing segment down to $V_L$, where both segments are periodically repeated during $N$ cycles. The stacked branched porous alumina is characterized by two main layers, where layer 1 is the main stem pore corresponding to the periods between $t_a$ to $t_c$, with a characteristic $d_1$ thickness and $n_1$ refractive index. Also, layer 2 consists of branched smaller pores formed during time $t_d$, with a $d_2$ layer thickness and $n_2$ refractive index. Then, according to the Bragg reflection law (7), varying $d_1/n_1$ or/and $d_2/n_2$ of each respective layer, the locations of the photonic bandgaps can be tunned across the

UV-VIS-NIR spectrum[354] depending on the desired applications. Generally, a red shift (towards higher wavelengths) as $t_c$ is increased has been reported,[353,355] while pore widening produces a blue shift.[349,356,357]

The fabrication of stacked photonic heterostructures, PC1, and PC2, that generate two different (first-order) photonic band gaps has also been reported.[355,358] In particular, overlapped, staggered, and split photonic bandgaps were generated by tuning the location of the first order photonic band of PC2 along the UV-VIS spectrum with an increase in the anodization voltage.[355]

Overlapping of several band gaps can be directly applied to produce a huge prohibited photonic bandgap as a way to reduce reflection losses in dielectric materials. Moreover, the separation between splitting bandgaps can be tuned for filtering applications, with control over permitted passbands and multichannel transmissions.

Photonic crystal heterostructures based on 3D porous alumina networks, where the periodicity of the high and low porosity layer (layers of low and high refractive index, respectively) is systematically altered as the thickness of such layers is gradually reduced, have been proven to enhance the optical sensibility four-fold (translated into a change of color) due to induced resonant interference.[16]

Additionally, the high control that the abovementioned Bragg reflector-AAO structures have demonstrated to provide fine adjustment of the location of the optical bandgaps can be used to make them sensitive to specific changes in the effective media inside the nanopores. A redshift in the photonic stopband of porous alumina photonic crystals has been experimentally observed based on the distributed Bragg reflector structures described above and a decrease in the intensity in the transmission spectra with exposure time and increasing concentration of different substances from liquids (of increasing refractive indexes water, ethyl alcohol, ethylene glycol, and glycerol, for instance)[359] to gases (ethanol, methanol, acetone and toluene.[360,361] Based on this sensitivity towards changes in the effective medium, more sophisticated BR-AAO sensors have been developed for the detection of specific molecules, such as vitamin C[362] or particles, such as mercury ions, $Hg^{2+}$.[17]

**7.2.3 Optical microcavities.** Optical microcavities are a step forward in the fabrication of a cavity section between two Bragg stacked reflectors for the confinement of light. The length of the cavities is adjusted by varying the duration time, $t_b$ (in Fig. 24b) at which high voltage ($V_H$) is sustained over time. Consequently, a central microcavity can be introduced between the Bragg reflectors in the alumina structure by applying a central high voltage pulse of a certain duration.

Accordingly, Wang et al.[363] developed two different types of optical microcavities, type I and type II, as shown in Fig. 25. If both $N$ cycles of pulsed anodization to form the AAO Bragg reflectors are applied in-phase, or if a phase shift is introduced between them without the need for a central microcavity, then constructive or destructive interference is promoted at certain wavelengths, respectively. In type I, the resonance peaks are
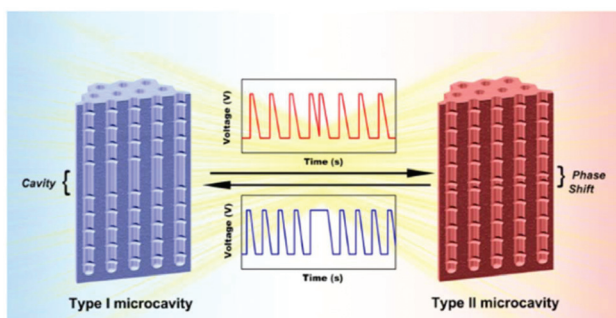
**Fig. 25** Illustration of the fabrication process of AAO microcavities by pulse anodization. Type I microcavities are prepared by inserting a cavity layer between the AAO-DBR structures (left side in blue). Type II microcavities are fabricated by shifting the phase of anodization to achieve the phase modulation of an effective refractive index in the bottom Bragg reflector structure (right side in red). Reprinted with permission from ref. 363. Copyright © 2015, the American Chemical Society.

introduced in the photonic bandgap of in-phase (constructive interference) distributed Bragg reflectors at each side of a central cavity layer with a constant refractive index according to the Bragg condition for constructive interference, $n_H d_H = \lambda/4 = n_L d_L$, where $n_H$, $d_H$ and $n_L$, $d_L$ are the refractive indexes and thicknesses of the grown layers under high and low voltage, respectively. By optimizing the length of the resonant cavity, resonant peaks appeared at positions corresponding to the different order resonant peaks associated with the Bragg reflector structure. To produce type II, a phase shift from $1/2\pi$ to $7/4\pi$ was introduced between the two Bragg reflectors to achieve destructive interference, which translates into a shift in the refractive index of the bottom distributed Bragg reflector (DBR) structure. However, resonant first-order peaks only appeared for a $7/4\pi$ phase shift or higher. At lower phase shifts, significant structural changes were not observed at the interface, in other words, no modulation of the pore geometry occurred. The authors hypothesized that these low phase shifts are associated with an early stage in time as the voltage is reduced from $V_H$ to $V_L$, at which a steady current state has not yet been reached. Thus, modulation of the pore shape does not occur, and therefore there are no changes in the refractive index. This is one of the major drawbacks of this method, as previously mentioned in section 5.1, because as the voltage is reduced during the formation of branched pores, relatively long recovery times are needed until the new steady state is reached, and thus the formation of pores is also delayed. Changes in the pore structure can be observed once the steady state is achieved, that is, after thinning of the barrier layer down to the corresponding value of the low anodization potential, $V_L$.

Both types of microcavities offer great versatility in the way that resonant peaks and stop bands are tuned across the UV-visible and near-infrared spectra. Moreover, the specifically added resonant peaks are narrower and the energy transmission of these peaks is enhanced compared to the actual photonic stop bands of the distributed Bragg reflectors, and thus the performance (higher sensitivity and quality factor, $Q$

ref) of these photonic structures is improved.[16,363,364] Combining the improved photonic response of the aforementioned type II microcavities, together with the intrinsic dependence of Bragg reflectors to the effective medium, the authors developed a humidity sensor.[363]

**7.2.4 Gradient index-filter and apodized gradient index-filter.** In the fabrication of gradient index optical filters (GIF) or apodized gradient-index filters, pulses with a sinusoidal profile and sinusoidal pulses with a varying profile define the geometry of the pores of these structures, respectively. The difference between both methods is the introduction of a mathematical function, where in the latter case, to produce a change in the original sinusoidal profile, which aims to enhance the photonic crystal quality of the structure. Consequently, narrower and more intense photonic stop bands are achieved.[365] However, in both cases, the time of the applied pulse, $T_p$, allows tunning of the location of the permitted and forbidden bands across the UV-VIS to NIR spectra.[16,365–367] Fig. 26a shows the typical applied current profile during this type of pulsed anodization to produce AAO optical bandpass filters and the correlation between the anodization parameters and the pore geometry. Fig. 26b shows the transmission spectrum of an AAO optical filter with a single stopband fixed at 331 nm, which is associated with a pulse
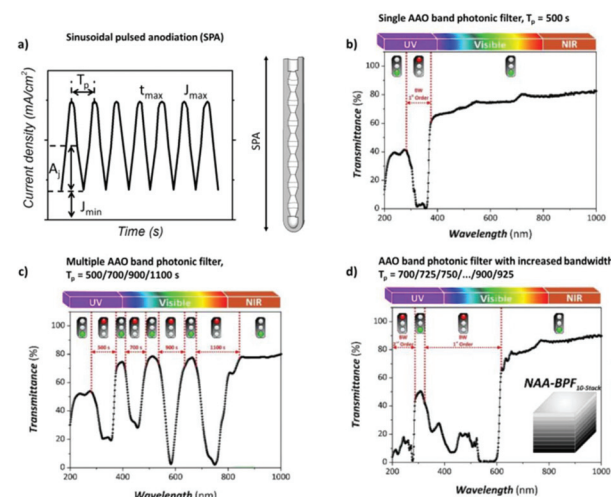


**Fig. 26** (a) Typical applied current profile during the fabrication of porous alumina optical filters and graphical description of the anodization parameters ($T_p$ = anodization period, $A_j$ = anodization amplitude, $J_{min}$ = minimum current density, $J_{max}$ = maximum current density, $t_{min}$ = time at $J_{min}$, and $t_{max}$ = time at $J_{max}$) to the left. Right, illustration establishing the correlation between the profile of the applied current curve and the final pore geometry of the AAO membrane. Reprinted with permission from ref. 364. Copyright © 2018 The Royal Society of Chemistry. (b) Transmission spectrum of a single AAO band photonic filter with characteristic stop band at 331 nm associated with $T_p$ = 500 s. (c) Transmission spectra of multiple AAO band photonic structure filters with designed stopbands at an anodizing time of 500 s, 700 s, 900 s, and 1100 s. (d) Transmission spectra of an AAO band photonic filter with huge bandwidth by increasing the anodization period in increments of 25 s, from 700s to 925 s. Reprinted with permission from ref. 366. Copyright © 2016 The Royal Society of Chemistry.

period of 500 s. In the latter case, the time between pulses is systematically changed in a way that several stopped and permitted bands are fitted in the spectra (Fig. 26c), or if time changes are introduced in small time increments, the bands remain centered while their amplitude increases (Fig. 26d).[366]

These gradient-index filters have proved to be useful for sensing applications.[16,368,369] Several studies show that engineering of the porous alumina structure can improve its sensibility to certain molecules (*i.e.*, detection of different concentration levels of D-glucose, where the sensibility of the GIF structure towards changes in the refractive index was enhanced, the detention limit of 4.93 nm M$^{-1}$ was reduced to 0.01 M).[368] Moreover, the functionalization of the alumina surface further improves the sensing capability of the alumina gradient filters. For example, thiol-modified surface AAO-GIFs were developed with increased sensibility to Hg$^{2+}$.[369] Using more complex functionalizing agents such as amino acids or proteins, more complex detection systems for vitamins and drugs[370,371] were designed.

Another interesting application making use of more complex AAO-GIFs systems with tuned located narrow peaks through multiple-sinusoidal anodization (MSPA, consisting of the combination of multiple sinusoidal waves) was proposed by Santos *et al.* for optical encoding of information within the porous alumina structure based on a color barcode system.[367] They fabricated an 8-bit encoding system with ON(1) and OFF (0) states by enabling or suppressing certain transmission peaks through modulation of the depth of the pore channels. Additionally, each of the different possible combinations of ON/OFF states was associated with a specific interferometric colour. The developed color barcode encoding system is shown in Fig. 27.

A different application of alumina porous membranes with gradient refractive index structures is the development of anti-reflective films. In this case, the refractive index of the photonic crystal structure is gradually reduced in a layered structure, which can be divided into different regions according to the refractive index of each layer (region) by changing the pore diameter and length. Then, the refractive index can range from a value close to that of the aluminium substrate (Region III, located at the bottom of the membrane) to a value matching the refractive index of air (Region I, top side close to the air surface). The resulting graded refractive index layered structure showed a broad transmission band up to an angle of 85° incidence light, and hence the reflectance of the porous alumina membrane was greatly suppressed, having omnidirectional properties. This is important to suppress the energy loss in the form of reflected light since it happens at the interfaces between different media having different refractive indices, for instance in solar cells.[372]

### 7.3 Biosensors and other biomedical applications

Self-ordered nanoporous alumina also provides a powerful platform for biosensors and biomedical applications. This is due to the increased surface area to volume ratio of these porous membranes, which are characterized by a high density
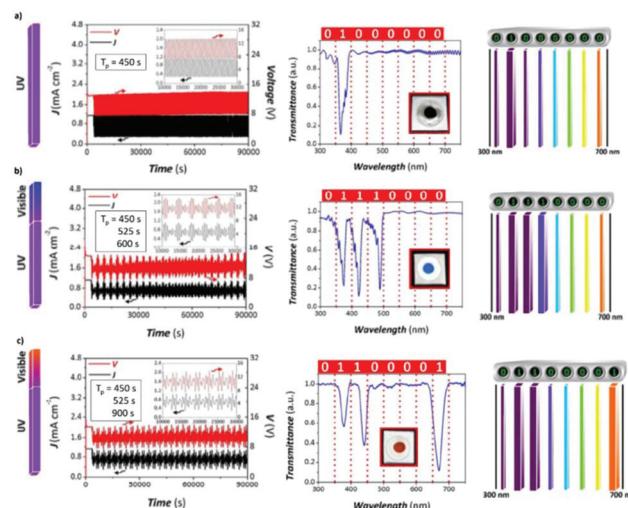


**Fig. 27** Generation of an 8-bit encoding system in AAO-GIF photonic crystal structures by MSPA. Left, multiple sinusoidal applied waveforms (inset shows a magnified view of the anodizing profiles). Center transmission spectrum (inset image interferometric color response of the photonic crystal structure) and right photonic bar code. Corresponding to (a) AAO-GIF photonic crystal structure with code 01000000 (number of waves ON = 1, $T_p$ = 400 s) and (b) AAO-GIF photonic crystal structure with code 01110000 (number of waves ON = 3, $T_p$ = 400, 525, and 600 s). (c) AAO-GIF photonic crystal structure with code 01100001 (number of waves ON = 3, $T_p$ = 400, 525, and 900 s). Reprinted with permission from ref. 367. Copyright © 2016 The Royal Society of Chemistry.

of uniform pores with diameters in the nanometer scale with control over the pore sizes (length and diameter), in large areas of a chemical stable composite, which can be easily tailored and fabricated. To sense biomolecules, it is usually necessary to place other molecules to act as active molecules for bioconjugation with the target molecules, which can be done in the large surface to volume ratio that the pore walls offer. Based on this technology, a wide variety of biosensors have been produced, including glucose, DNA, and protein detection in porous alumina templates (some examples were given in section 7.2). Other biosensing strategies are based on coating the alumina templates with different metals, which enhances the sensitivity and the performance of the sensors (due to surface plasmon resonance at the metal-AAO film interface, see section 7.1). Complete reviews of the biosensing applications based on anodic alumina can be found in ref. 18 and 373, ranging from the detection of simple (glucose), and more complex molecules (proteins, enzymes, DNA, *etc.*) or even viruses, to the detection of living cells (tumor cells). Most of the methods for sensing using these platforms are based on interferometric measurements such as interferometric reflectance spectroscopy. Accordingly, it is worth highlighting the recent review by Tabrizi *et al.*,[19] where a variety of applications using nanoporous anodic alumina for biosensing and sensing were presented. Among them, when alumina was modified with trypsin for the detection of cytochrome, a sensibility of up to 100 nM was achieved, which was used as cancer marker. Also, in using plasmonic absorption spectra (see for instance

ref. 20), gold nanoparticle nanocomposites fabricated in anodic alumina were used to detect DNA.

The characteristics of porous alumina also make it a good candidate as a drug delivery system, showing some advantages such controlled drug release that can be sustained over long periods, with no observed bursting effects (where high doses of the load are released in the early stage), chemical stability of alumina membranes and the bonus of the possibility of functionalizing the surface to promote selective release (a review on this application can be found in ref. 374). The dependence on the total drug load and diffusion kinetics of the subsequent drug release on pore geometry has been reported.[21] Three different structures were studied, including straight pores, nano funnels consisting of different layers with decreasing pore diameters (from top to bottom), and inverted nano-funnels. The first two showed a linear relationship between the amount of drug loaded with pore volume. The latter showed a higher degree of loading amount of drug per unit volume and a slower release rate of the drug, which is associated with the bottle-neck geometry of the pores and smaller pore diameter of the top layer, hindering the diffusion of the drug out of the alumina, while favoring drug loading. Inverted nano-funnels are adequate as long-term release drug systems. However, if higher release rates are required, then straight pore structures are more appropriate. Also, higher release rates have been achieved by reducing the diameter, $d$, of the pores at the top surface by adding a polymer layer ($d < 5$ nm). The main challenge in this field is to extend the time release by more 3 months,[375] and even though there are some promising works,[22] this goal is yet to be realized.

Other strategies include the aforementioned chemical tuning of the alumina surface (*i.e.*, hydrophobic or hydrophilic functional groups can alter the water affinity of the loaded drug and its release rate).[375,376] The influence of the pH of the medium has also been investigated by researchers.[25] More novel intelligent drug release approaches are based on induced changes in the alumina structures to external stimuli (change in the pH, inducing electromagnetic fields, *etc.*) to have better control over the way and when the drug is released, and the exact amount that is required in each situation. For example, if the AAO is coated with a polymer, polymerization, and depolymerization of this top layer can be controlled by an applied external field through electrochemical polymerization. Consequently, the opening and closing of the pores can be controlled through an external electric field.[23] The addition of iron particles to trigger the release of the load whenever a magnetic field is applied has also been reported.[375] Recently, a process for the photoresponse-controlled transport of molecules has been developed, where alumina was modified with certain peptides that are sensitive to light exposure, undergoing reversible isomerism transformations. Consequently, the transport of molecules could be switched on and off by an optical stimulus.[24] Finally, taking advantage of its high surface to volume ratio and different morphologies that can be achieved, there are also studies on the application of nanoporous alumina for tissue engineering, providing large areas of
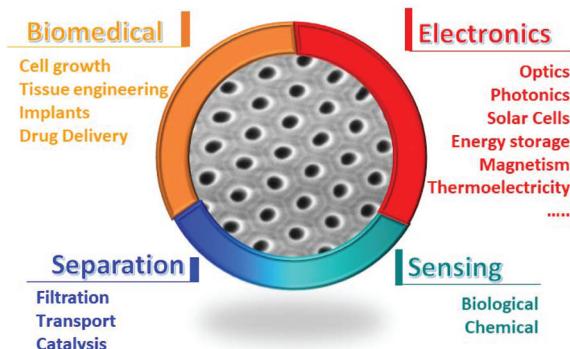


**Fig. 28** Visual summary of some of the most important applications in which AAO platforms have been used, either as templates or as grown.

hydrophilic or hydrophobic surfaces, depending on the application, for cell proliferation, tissue migration, *etc.*[377]

### 7.4 Adsorption

Another important property of nanoporous alumina is that the adsorption on its surface is very sensitive to its morphology and structural features, such as pore diameter and roughness of its top surface layer. Similarly, the adsorption of different substances along the pore walls is affected by the shape and structural properties of the vertical channels (modulation of their diameter, length, roughness of the pores, *etc.*, see ref. 378). These studies are quite relevant for their use as biosensors, where the pores should be activated to detect certain molecules. Also, this property can be exploited for applications such as humidity sensors.[379] A further step in these studies is the fabrication of superhydrophobic surfaces by fabricating a highly rough structure with the combination of hard anodization and mild anodization, protecting the material from corrosion, bacteria growth, *etc.* in a cheap way that is easy to be produced in big areas.[380]

In summary, there is a wide variety of applications in which AAOs have been implemented to date. Fig. 28 shows the most important applications discussed in sections 6 and 7.

## 8 Conclusions

AAO membranes have proved to be a powerful and versatile tool for the development of future technologies, with many different applications in a wide variety of fields. One of their main advantages is their low production cost, which makes alumina-based devices cheaper and more easily scalable to industry production than nanostructures fabricated by other techniques, such as lithography. The latest fundamental studies devoted to understanding their formation mechanisms to achieve better control over the produced structures have been reviewed in this work, together with the different regimes at which ordered porous aluminium anodization can be produced (mild and hard anodization). Accordingly, a whole set of

**Table 2** Summary of the different morphologies that can be obtained for alumina membranes (straight pores, branched pores, and modulated or interconnected pores) and possible modifications of the pore shape and geometry, the structures that can be grown by several deposition techniques when acting as templates and the direct applications of these membranes according to their different morphologies

| Morphology | Example | Uses as template | Uses as grown |
|---|---|---|---|
| Pre-patterned guided porous structure[a] | | 1) Square-dot arrays** 2) Triangular nanotubes*** 3) Highly ordered cylinders**** | Photonic devices |
| Ordered nanoporous structure[b] | | 1) Nanowires 2) Nanotubes ●● 3) Nanomeshes ●●● | Structural coloration Fabry Pérot adsorption |
| Branched structure[c] | | 1) Y-branched NWs or NTs □□ 2) Multi branched NWs or NTs □□ 3) Hierrachically branched NWs/NTs □□□ | Drug delivery biosensors |
| Modulated in diameter nanopores[d] | | Modulated NWs or NTs ◊◊ | Structural coloration: DBR, photonic crystals, optical microcavities, graded index filters and biosensors |
| Nanoporous structure[e] | | 3D Nanowire-networks◊◊ | Structural coloration: Distributed Bragg, reflector, photonic crystals and biosensors |

[a] Reprinted with permission from ref. 192. Copyright © 2009, AIP Publishing and ref. 180. Copyright © 2011, the American Chemical Society. **Reprinted with permission from ref. 229. Copyright © 2015, the American Chemical Society. ***Reprinted with permission from ref. 335. Copyright © 2004 WILEY-VCH Verlag GmbH & Co. KGaA, Weinheim. ****Reprinted with permission from the Japan Society of Applied Physics from ref. 230. [b] Reprinted with permission from ref. 336. Copyright © 2015 Yao *et al.*, licensee Springer. ●●Reprinted with permission from ref. 337. ●●●Reprinted with permission from ref. 66 Copyright © 2016, Springer Nature. [c] Reprinted with permission from ref. 300. Copyright © the Owner Societies 2015, and from ref. 201. Copyright © 2008 WILEY-VCH Verlag GmbH & Co. KGaA, Weinheim. □□Reprinted with permission from ref. 338. Copyright © 2005 the National Academy of Science, U.S.A. □□□Reprinted with permission from ref. 53 Copyright © 2010 WILEY-VCH Verlag GmbH & Co. KGaA, Weinheim. [d] Reprinted with permission from ref. 339. Copyright © 2010 WILEY–VCH Verlag GmbH & Co. KGaA, Weinheim. ◊Reprinted with permission from ref. 220. Copyright © 2018, the American Chemical Society. ◊◊Reprinted with permission from ref. 340. Copyright© 2018 by MDPI. [e] Reprinted with permission from ref. 57. Copyright © 2018, the American Chemical Society.

structural possibilities was presented, and many different porous structures can be achieved in a controlled way.

Also, these membranes constitute reliable platforms for the nanostructuration of all types of different materials with a high degree of control over the shape to synthesize a certain material, ranging from solid nanowires, hollowed nanotubular wires, and non-continuous films of antidots arrays, to modulated (in diameter) nanowires and 3D interconnected nanowire networks (see Table 2). In these cases, the diameter of the different structures can be tuned as desired as well as the interpore distance between neighboring wires, $D_{int}$, the nanotube length, and, in the case of 3D structures, the periodic distance at which modulation of the diameter or actual interconnections along the longitudinal nanowires are generated. This opens new possibilities and ways to tailor the magnetic, electrical, and optical properties at the nanoscale for the design of next-generation devices and their implementation and improvement of existing technologies.

Finally, the most recent and relevant examples of the state-of-the-art developments and applications based on AAO membranes have been shown, from their use for structural coloration to distributed Bragg reflectors, drug delivery, and sensing applications (see Table 2). The engineering of these nanostructures enables the development of novel approaches to different problems encountered in a great variety of fields. Some of these future applications appear nowadays as challenges that are being tackled, such as the fabrication of nanowires or 3D nanostructured metamaterials with tailored properties, or the design of novel AAO nanostructures, with direct applications in fields such as biotechnology, optical detection, energy storage, conversion and generation, and filtering. For instance, 3D-AAO templates provide a way of obtaining an assembly of mechanically robust nanowires, making it possible to obtain scaffolds of interconnected nanowires. Also, the 3D-AAO structure itself provides a much higher surface to volume ratio than other structures, which can be beneficial for techniques that use activated surfaces, such as bio-sensing (virus detection, DNA, *etc.*). Most importantly, these AAO platforms will also be the answer to problems not envisaged yet in fields where they have not been traditionally used, where their outstanding properties such as thermal, chemical, and mechanical stability, control over morphology, and large area coverage can be determinant to find novel solutions.

The number of original works based on AAO membranes discussed in this review, either using their nanostructuring possibilities to nanostructure different materials in a scalable way or to directly exploit their properties, justify the importance that the understanding of their growth mechanisms has to be further developed to gain finer control over their structures. Thus, AAO membranes are a powerful and promising platform to explore novel metamaterials through nanostructuration and creative applications in a wide range of fields.

# Conflicts of interest

There are no conflicts to declare.

# Acknowledgements

# Notes and references

1 H. Masuda, H. Tanaka and N. Baba, *Chem. Lett.*, 1990, **19**, 621–622.

2 K. Schwirn, W. Lee, R. Hillebrand, M. Steinhart, K. Nielsch and U. Gösele, *ACS Nano*, 2008, **2**, 302–310.

3 C. V. Manzano, J. Martín and M. S. Martín-González, *Microporous Mesoporous Mater.*, 2014, **184**, 177–183.

4 W. Lee, R. Ji, U. Gösele and K. Nielsch, *Nat. Mater.*, 2006, **5**, 741.

5 V. Vega, J. García, J. M. Montero-Moreno, B. Hernando, J. Bachmann, V. M. Prida and K. Nielsch, *ACS Appl. Mater. Interfaces*, 2015, **7**, 28682–28692.

6 Y. Li, M. Zheng, L. Ma and W. Shen, *Nanotechnology*, 2006, **17**, 5101–5105.

7 S. Akiya, T. Kikuchi, S. Natsui, N. Sakaguchi and R. O. Suzuki, *Electrochim. Acta*, 2016, **190**, 471–479.

8 A. Takenaga, T. Kikuchi, S. Natsui and R. O. Suzuki, *ECS Solid State Lett.*, 2015, **4**, P55–P58.

9 S. Ono, M. Saito and H. Asoh, *Electrochim. Acta*, 2005, **51**, 827–833.

10 T. Kikuchi, O. Nishinaga, S. Natsui and R. O. Suzuki, *Electrochim. Acta*, 2015, **156**, 235–243.

11 S. Akiya, T. Kikuchi, S. Natsui and R. O. Suzuki, *Appl. Surf. Sci.*, 2017, **403**, 652–661.

12 J. Martín, C. V. Manzano, O. Caballero-Calero and M. Martín-González, *ACS Appl. Mater. Interfaces*, 2013, **5**, 72–79.

13 J. Martín, C. V. Manzano and M. Martín-González, *Microporous Mesoporous Mater.*, 2012, **151**, 311–316.

14 L. M. Ferro, S. G. Lemos, M. Ferreira and F. Trivinho-Strixino, *Sens. Actuators, B*, 2017, **248**, 718–723.

15 T. Kumeria, A. Santos, M. M. Rahman, J. Ferré-Borrull, L. F. Marsal and D. Losic, *ACS Photonics*, 2014, **1**, 1298–1306.

16 J. Lee, K. Bae, G. Kang, M. Choi, S. Baek, D.-S. Yoo, C.-W. Lee and K. Kim, *RSC Adv.*, 2015, **5**, 71770–71777.

17 Y. Chen, A. Santos, Y. Wang, T. Kumeria, D. Ho, J. Li, C. Wang and D. Losic, *Sci. Rep.*, 2015, **5**, 12893.

18 G. Sriram, P. Patil, M. P. Bhat, R. M. Hegde, K. V. Ajeya, I. Udachyan, M. Bhavya, M. G. Gatti, U. Uthappa and G. M. Neelgund, *J. Nanomater.*, 2016, **2016**, 1753574.

19 M. A. Tabrizi, J. Ferré-Borrull and L. F. Marsal, *Biosens. Bioelectron.*, 2020, **149**, 111828.

20 T. Lednicky and A. Bonyár, *ACS Appl. Mater. Interfaces*, 2020, **4**, 4804–4814.

21 M. Porta-i-Batalla, E. Xifré-Pérez, C. Eckstein, J. Ferré-Borrull and L. F. Marsal, *Nanomaterials*, 2017, **7**, 227.

22 S. Simovic, D. Losic and K. Vasilev, *Chem. Commun.*, 2010, **46**, 1317–1319.

23 G. Jeon, S. Y. Yang, J. Byun and J. K. Kim, *Nano Lett.*, 2011, **11**, 1284–1288.

24 T. Kumeria, J. Yu, M. Alsawat, M. D. Kurkuri, A. Santos, A. D. Abell and D. Losic, Modulating molecular transport across peptide-modified nanoporous alumina membranes with light, in *SPIE BioPhotonics Australasia*, International Society for Optics and Photonics, 2016, vol. 10013, p. 100131W.

25 M. Porta-i-Batalla, C. Eckstein, E. Xifré-Pérez, P. Formentín, J. Ferré-Borrull and L. F. Marsal, *Nanoscale Res. Lett.*, 2016, **11**, 372.

26 A. M. Mebed, A. M. Abd-Elnaiem and N. M. Al-Hosiny, *Appl. Phys. A*, 2016, **122**, 565.

27 F. Domínguez-Adame, M. Martín-González, D. Sánchez and A. Cantarero, *Phys. E*, 2019, **113**, 213–225.

28 C. V. Manzano and M. Martin-Gonzalez, *Front. Chem.*, 2019, **7**, 516.

29 G. Zhang, H. Fang, H. Yang, L. A. Jauregui, Y. P. Chen and Y. Wu, *Nano Lett.*, 2012, **12**, 3627–3633.

30 H.-P. Wang, K.-T. Tsai, K.-Y. Lai, T.-C. Wei, Y.-L. Wang and J.-H. He, *Opt. Express*, 2012, **20**, A94–A103.

31 Y. Shirai, S. Takami, S. Lasmono, H. Iwai, T. Chikyow and Y. Wakayama, *J. Polym. Sci., Part B: Polym. Phys.*, 2011, **49**, 1762–1768.

32 D. O'Carroll, D. Iacopino, A. O'Riordan, P. Lovera, É. O'Connor, G. A. O'Brien and G. Redmond, *Adv. Mater.*, 2008, **20**, 42–48.

33 C. Manzano, G. Bürki, L. Pethö, J. Michler and L. Philippe, *J. Mater. Chem. C*, 2017, **5**, 1706–1713.

34 C. d. Frantz, A. Lauria, C. V. Manzano, C. Guerra-Nuñez, M. Niederberger, C. d. Storrer, J. Michler and L. Philippe, *Langmuir*, 2017, **33**, 12404–12418.

35 E. Bertero, C. V. Manzano, G. Bürki and L. Philippe, *Mater. Des.*, 2020, 108559.

36 J. García, V. Vega, L. Iglesias, V. M. Prida, B. Hernando, E. D. Barriga-Castro, R. Mendoza-Reséndez, C. Luna, D. Görlitz and K. Nielsch, *Phys. Status Solidi A*, 2014, **211**, 1041–1047.

37 M. S. Salem, F. Tejo, R. Zierold, P. Sergelius, J. M. M. Moreno, D. Goerlitz, K. Nielsch and J. Escrig, *Nanotechnology*, 2018, **29**, 065602.

38 Y. P. Ivanov, A. Chuvilin, S. Lopatin and J. Kosel, *ACS Nano*, 2016, **10**, 5326–5332.

39 M. S. Salem, P. Sergelius, R. M. Corona, J. Escrig, D. Görlitz and K. Nielsch, *Nanoscale*, 2013, **5**, 3941–3947.

40 C. Zhao, Q. Li, W. Wan, J. Li, J. Li, H. Zhou and D. Xu, *J. Mater. Chem.*, 2012, **22**, 12193–12197.

41 M. P. Proenca, C. T. Sousa, J. Ventura and J. P. Araújo, in *Magnetic Nano- and Microwires*, ed. M. Vázquez, Woodhead Publishing, 2nd edn, 2020, pp. 135–184, DOI: 10.1016/B978-0-08-102832-2.00006-2.

42 K. Žužek Rožman, D. Pečko, S. Šturm, U. Maver, P. Nadrah, M. Bele and S. Kobe, *Mater. Chem. Phys.*, 2012, **133**, 218–224.

43 B. I. Seo, U. A. Shaislamov, M. H. Ha, S. W. Kim, H. K. Kim and B. Yang, *Physica E*, 2007, **37**, 241–244.

44 M. Norek, M. Putkonen, W. Zaleszczyk, B. Budner and Z. Bojar, *Mater. Charact.*, 2018, **136**, 52–59.

45 J. S. Lee, G. H. Gu, H. Kim, K. S. Jeong, J. Bae and J. S. Suh, *Chem. Mater.*, 2001, **13**, 2387–2391.

46 M. Alsawat, T. Altalhi, A. Santos and D. Losic, *J. Phys. Chem. C*, 2017, **121**, 13634–13644.

47 J.-W. Back, S. Lee, C.-R. Hwang, C.-S. Chi and J.-Y. Kim, *Macromol. Res.*, 2011, **19**, 33–37.

48 J. Byun, Y. Kim, G. Jeon and J. K. Kim, *Macromolecules*, 2011, **44**, 8558–8562.

49 R. M. Córdova-Castro, A. V. Krasavin, M. E. Nasir, A. V. Zayats and W. Dickson, *Nanotechnology*, 2018, **30**, 055301.

50 G. Meng, F. Han, X. Zhao, B. Chen, D. Yang, J. Liu, Q. Xu, M. Kong, X. Zhu, Y. J. Jung, Y. Yang, Z. Chu, M. Ye, S. Kar, R. Vajtai and P. M. Ajayan, *Angew. Chem., Int. Ed.*, 2009, **48**, 7166–7170.

51 L. Sacco, I. Florea, M. Châtelet and C.-S. Cojocaru, *J. Phys.: Mater.*, 2018, **1**, 015004.

52 Y. Tian, G. Meng, S. K. Biswas, P. M. Ajayan, S. Sun and L. Zhang, *Appl. Phys. Lett.*, 2004, **85**, 967–969.

53 B. Chen, Q. Xu, X. Zhao, X. Zhu, M. Kong and G. Meng, *Adv. Funct. Mater.*, 2010, **20**, 3791–3796.

54 X. Li, G. Meng, Q. Xu, M. Kong, X. Zhu, Z. Chu and A.-P. Li, *Nano Lett.*, 2011, **11**, 1704–1709.

55 S. Mahima, R. Kannan, I. Komath, M. Aslam and V. K. Pillai, *Chem. Mater.*, 2008, **20**, 601–603.

56 H. Jo, N. Haberkorn, J.-A. Pan, M. Vakili, K. Nielsch and P. Theato, *Langmuir*, 2016, **32**, 6437–6444.

57 S. P. Zankowski and P. M. Vereecken, *ACS Appl. Mater. Interfaces*, 2018, **10**, 44634–44644.

58 N. Kim, E. Sahadeo, C. Liu, O. Rose, G. Rubloff and S. B. Lee, *Phys. Chem. Chem. Phys.*, 2018, **20**, 29708–29716.

59 A. Ruiz-Clavijo, S. Ruiz-Gomez, O. Caballero-Calero, L. Perez and M. Martin-Gonzalez, *Phys. Status Solidi RRL*, 2019, **13**, 1900263.

60 A. Ruiz-Clavijo, O. Caballero-Calero and M. Martín-González, *Nanomaterials*, 2018, **8**, 345.

61 P. M. Resende, R. Sanz, O. Caballero-Calero and M. Martín-González, *Adv. Opt. Mater.*, 2018, **6**, 1800408.

62 A. García-Barberá, M. Culebras, S. Roig-Sánchez, C. M. Gómez and A. Cantarero, *Synth. Met.*, 2016, **220**, 208–212.

63 D. Navas, F. Ilievski and C. A. Ross, *J. Appl. Phys.*, 2009, **105**, 113921.

64 M. Vázquez, K. R. Pirota, D. Navas, A. Asenjo, M. Hernández-Vélez, P. Prieto and J. M. Sanz, *J. Magn. Magn. Mater.*, 2008, **320**, 1978–1983.

65 Y. Xiang, Q.-l. Xia, J.-h. Luo, Y.-p. Liu, Y.-d. Peng, D.-w. Wang, Y.-z. Nie and G.-h. Guo, *Solid State Commun.*, 2018, **281**, 1–5.

66 J. A. Perez-Taborda, M. Muñoz Rojo, J. Maiz, N. Neophytou and M. Martin-Gonzalez, *Sci. Rep.*, 2016, **6**, 32778.

67 J. Tang, H.-T. Wang, D. H. Lee, M. Fardy, Z. Huo, T. P. Russell and P. Yang, *Nano Lett.*, 2010, **10**, 4279–4283.

68 Z. Zeng, X. Huang, Z. Yin, H. Li, Y. Chen, H. Li, Q. Zhang, J. Ma, F. Boey and H. Zhang, *Adv. Mater.*, 2012, **24**, 4138–4142.

69 L. Zhang, L. Jin, B. Liu and J. He, *Front. Chem.*, 2019, **7**, 22.

70 V. Malgras, Q. Ji, Y. Kamachi, T. Mori, F.-K. Shieh, K. C.-W. Wu, K. Ariga and Y. Yamauchi, *Bull. Chem. Soc. Jpn.*, 2015, **88**, 1171–1200.

71 G. Williams, M. Hunt, B. Boehm, A. May, M. Taverne, D. Ho, S. Giblin, D. Read, J. Rarity and R. Allenspach, *Nano Res.*, 2018, **11**, 845–854.

72 M. F. Wagner, F. Völklein, H. Reith, C. Trautmann and M. E. Toimil-Molares, *Phys. Status Solidi A*, 2016, **213**, 610–619.

73 C. Li, Q. Li, Y. V. Kaneti, D. Hou, Y. Yamauchi and Y. Mai, *Chem. Soc. Rev.*, 2020, **49**, 4681–4736.

74 Q. Wang and D. Astruc, *Chem. Rev.*, 2019, **120**, 1438–1511.

75 C. Healy, K. M. Patil, B. H. Wilson, L. Hermanspahn, N. C. Harvey-Reid, B. I. Howard, C. Kleinjan, J. Kolien, F. Payet and S. G. Telfer, *Coord. Chem. Rev.*, 2020, **419**, 213388.

76 B. Singh, J. Na, M. Konarova, T. Wakihara, Y. Yamauchi, C. Salomon and M. B. Gawande, *Bull. Chem. Soc. Jpn.*, 2020, **93**, 1459–1496.

77 L. Vera-Londono, A. Ruiz-Clavijo, O. Caballero-Calero and M. Martín-González, *Nanoscale Adv.*, 2020, **2**, 4591–4603.

78 K. Nishio, *Electrochem. Commun.*, 2017, **82**, 30–33.

79 Y. Yang, H. Fei, G. Ruan and J. M. Tour, *Adv. Mater.*, 2015, **27**, 3175–3180.

80 B. Hu, W. Zhang, C. Yu, Z. Zheng, Y. Chen, J. Wang, J. Liu, K. Ma and W. Ren, *Ind. Eng. Chem. Res.*, 2019, **58**, 7131–7138.

81 B. Pandey, P. S. Thapa, D. A. Higgins and T. Ito, *Langmuir*, 2012, **28**, 13705–13711.

82 A. Zaffora, F. Di Franco, F. Di Quarto, R. Macaluso, M. Mosca, H. Habazaki and M. Santamaria, *ECS J. Solid State Sci. Technol.*, 2017, **6**, N25.

83 M. Martin-Gonzalez, R. Martinez-Moro, M. H. Aguirre, E. Flores and O. Caballero-Calero, *Electrochim. Acta*, 2020, **330**, 135241.

84 J. S. Kang, J. Kim, M. J. Lee, Y. J. Son, D. Y. Chung, S. Park, J. Jeong, J. M. Yoo, H. Shin and H. Choe, *Adv. Sci.*, 2018, **5**, 1700601.

85 M. Altomare, G. Cha and P. Schmuki, *Electrochim. Acta*, 2020, 136158.

86 L. Zaraska, K. Gawlak, M. Gurgul, M. Dziurka, M. Nowak, D. Gilek and G. D. Sulka, *Appl. Surf. Sci.*, 2018, **439**, 672–680.

87 R. Sanz, M. A. Buccheri, M. Zimbone, V. Scuderi, G. Amiard, G. Impellizzeri, L. Romano and V. Privitera, *Appl. Surf. Sci.*, 2017, **399**, 451–462.

88 J. Kapusta-Kołodziej, A. Chudecka and G. D. Sulka, *J. Electroanal. Chem.*, 2018, **823**, 221–233.

89 T. Kikuchi, J. Kawashima, S. Natsui and R. O. Suzuki, *Appl. Surf. Sci.*, 2017, **422**, 130–137.

90 H. Lee, V. S. Kumbhar, J. Lee, Y. Choi and K. Lee, *Electrochim. Acta*, 2020, **334**, 135618.

91 K. Mika, R. P. Socha, P. Nyga, E. Wiercigroch, K. Małek, M. Jarosz, T. Uchacz, G. D. Sulka and L. Zaraska, *Electrochim. Acta*, 2019, **305**, 349–359.

92 S. N. Patel, V. Jayaram and D. Banerjee, *Surf. Coat. Technol.*, 2017, **323**, 2–9.

93 G. E. Thompson and G. C. Wood, in *Treatise on Materials Science and Technology*, ed. J. C. Scully, Elsevier, 1983, vol. 23, pp. 205–329.

94 S. Chu, K. Wada, S. Inoue, M. Isogai, Y. Katsuta and A. Yasumori, *J. Electrochem. Soc.*, 2006, **153**, B384–B391.

95 J. O'Sullivan and G. Wood, *Proc. R. Soc. London, Ser. A*, 1970, **317**, 511–543.

96 S. Ono, M. Saito, M. Ishiguro and H. Asoh, *J. Electrochem. Soc.*, 2004, **151**, B473.

97 K. Nielsch, J. Choi, K. Schwirn, R. B. Wehrspohn and U. Gösele, *Nano Lett.*, 2002, **2**, 677–680.

98 F. Li, L. Zhang and R. M. Metzger, *Chem. Mater.*, 1998, **10**(9), 2470–2480.

99 G. Sulka and K. G. Parkoła, *Electrochim. Acta*, 2007, **52**, 1880–1888.

100 S.-K. Hwang, S.-H. Jeong, H.-Y. Hwang, O.-J. Lee and K.-H. Lee, *Korean J. Chem. Eng.*, 2002, **19**, 467–473.

101 V. Parkhutik and V. Shershulsky, *J. Phys. D: Appl. Phys.*, 1992, **25**, 1258.

102 M. Pashchanka and J. J. Schneider, *J. Phys. Chem. C*, 2016, **120**, 14590–14596.

103 A. L. Friedman, D. Brittain and L. Menon, *J. Chem. Phys.*, 2007, **127**, 154717.

104 G. D. Sulka, *Nanostruct. Mater. Electrochem.*, 2008, **1**, 1–116.

105 D. Losic and A. Santos, *Nanoporous Alumina: Fabrication, Structure, Properties and Applications, Springer Series in Materials Science*, Springer International Publishing Switzerland, 2015, vol. 219, ISBN 978-3-319-20333-1.

106 W. Lee and S.-J. Park, *Chem. Rev.*, 2014, **114**, 7487–7556.

107 O. Nishinaga, T. Kikuchi, S. Natsui and R. O. Suzuki, *Sci. Rep.*, 2013, **3**, 2748.

108 T. Kikuchi, O. Nishinaga, S. Natsui and R. O. Suzuki, *Electrochim. Acta*, 2014, **137**, 728–735.

109 S. Akiya, T. Kikuchi, S. Natsui and R. O. Suzuki, *J. Electrochem. Soc.*, 2015, **162**, E244–E250.

110 W. J. Stępniowski, M. Moneta, M. Norek, M. Michalska-Domańska, A. Scarpellini and M. Salerno, *Electrochim. Acta*, 2016, **211**, 453–460.

111 S. Stojadinovic, R. Vasilic, I. Belca, M. Tadic, B. Kasalica and L. Zekovic, *Appl. Surf. Sci.*, 2008, **255**, 2845–2850.

112 R. Kondo, D. Nakajima, T. Kikuchi, S. Natsui and R. O. Suzuki, *J. Alloys Compd.*, 2017, **725**, 379–387.

113 W. Lee, K. Nielsch and U. Gösele, *Nanotechnology*, 2007, **18**, 475713.

114 J. Bellemare, F. Sirois and D. Ménard, *J. Electrochem. Soc.*, 2014, **161**, E75.

115 H. Masuda and K. Fukuda, *Science*, 1995, **268**, 1466–1468.

116 H. Masuda, K. Yada and A. Osaka, *Jpn. J. Appl. Phys.*, 1998, **37**, L1340–L1342.

117 H. Masuda, *J. Electrochem. Soc.*, 1997, **144**, L127.

118 X. Chen, D. Yu, L. Cao, X. Zhu, Y. Song, H. Huang, L. Lu and X. Chen, *Mater. Res. Bull.*, 2014, **57**, 116–120.

119 S.-Z. Chu, K. Wada, S. Inoue, M. Isogai and A. Yasumori, *Adv. Mater.*, 2005, **17**, 2115–2119.

120 O. Jessensky, F. Muller and U. Gosele, *Appl. Phys. Lett.*, 1998, **72**, 1173–1175.

121 E. O. Gordeeva, I. V. Roslyakov and K. S. Napolskii, *Electrochim. Acta*, 2019, **307**, 13–19.

122 S. Shingubara, K. Morimoto, H. Sakaue and T. Takahagi, *Electrochem. Solid-State Lett.*, 2004, **7**, E15.

123 M. Almasi Kashi, A. Ramazani, Y. Mayamai and M. Noormohammadi, *Jpn. J. Appl. Phys.*, 2010, **49**, 015202.

124 Y.-f. Xu, H. Liu, X.-j. Li, W.-m. Kang, B.-w. Cheng and X.-j. Li, *Mater. Lett.*, 2015, **151**, 79–81.

125 M. Almasi Kashi and A. Ramazani, *Int. J. Nanosci. Nanotechnol.*, 2010, **6**, 78–87.

126 H. A. Rayat Azimi, M. Zarei, A. Rafati and M. Noormohammadi, *J. Porous Mater.*, 2016, **23**, 357–363.

127 R. Kanakala, P. Singaraju, R. Venkat and B. Das, *J. Electrochem. Soc.*, 2005, **152**, J1–J5.

128 E. Verwey, *Physica*, 1935, **2**, 1059–1063.

129 N. Cabrera and N. F. Mott, *Rep. Prog. Phys.*, 1949, **12**, 163–184.

130 J. Dewald, *J. Electrochem. Soc.*, 1955, **102**, 1.

131 L. Zhang, D. D. Macdonald, E. Sikora and J. Sikora, *J. Electrochem. Soc.*, 1998, **145**, 898.

132 M. Lohrengel, *Mater. Sci. Eng., R*, 1993, **11**, 243–294.

133 D. LeClere, A. Velota, P. Skeldon, G. Thompson, S. Berger, J. Kunze, P. Schmuki, H. Habazaki and S. Nagata, *J. Electrochem. Soc.*, 2008, **155**, C487.

134 K. Shimizu, K. Kobayashi, G. Thompson and G. Wood, *Philos. Mag. A*, 1992, **66**, 643–652.

135 F. Keller, M. Hunter and D. Robinson, *J. Electrochem. Soc.*, 1953, **100**, 411.

136 T. Hoar and J. Yahalom, *J. Electrochem. Soc.*, 1963, **110**, 614–621.

137 G. Wood and J. O'Sullivan, *Electrochim. Acta*, 1970, **15**, 1865–1876.

138 G. Thompson, *Thin Solid Films*, 1997, **297**, 192–201.

139 S. Garcia-Vergara, P. Skeldon, G. Thompson and H. Habazaki, *Electrochim. Acta*, 2006, **52**, 681–687.

140 J. E. Houser and K. R. Hebert, *Nat. Mater.*, 2009, **8**, 415–420.

141 J. E. Houser and K. R. Hebert, *Phys. Status Solidi A*, 2008, **205**, 2396–2399.

142 K. R. Hebert and J. E. Houser, *J. Electrochem. Soc.*, 2009, **156**, C275–C281.

143 X. Zhu, L. Liu, Y. Song, H. Jia, H. Yu, X. Xiao and X. Yang, *Monatsh. Chem. – Chem. Monthly*, 2008, **139**, 999–1003.

144 M. Nagayama and K. Tamura, *Electrochim. Acta*, 1967, **12**, 1097–1107.

145 R. B. Mason, *J. Electrochem. Soc.*, 1955, **102**, 671.

146 J. Oh, Porous Anodic Aluminum Oxide Scaffolds, Formation Mechanisms and Applications, Massachusetts Institute of Technology, 2010.

147 M. Hunter and P. Fowle, *J. Electrochem. Soc.*, 1954, **101**, 514.

148 S. K. Thamida and H.-C. Chang, *Chaos*, 2002, **12**, 240–251.

149 G. Singh, A. Golovin and I. Aranson, *Phys. Rev. B: Condens. Matter Mater. Phys.*, 2006, **73**, 205422.

150 J. E. Houser and K. R. Hebert, *J. Electrochem. Soc.*, 2006, **153**, B566–B573.

151 Z. Su, G. Hähner and W. Zhou, *J. Mater. Chem.*, 2008, **18**, 5787–5795.

152 J. Siejka and C. Ortega, *J. Electrochem. Soc.*, 1977, **124**, 883–891.

153 A. Baron-Wiecheć, J. Ganem, S. Garcia-Vergara, P. Skeldon, G. Thompson and I. Vickridge, *J. Electrochem. Soc.*, 2010, **157**, C399–C407.

154 H. Takahashi and M. Nagayama, *Corros. Sci.*, 1978, **18**, 911–925.

155 Z. Wu, C. Richter and L. Menon, *J. Electrochem. Soc.*, 2007, **154**, E8–E12.

156 P. Skeldon, G. Thompson, S. Garcia-Vergara, L. Iglesias-Rubianes and C. Blanco-Pinzon, *Electrochem. Solid-State Lett.*, 2006, **9**, B47–B51.

157 N. Sato, *Electrochim. Acta*, 1971, **16**, 1683–1692.

158 A. Li, F. Müller, A. Birner, K. Nielsch and U. Gösele, *J. Appl. Phys.*, 1998, **84**, 6023–6026.

159 I. Vrublevsky, V. Parkoun, V. Sokol, J. Schreckenbach and G. Marx, *Appl. Surf. Sci.*, 2004, **222**, 215–225.

160 I. Vrublevsky, V. Parkoun, J. Schreckenbach and G. Marx, *Appl. Surf. Sci.*, 2003, **220**, 51–59.

161 S. Ono and N. Masuko, *Corros. Sci.*, 1992, **33**, 503–507.

162 H. Takahashi, K. Fujimoto, H. Konno and M. Nagayama, *J. Electrochem. Soc.*, 1984, **131**, 1856.

163 I. Mínguez-Bacho, S. Rodríguez-López, A. Climent, D. Fichou, M. Vázquez and M. Hernández-Vélez, *J. Phys. Chem. C*, 2015, **119**, 27392–27400.

164 P. Mishra and K. R. Hebert, *Electrochim. Acta*, 2016, **222**, 1186–1190.

165 K. R. Hebert and P. Mishra, *J. Electrochem. Soc.*, 2018, **165**, E737–E743.

166 K. R. Hebert and P. Mishra, *J. Electrochem. Soc.*, 2018, **165**, E744–E750.

167 P. Mishra and K. R. Hebert, *Electrochim. Acta*, 2020, 135879.

168 S. Garcia-Vergara, H. Habazaki, P. Skeldon and G. Thompson, *Nanotechnology*, 2007, **18**, 415605.

169 S. Garcia-Vergara, P. Skeldon, G. Thompson and H. Habazaki, *Corros. Sci.*, 2007, **49**, 3772–3782.

170 F.-y. Zhou, A. M. Al-Zenati, A. Baron-Wiecheć, M. Curioni, S. Garcia-Vergara, H. Habazaki, P. Skeldon and G. Thompson, *J. Electrochem. Soc.*, 2011, **158**, C202.

171 X. Zhu, D. Li, Y. Song and Y. Xiao, *Mater. Lett.*, 2005, **59**, 3160–3163.

172 D. Li, C. Jiang, J. Jiang and J. G. Lu, *Chem. Mater.*, 2009, **21**, 253–258.

173 D. Li, L. Zhao, C. Jiang and J. G. Lu, *Nano Lett.*, 2010, **10**, 2766–2771.

174 X.-F. Zhu, Y. Song, L. Liu, C.-Y. Wang, J. Zheng, H.-B. Jia and X.-L. Wang, *Nanotechnology*, 2009, **20**, 475303.

175 H. Fan, T. Lin, W. Zhang, J. Ma, S. Lu and X. Zhu, *Mater. Res. Bull.*, 2017, **90**, 119–124.

176 S. Heinschke and J. J. Schneider, *J. Phys. Chem. C*, 2020, **124**, 11913–11921.

177 M. Pashchanka, *Phys. Chem. Chem. Phys.*, 2020, **22**(28), 15867–15875.

178 M. Pashchanka and J. J. Schneider, *J. Mater. Chem.*, 2011, **21**, 18761–18767.

179 H. Masuda and M. Satoh, *Jpn. J. Appl. Phys.*, 1996, **35**, L126.

180 B. Chen, K. Lu and Z. Tian, *Langmuir*, 2011, **27**, 800–808.

181 K. Lu, *Electrochim. Acta*, 2012, **63**, 256–262.

182 B. Chen and K. Lu, *Langmuir*, 2011, **27**, 4117–4125.

183 Z. Tian, K. Lu and B. Chen, *J. Appl. Phys.*, 2010, **108**, 094306.

184 K. Lu and J. Zhao, *J. Nanosci. Nanotechnol.*, 2010, **10**, 6760–6768.

185 S. Shingubara, Y. Murakami, K. Morimoto and T. Takahagi, *Surf. Sci.*, 2003, **532**, 317–323.

186 M. Jaafar, D. Navas, M. Hernández-Vélez, J. Baldonedo, M. Vázquez and A. Asenjo, *Surf. Sci.*, 2009, **603**, 3155–3159.

187 Z. Sun and H. K. Kim, *Appl. Phys. Lett.*, 2002, **81**, 3458–3460.

188 B. Kim, S. Park, T. J. McCarthy and T. P. Russell, *Small*, 2007, **3**, 1869–1872.

189 A. Yin, M. Tzolov, D. Cardimona, L. Guo and J. Xu, *IET Circuits, Devices Syst.*, 2007, **1**, 205–209.

190 V. Stasi, G. Cattaneo, S. Franz, M. Bestetti, M. Ubaldi, D. Piccinin and S. M. Pietralunga, *Photonics and Nanostructures-Fundamentals and Applications*, 2007, **5**, 136–139.

191 T. S. Kustandi, W. W. Loh, H. Gao and H. Y. Low, *ACS Nano*, 2010, **4**, 2561–2568.

192 J. T. Smith, Q. Hang, A. D. Franklin, D. B. Janes and T. D. Sands, *Appl. Phys. Lett.*, 2008, **93**, 043108.

193 A. Maria Chong, L. K. Tan, J. Deng and H. Gao, *Adv. Funct. Mater.*, 2007, **17**, 1629–1635.

194 H. Masuda, H. Yamada, M. Satoh, H. Asoh, M. Nakao and T. Tamamura, *Appl. Phys. Lett.*, 1997, **71**, 2770–2772.

195 H. Masuda, M. Yotsuya, M. Asano, K. Nishio, M. Nakao, A. Yokoo and T. Tamamura, *Appl. Phys. Lett.*, 2001, **78**, 826–828.

196 W. Lee, R. Ji, C. A. Ross, U. Gösele and K. Nielsch, *Small*, 2006, **2**, 978–982.

197 D. Navas, O. Sanchez, A. Asenjo, M. Jaafar, J. Baldonedo, M. Vazquez and M. Hernandez-Velez, *Nanotechnology*, 2007, **18**, 165302.

198 X. Wang, S. Xu, M. Cong, H. Li, Y. Gu and W. Xu, *Small*, 2012, **8**, 972–976.

199 W. Im, Y. Cho, G. Choi, F. Yu and D. Kim, *Diamond Relat. Mater.*, 2004, **13**, 1214–1217.

200 C. Sousa, A. Apolinário and D. Leitão, *Adv. Nanotechnol.*, 2014, **12**, 123.

201 A. Y. Y. Ho, H. Gao, Y. C. Lam and I. Rodriguez, *Adv. Funct. Mater.*, 2008, **18**, 2057–2063.

202 C. Shuoshuo, L. Zhiyuan, H. Xing, Y. Hui and L. Yi, *J. Mater. Chem.*, 2010, **20**, 1794–1798.

203 R. Krishnan and C. V. Thompson, *Adv. Mater.*, 2007, **19**, 988–992.

204 C. Sousa, A. Apolinario, D. Leitao, A. Pereira, J. Ventura and J. Araujo, *J. Mater. Chem.*, 2012, **22**, 3110–3116.

205 D. Guo, L. Fan, J. Sang, Y. Liu, S. Huang and X. Zou, *Nanotechnology*, 2007, **18**, 405304.

206 J. Zhang, C. S. Day and D. L. Carroll, *Chem. Commun.*, 2009, 6937–6939.

207 R. Zakeri, C. Watts, H. Wang and P. Kohli, *Chem. Mater.*, 2007, **19**, 1954–1963.

208 S. Jin, Y. Li, Z. Li, X. Hu, Z. Ling, X. He, Y. Shen and L. Jin, *J. Electrochem. Soc.*, 2016, **163**, H1053–H1059.

209 W. Cheng, M. Steinhart, U. Gösele and R. B. Wehrspohn, *J. Mater. Chem.*, 2007, **17**, 3493–3495.

210 H. Hashimoto, S. Kojima, T. Sasaki and H. Asoh, *J. Eur. Ceram. Soc.*, 2018, **38**, 1836–1840.

211 G. D. Sulka, A. Brzózka and L. Liu, *Electrochim. Acta*, 2011, **56**, 4972–4979.

212 M. Norek, W. J. Stępniowski and D. Siemiaszko, *J. Electroanal. Chem.*, 2016, **762**, 20–28.

213 P. Hoyer, K. Nishio and H. Masuda, *Thin Solid Films*, 1996, **286**, 88–91.

214 L. Yi, L. Zhiyuan, C. Shuoshuo, H. Xing and H. Xinhua, *Chem. Commun.*, 2010, **46**, 309–311.

215 L. Yi, L. Zhiyuan, H. Xing, L. Yisen and C. Yi, *RSC Adv.*, 2012, **2**, 5164–5171.

216 G. D. Sulka and K. Hnida, *Nanotechnology*, 2012, **23**, 075303.

217 D. Losic, M. Lillo and D. Losic Jr., *Small*, 2009, **5**, 1392–1397.

218 W. Lee and J.-C. Kim, *Nanotechnology*, 2010, **21**, 485304.

219 J. Liao, *Surf. Eng. Appl. Electrochem.*, 2018, **54**, 555–561.

220 H. Bayat, C.-H. Lin, M.-H. Cheng, M. Steuber, J.-T. Chen and H. Schönherr, *ACS Appl. Nano Mater.*, 2017, **1**, 200–208.

221 Y. Wang, A. Santos, A. Evdokiou and D. Losic, *Electrochim. Acta*, 2015, **154**, 379–386.

222 J. Martín, M. Martín-González, J. F. Fernández and O. Caballero-Calero, *Nat. Commun.*, 2014, **5**, 5130.

223 D. Losic and D. Losic Jr., *Langmuir*, 2009, **25**, 5426–5431.

224 P. M. Resende, R. Sanz, A. Ruiz-Clavijo, O. Caballero-Calero and M. Martin-Gonzalez, *Coatings*, 2016, **6**, 59.

225 F. Matsumoto, M. Harada, N. Koura, K. Nishio and H. Masuda, *Electrochem. Solid-State Lett.*, 2004, **7**, E51.

226 J. Choi, J. Schilling, K. Nielsch, R. Hillebrand, M. Reiche, R. Wehrspohn and U. Gösele, *MRS Online Proc. Libr. Arch.*, 2002, **722**, 52.

227 Z. Fan, H. Razavi, J.-w. Do, A. Moriwaki, O. Ergen, Y.-L. Chueh, P. W. Leu, J. C. Ho, T. Takahashi and L. A. Reichertz, *Nat. Mater.*, 2009, **8**, 648–653.

228 L. Wen, R. Xu, Y. Mi and Y. Lei, *Nat. Nanotechnol.*, 2017, **12**, 244–250.

229 Y. Xu, M. Zhou, L. Wen, C. Wang, H. Zhao, Y. Mi, L. Liang, Q. Fu, M. Wu and Y. Lei, *Chem. Mater.*, 2015, **27**, 4274–4280.

230 K. Yasui, K. Nishio and H. Masuda, *Jpn. J. Appl. Phys.*, 2005, **44**, L1181.

231 G. Fois, C. T. Bolger, J. D. Holmes and G. Cross, *MRS Online Proc. Libr. Arch.*, 2010, **1258**, 1258-Q05-01.

232 J. Choi, R. B. Wehrspohn and U. Gösele, *Electrochim. Acta*, 2005, **50**, 2591–2595.

233 H. Asoh, S. Ono, T. Hirose, I. Takatori and H. Masuda, *Jpn. J. Appl. Phys.*, 2004, **43**, 6342.

234 J. Choi, K. Nielsch, M. Reiche, R. Wehrspohn and U. Gösele, *J. Vac. Sci. Technol., B: Microelectron. Nanometer Struct.–Process., Meas., Phenom.*, 2003, **21**, 763–766.

235 S. Shingubara, S. Maruo, T. Yamashita, M. Nakao and T. Shimizu, *Microelectron. Eng.*, 2010, **87**, 1451–1454.

236 H. Masuda, Y. Matsui, M. Yotsuya, F. Matsumoto and K. Nishio, *Chem. Lett.*, 2004, **33**, 584–585.

237 S. Fournier-Bidoz, V. Kitaev, D. Routkevitch, I. Manners and G. A. Ozin, *Adv. Mater.*, 2004, **16**, 2193–2196.

238 Q. Xu, G. Meng and F. Han, *Prog. Mater. Sci.*, 2018, **95**, 243–285.

239 D. Routkevitch, A. Tager, J. Haruyama, D. Almawlawi, M. Moskovits and J. M. Xu, *IEEE Trans. Electron Devices*, 1996, **43**, 1646–1658.

240 W. J. Stępniowski and M. Salerno, *Manuf. Nanostruct.*, 2014, **12**, 321–357.

241 H. Hashimoto, Y. Shigehara, S. Ono and H. Asoh, *Microporous Mesoporous Mater.*, 2018, **265**, 77–83.

242 L. Vera-Londono, A. Ruiz-Clavijo, O. Caballero-Calero and M. Martín-González, *Nanoscale Adv.*, 2020, **2**, 4591–4603.

243 T. Huber, K. Owusu, S. Johnson, A. Nikolaeva, L. Konopko, R. Johnson and M. J. Graf, *J. Appl. Phys.*, 2012, **111**, 043709.

244 M. Sistani, P. Staudinger, J. Greil, M. Holzbauer, H. Detz, E. Bertagnolli and A. Lugstein, *Nano Lett.*, 2017, **17**, 4556–4561.

245 J. Fang, S. Chen, W. G. Vandenberghe and M. V. Fischetti, *IEEE Trans. Electron Devices*, 2017, **64**, 2758–2764.

246 M. Muñoz Rojo, Y. Zhang, C. V. Manzano, R. Alvaro, J. Gooth, M. Salmeron and M. Martin-Gonzalez, *Sci. Rep.*, 2016, **6**, 19014.

247 S. S. Parkin, M. Hayashi and L. Thomas, *Science*, 2008, **320**, 190–194.

248 D. A. Allwood, G. Xiong, C. Faulkner, D. Atkinson, D. Petit and R. Cowburn, *Science*, 2005, **309**, 1688–1692.

249 J. A. Fernandez-Roldan, R. P. del Real, C. Bran, M. Vazquez and O. Chubykalo-Fesenko, *Nanoscale*, 2018, **10**, 5923–5927.

250 C. Murapaka, P. Sethi, S. Goolaup and W. S. Lew, *Sci. Rep.*, 2016, **6**, 20130.

251 C. Bran, E. Berganza, J. A. Fernandez-Roldan, E. M. Palmero, J. Meier, E. Calle, M. Jaafar, M. Foerster, L. Aballe and A. Fraile Rodriguez, *ACS Nano*, 2018, **12**, 5932–5939.

252 Y. P. Ivanov, M. Vázquez and O. Chubykalo-Fesenko, *J. Phys. D: Appl. Phys.*, 2013, **46**, 485001.

253 S. Da Col, S. Jamet, N. Rougemaille, A. Locatelli, T. O. Mentes, B. S. Burgos, R. Afid, M. Darques, L. Cagnon and J.-C. Toussaint, *Phys. Rev. B: Condens. Matter Mater. Phys.*, 2014, **89**, 180405.

254 R. Wieser, U. Nowak and K.-D. Usadel, *Phys. Rev. B: Condens. Matter Mater. Phys.*, 2004, **69**, 064401.

255 H. Forster, T. Schrefl, W. Scholz, D. Suess, V. Tsiantos and J. Fidler, *J. Magn. Magn. Mater.*, 2002, **249**, 181–186.

256 M. Yan, A. Kákay, S. Gliga and R. Hertel, *Phys. Rev. Lett.*, 2010, **104**, 057201.

257 S. S. Parkin, M. Hayashi and L. Thomas, *Science*, 2008, **320**(5873), 190–194.

258 K. Pitzschel, J. Bachmann, S. Martens, J. M. Montero-Moreno, J. Kimling, G. Meier, J. Escrig, K. Nielsch and D. Görlitz, *J. Appl. Phys.*, 2011, **109**, 033907.

259 Y. T. Chong, D. Görlitz, S. Martens, M. Y. E. Yau, S. Allende, J. Bachmann and K. Nielsch, *Adv. Mater.*, 2010, **22**, 2435–2439.

260 S. Samanifar, M. Alikhani, M. A. Kashi, A. Ramazani and A. Montazer, *J. Magn. Magn. Mater.*, 2017, **430**, 6–15.

261 A. Samardak, A. Ognev, A. Y. Samardak, E. Stebliy, E. Modin, L. Chebotkevich, S. Komogortsev, A. Stancu, E. Panahi-Danaei and A. Fardi-Ilkhichy, *J. Alloys Compd.*, 2018, **732**, 683–693.

262 S. Ruiz-Gómez, M. Foerster, L. Aballe, M. P. Proenca, I. Lucas, J. L. Prieto, A. Mascaraque, J. de la Figuera, A. Quesada and L. Pérez, *Sci. Rep.*, 2018, **8**, 1–6.

263 M. Abbas, A. Ramazani, A. Montazer and M. A. Kashi, *J. Appl. Phys.*, 2019, **125**, 173902.

264 N. Şarlı and M. Keskin, *Solid State Commun.*, 2012, **152**, 354–359.

265 K. Liu, K. Nagodawithana, P. Searson and C. Chien, *Phys. Rev. B: Condens. Matter Mater. Phys.*, 1995, **51**, 7381.

266 H. Kamimura, M. Hayashida and T. Ohgai, *Nanomaterials*, 2020, **10**, 5.

267 J. E. Perez and J. Kosel, in *Magnetic Nano-and Microwires*, Elsevier, 2020, pp. 697–713.

268 A. Prina-Mello, Z. Diao and J. M. D. Coey, *J. Nanobiotechnol.*, 2006, **4**, 9.

269 Y. P. Ivanov, A. Alfadhel, M. Alnassar, J. E. Perez, M. Vazquez, A. Chuvilin and J. Kosel, *Sci. Rep.*, 2016, **6**, 24189.

270 A. I. Martínez-Banderas, A. Aires, S. Plaza-García, L. Colás, J. A. Moreno, T. Ravasi, J. S. Merzaban, P. Ramos-Cabrer, A. L. Cortajarena and J. Kosel, *J. Nanobiotechnol.*, 2020, **18**, 1–12.

271 W.-S. Lin, H.-M. Lin, H.-H. Chen, Y.-K. Hwu and Y.-J. Chiou, *J. Nanomater.*, 2013, 237439.

272 C. Rodríguez-Fernández, C. V. Manzano, A. H. Romero, J. Martín, M. Martín-González, M. Morais de Lima Jr. and A. Cantarero, *Nanotechnology*, 2016, **27**, 075706.

273 C. V. Manzano, M. N. Polyakov, J. Maiz, M. H. Aguirre, X. Maeder and M. Martín-González, *Sci. Technol. Adv. Mater.*, 2019, **20**, 1022–1030.

274 L. Hicks and M. S. Dresselhaus, *Phys. Rev. B: Condens. Matter Mater. Phys.*, 1993, **47**, 16631.

275 M. Dresselhaus, G. Dresselhaus, X. Sun, Z. Zhang, S. Cronin and T. Koga, *Phys. Solid State*, 1999, **41**, 679–682.

276 M. M. Rojo, B. Abad, C. V. Manzano, P. Torres, X. Cartoixà, F. Alvarez and M. M. Gonzalez, *Nanoscale*, 2017, **9**, 6741–6747.

277 G. Gadea, A. Morata and A. Tarancon, in *Semiconductors and Semimetals*, Elsevier, 2018, vol. 98, pp. 321–407.

278 L. Shen, H. Du, J. Yang and Z. Ma, *Appl. Surf. Sci.*, 2015, **325**, 100–104.

279 R. Zhang, C. Zhao, B. Shao, J. Dong, J. Zhang and H. Yang, Broadband and quasi-omnidirectional antireflection Si subwavelength structure based on alumina nano-template directly formed on $SiO_2/Si$, in *Advances in Optoelectronics and Micro/nano-optics*, IEEE, 2010, pp. 1–4.

280 H. Deniz, T. Khudiyev, F. Buyukserin and M. Bayindir, *Appl. Phys. Lett.*, 2011, **99**, 183107.

281 L. Chen, J. Xie, K. R. Aatre and V. K. Varadan, *J. Nanotechnol. Eng. Med.*, 2009, **1**(1), 011009-1/8.

282 L. Chen, J. Xie, K. R. Aatre, J. Yancey, M. Srivatsan and V. K. Varadan, *Nanosystems in Engineering and Medicine*, International Society for Optics and Photonics, 2012, vol. 8548, p. 854867.

283 L. González-Souto, L. González-Rovira, F. J. Botana, J. J. Calvino, M. Á. Cauqui and J. C. Hernández-Garrido, *Part. Part. Syst. Charact.*, 2019, **36**, 1900168.

284 P. Banerjee, I. Perez, L. Henn-Lecordier, S. B. Lee and G. W. Rubloff, *Nat. Nanotechnol.*, 2009, **4**, 292–296.

285 L. C. Haspert, S. B. Lee and G. W. Rubloff, *ACS Nano*, 2012, **6**, 3528–3536.

286 Q. Lin, S.-F. Leung, L. Lu, X. Chen, Z. Chen, H. Tang, W. Su, D. Li and Z. Fan, *ACS Nano*, 2014, **8**, 6484–6490.

287 A. Brzózka, D. Szeliga, E. Kurowska-Tabor and G. D. Sulka, *Mater. Lett.*, 2016, **174**, 66–70.

288 M. M. Tavakoli, Q. Lin, S.-F. Leung, G. C. Lui, H. Lu, L. Li, B. Xiang and Z. Fan, *Nanoscale*, 2016, **8**, 4276–4283.

289 F. Béron, A. Kaidatzis, M. F. Velo, L. C. C. Arzuza, E. M. Palmero, R. P. del Real, D. Niarchos, K. R. Pirota and J. M. García-Martín, *Nanoscale Res. Lett.*, 2016, **11**, 86.

290 C. Bran, P. Gawronski, I. Lucas, R. P. del Real, P. Strichovanec, A. Asenjo, M. Vazquez and O. Chubykalo-Fesenko, *J. Phys. D: Appl. Phys.*, 2017, **50**, 065003.

291 T. N. A. Nguyen, J. Fedotova, J. Kasiuk, V. Bayev, O. Kupreeva, S. Lazarouk, D. H. Manh, D. L. Vu, S. Chung, J. Åkerman, V. Altynov and A. Maximenko, *Appl. Surf. Sci.*, 2018, **427**, 649–655.

292 M. T. Rahman, N. N. Shams, C. H. Lai, J. Fidler and D. Suess, *Phys. Rev. B: Condens. Matter Mater. Phys.*, 2010, **81**, 014418.

293 A. Maximenko, M. Marszałek, J. Chojenka, J. Fedotova, B. R. Jany, F. Krok, J. Morgiel, A. Zarzycki and Y. Zabila, *J. Magn. Magn. Mater.*, 2019, **477**, 182–189.

294 M. Salaheldeen, V. Vega, A. Fernández and V. M. Prida, *J. Magn. Magn. Mater.*, 2019, **491**, 165572.

295 M. Salaheldeen, M. Méndez, V. Vega, A. Fernández and V. M. Prida, *ACS Appl. Nano Mater.*, 2019, **2**, 1866–1875.

296 Y. Li, Y. Chen, M. Qiu, H. Yu, X. Zhang, X. W. Sun and R. Chen, *Sci. Rep.*, 2016, **6**, 20114.

297 J.-H. Lee, G. A. Galli and J. C. Grossman, *Nano Lett.*, 2008, **8**, 3750–3754.

298 Q. Hao, G. Chen and M.-S. Jeng, *J. Appl. Phys.*, 2009, **106**, 114321.

299 B. Abad, J. Maiz, A. Ruiz-Clavijo, O. Caballero-Calero and M. Martin-Gonzalez, *Sci. Rep.*, 2016, **6**, 38595.

300 E. Gillette, S. Wittenberg, L. Graham, K. Lee, G. Rubloff, P. Banerjee and S. B. Lee, *Phys. Chem. Chem. Phys.*, 2015, **17**, 3873–3879.

301 H. S. Bindra, S. John, S. C. Roy, O. P. Sinha, S. S. Islam and R. Nayak, *J. Electrochem. Soc.*, 2017, **165**, H3061–H3068.

302 C. Papadopoulos, A. Rakitin, J. Li, A. S. Vedeneev and J. M. Xu, *Phys. Rev. Lett.*, 2000, **85**, 3476–3479.

303 Q. Guo, L. Qin, J. Zhao, Y. Hao, Z. Yan, F. Mu and P. Chen, *Physica E*, 2012, **44**, 1988–1991.

304 C. Berger, Y. Yi, Z. L. Wang and W. A. de Heer, *Appl. Phys. A*, 2002, **74**, 363–365.

305 M. S. Fuhrer, M. Forero, A. Zettl and P. L. McEuen, *AIP Conf. Proc.*, 2001, **591**, 401–404.

306 H. J. Li, W. G. Lu, J. J. Li, X. D. Bai and C. Z. Gu, *Phys. Rev. Lett.*, 2005, **95**, 086601.

307 M. Bockrath, D. H. Cobden, P. L. McEuen, N. G. Chopra, A. Zettl, A. Thess and R. E. Smalley, *Science*, 1997, **275**, 1922.

308 W. Yi, L. Lu, H. Hu, Z. W. Pan and S. S. Xie, *Phys. Rev. Lett.*, 2003, **91**, 076801.

309 S. J. Tans, M. H. Devoret, H. Dai, A. Thess, R. E. Smalley, L. J. Geerligs and C. Dekker, *Nature*, 1997, **386**, 474–477.

310 S. Ilani, L. A. K. Donev, M. Kindermann and P. L. McEuen, *Nat. Phys.*, 2006, **2**, 687–691.

311 V. N. Popov, *Mater. Sci. Eng., R*, 2004, **43**, 61–102.

312 H. Dai, *Surf. Sci.*, 2002, **500**, 218–241.

313 R. H. Baughman, A. A. Zakhidov and W. A. de Heer, *Science*, 2002, **297**, 787.

314 A. Javey, J. Guo, Q. Wang, M. Lundstrom and H. Dai, *Nature*, 2003, **424**, 654–657.

315 T. J. Kazmierski, D. Zhou, B. M. Al-Hashimi and P. Ashburn, *IEEE Trans. Nanotechnol.*, 2010, **9**, 99–107.

316 T.-T. Tran and A. Mulchandani, *TrAC, Trends Anal. Chem.*, 2016, **79**, 222–232.

317 H. W. C. Postma, T. Teepen, Z. Yao, M. Grifoni and C. Dekker, *Science*, 2001, **293**, 76.

318 H. Li, Q. Zhang and J. Li, *Appl. Phys. Lett.*, 2006, **88**, 013508.

319 J. Li, C. Papadopoulos, J. M. Xu and M. Moskovits, *Appl. Phys. Lett.*, 1999, **75**, 367–369.

320 H. Gao, C. Mu, F. Wang, D. Xu, K. Wu, Y. Xie, S. Liu, E. Wang, J. Xu and D. Yu, *J. Appl. Phys.*, 2003, **93**, 5602–5605.

321 D. N. Davydov, J. Li, K. B. Shelimov, T. L. Haslett, M. Moskovits and B. W. Statt, *J. Appl. Phys.*, 2000, **88**, 7205–7208.

322 C. Kshirsagar, H. Li, T. E. Kopley and K. Banerjee, *IEEE Electron Device Lett.*, 2008, **29**, 1408–1411.

323 K. B. Shelimov, D. N. Davydov and M. Moskovits, *Appl. Phys. Lett.*, 2000, **77**, 1722–1724.

324 W. S. Im, Y. S. Cho, G. S. Choi, F. C. Yu and D. J. Kim, *Diamond Relat. Mater.*, 2004, **13**, 1214–1217.

325 W. Y. Jang, N. N. Kulkarni, C. K. Shih and Z. Yao, *Appl. Phys. Lett.*, 2004, **84**, 1177–1179.

326 R. Mangu, S. Rajaputra, P. Clore, D. Qian, R. Andrews and V. P. Singh, *J. Mater. Sci. Eng. B*, 2010, **174**, 2–8.

327 A. Mezni, T. Altalhi, N. B. Saber, A. Aldalbahi, S. Boulehmi, A. Santos and D. Losic, *J. Colloid Interface Sci.*, 2017, **491**, 375–389.

328 I. Jung, H. Y. Jang, J. Moon and S. Park, *Nanoscale*, 2014, **6**, 6482–6486.

329 A. Sinitskii and J. M. Tour, *J. Am. Chem. Soc.*, 2010, **132**, 14730–14732.

330 K. Tada, N. Kosugi, K. Sakuramoto, T. Hashimoto, K. Takeuchi, Y. Yagi, J. Haruyama, H. Yang and M. Chshiev, *J. Supercond. Novel Magn.*, 2013, **26**, 1037–1043.

331 C. Mijangos, R. Hernández and J. Martín, *Prog. Polym. Sci.*, 2016, **54–55**, 148–182.

332 D. O'Carroll, I. Lieberwirth and G. Redmond, *Nat. Nanotechnol.*, 2007, **2**, 180–184.

333 D. O'Carroll, D. Iacopino and G. Redmond, *Adv. Mater.*, 2009, **21**, 1160–1165.

334 L.-B. Huang, Z.-X. Xu, X. Chen, W. Tian, S.-T. Han, Y. Zhou, J.-J. Xu, X.-B. Yang and V. A. L. Roy, *ACS Appl. Mater. Interfaces*, 2014, **6**, 11874–11881.

335 T. Yanagishita, M. Sasaki, K. Nishio and H. Masuda, *Adv. Mater.*, 2004, **16**, 429–432.

336 Z. Yao, C. Wang, Y. Li and N.-Y. Kim, *Nanoscale Res. Lett.*, 2015, **10**, 166.

337 A. L. Friedman, *The magnetic and transport properties of template-synthesized carbon-based and related nanomaterials*, Doctoral dissertation, Northeastern University, 2009.

338 G. Meng, Y. J. Jung, A. Cao, R. Vajtai and P. M. Ajayan, *Proc. Natl. Acad. Sci. U. S. A.*, 2005, **102**, 7074–7078.

339 W. Lee, J.-C. Kim and U. Gösele, *Adv. Funct. Mater.*, 2010, **20**, 21–27.

340 M. Méndez, V. Vega, S. González, R. Caballero-Flores, J. García and V. M. Prida, *Nanomaterials*, 2018, **8**, 595.

341 C. V. Manzano, D. Ramos, L. Petho, G. Bürki, J. Michler and L. Philippe, *J. Phys. Chem. C*, 2018, **122**, 957–963.

342 C. Manzano, J. Best, J. Schwiedrzik, A. Cantarero, J. Michler and L. Philippe, *J. Mater. Chem. C*, 2016, **4**, 7658–7666.

343 K. Choudhari, S. D. Kulkarni, V. Unnikrishnan, R. K. Sinha, C. Santhosh and S. D. George, *Nano-Struct. Nano-Objects*, 2019, **19**, 100354.

344 X. Wang, D. Zhang, H. Zhang, Y. Ma and J. Jiang, *Nanotechnology*, 2011, **22**, 305306.

345 J. Xue, Z.-K. Zhou, Z. Wei, R. Su, J. Lai, J. Li, C. Li, T. Zhang and X.-H. Wang, *Nat. Commun.*, 2015, **6**, 8906.

346 Y. Chen, A. Santos, D. Ho, Y. Wang, T. Kumeria, J. Li, C. Wang and D. Losic, *Electrochim. Acta*, 2015, **174**, 672–681.

347 S. Zhang, Q. Xu, S. Feng, C. Sun, Q. Peng and T. Lan, *Opt. Mater.*, 2019, **98**, 109488.

348 A. Ruiz-Clavijo, Y. Tsurimaki, O. Caballero-Calero, G. Ni, G. Chen, S. V. Boriskina and M. Martín-González, *ACS Photonics*, 2018, **5**, 2120–2128.

349 S. Abbasimofrad, M. A. Kashi, M. Noormohammadi and A. Ramazani, *J. Phys. Chem. Solids*, 2018, **118**, 221–231.

350 A. Santos, *J. Mater. Chem. C*, 2017, **5**, 5581–5599.

351 C. S. Law, S. Y. Lim, A. D. Abell, N. H. Voelcker and A. Santos, *Nanomaterials*, 2018, **8**, 788.

352 H. Masuda, M. Ohya, H. Asoh, M. Nakao, M. Nohtomi and T. Tamamura, *Jpn. J. Appl. Phys.*, 1999, **38**, L1403.

353 W. J. Zheng, G. T. Fei, B. Wang, Z. Jin and L. De Zhang, *Mater. Lett.*, 2009, **63**, 706–708.

354 Y. Liu, Y. Chang, Z. Ling, X. Hu and Y. Li, *Electrochem. Commun.*, 2011, **13**, 1336–1339.

355 Y. Su, G. T. Fei, Y. Zhang, P. Yan, H. Li, G. L. Shang and L. De Zhang, *Mater. Lett.*, 2011, **65**, 2693–2695.

356 B. Wang, G. T. Fei, M. Wang, M. G. Kong and L. De Zhang, *Nanotechnology*, 2007, **18**, 365601.

357 M. M. Rahman, L. F. Marsal, J. Pallarès and J. Ferré-Borrull, *ACS Appl. Mater. Interfaces*, 2013, **5**, 13375–13381.

358 L. Zhi-Yuan, C. Shuo-Shuo, H. Xing and L. Yi, *Chin. Phys. Lett.*, 2009, **26**, 054213.

359 P. Yan, G. T. Fei, G. L. Shang, B. Wu and L. De Zhang, *J. Mater. Chem. C*, 2013, **1**, 1659–1664.

360 G. Shang, G. Fei, Y. Li and L. Zhang, *Nano Res.*, 2016, **9**, 703–712.

361 G. L. Shang, G. T. Fei, Y. Zhang, P. Yan, S. H. Xu and L. De Zhang, *J. Mater. Chem. C*, 2013, **1**, 5285–5291.

362 Y. Chen, A. Santos, Y. Wang, T. Kumeria, J. Li, C. Wang and D. Losic, *ACS Appl. Mater. Interfaces*, 2015, **7**, 19816–19824.

363 Y. Wang, Y. Chen, T. Kumeria, F. Ding, A. Evdokiou, D. Losic and A. Santos, *ACS Appl. Mater. Interfaces*, 2015, **7**, 9879–9888.

364 C. S. Law, S. Y. Lim, A. D. Abell, L. F. Marsal and A. Santos, *Nanoscale*, 2018, **10**, 14139–14152.

365 A. Santos, C. S. Law, D. W. C. Lei, T. Pereira and D. Losic, *Nanoscale*, 2016, **8**, 18360–18375.

366 A. Santos, T. Pereira, C. S. Law and D. Losic, *Nanoscale*, 2016, **8**, 14846–14857.

367 A. Santos, C. S. Law, T. Pereira and D. Losic, *Nanoscale*, 2016, **8**, 8091–8100.

368 T. Kumeria, M. M. Rahman, A. Santos, J. Ferré-Borrull, L. F. Marsal and D. Losic, *Anal. Chem.*, 2014, **86**, 1837–1844.

369 T. Kumeria, M. M. Rahman, A. Santos, J. Ferré-Borrull, L. F. Marsal and D. Losic, *ACS Appl. Mater. Interfaces*, 2014, **6**, 12971–12978.

370 M. Nemati, A. Santos, C. S. Law and D. Losic, *Anal. Chem.*, 2016, **88**, 5971–5980.

371 A. Santos, J. H. Yoo, C. V. Rohatgi, T. Kumeria, Y. Wang and D. Losic, *Nanoscale*, 2016, **8**, 1360–1373.

372 K. Choi, Y. Yoon, J. Jung, C. W. Ahn, G. J. Lee, Y. M. Song, M. J. Ko, H. S. Lee, B. Kim and I. S. Kang, *Adv. Opt. Mater.*, 2017, **5**, 1600616.

373 G. Rajeev, B. Prieto Simon, L. F. Marsal and N. H. Voelcker, *Adv. Healthcare Mater.*, 2018, **7**, 1700904.

374 P. Kapruwan, J. Ferré-Borrull and L. F. Marsal, *Adv. Mater. Interfaces*, 2020, 2001133.

375 M. S. Aw, M. Kurian and D. Losic, *Biomater. Sci.*, 2014, **2**, 10–34.

376 R. Fazli-Abukheyli, M. R. Rahimi and M. Ghaedi, *J. Drug Delivery Sci. Technol.*, 2019, **54**, 101247.

377 E. Davoodi, M. Zhianmanesh, H. Montazerian, A. S. Milani and M. Hoorfar, *J. Mater. Sci.: Mater. Med.*, 2020, **31**, 1–16.

378 G. Mistura, L. Bruschi and W. Lee, *J. Low Temp. Phys.*, 2016, **185**, 138–160.

379 M. Mir, M. Shah and P. Ganai, *J. Solid State Electrochem.*, 2020, **24**, 1679–1686.

380 C. Jeong and H. Ji, *Materials*, 2019, **12**, 3231.